GRAPHENE TRANSFER ONTO PP, PES AND PVDF POLYMERIC SUBSTRATES: DEVELOPMENT OF WATER PURIFICATION MEMBRANES

BY

FERAS MOHAMMAD ABDALLA KAFIAH

A Dissertation Presented to the
DEANSHIP OF GRADUATE STUDIES

KING FAHD UNIVERSITY OF PETROLEUM & MINERALS

DHAHRAN, SAUDI ARABIA

In Partial Fulfillment of the
Requirements for the Degree of

DOCTOR OF PHILOSOPHY

In

MECHANICAL ENGINEERING

DECEMBER 2015

KING FAHD UNIVERSITY OF PETROLEUM & MINERALS
DHAHRAN- 31261, SAUDI ARABIA

DEANSHIP OF GRADUATE STUDIES

This thesis, written by **FERAS MOHAMMAD ABDALLA KAFIAH** under the direction his thesis advisor and approved by his thesis committee, has been presented and accepted by the Dean of Graduate Studies, in partial fulfillment of the requirements for the degree of **DOCTOR OF PHILISOPHY IN MECHANICAL ENGINEERING.**

Dr. Zafarullah Khan
(Advisor)

Dr. Tahar Laoui
(Co-Advisor)

Dr. Saheb Nouari
(Member)

Dr. Muataz A. Hussien
(Member)

Dr. Isam Aljundi
(Member)

Dr. Zuhair M. Gasem
Department Chairman

Dr. Salam A. Zummo
Dean of Graduate Studies

3/3/16
Date

DEDICATION

To my parents,
who always picked me up on time
and encouraged me to go on every adventure.

To my wife,
her tender-loving care, patience,
and dedication to me and our children,
has been a constant source of inspiration
for me while working during my PhD.

To my children Mohammad and Ibraheem,
their shiny eyes gave me the power to always stand and look forward

To my coming baby who we still have not decided his/her name

To my only brother and all of my sisters,
who are always looking at me proudly and follow my success step by step

ACKNOWLEDGMENTS

Praise and thanks to **ALLAH** who helped me accomplish this great step on my life and for letting me through all the difficulties. I have experienced your presence and power at all times and in all places day by day. You are the one who let me finish my degree.

I would like to express my deep appreciation to my advisor Professor **Dr. Zafarullah Khan**; you have been a marvelous supporter for me. Thank you for inspiring my research and for teaching me how to be a research scientist. Thanks also for your wonderful remarks and suggestions. I would also like to thank my committee members, Professor Tahar Laoui, Professor Mutaz Atteih, Professor Isam Aljundi and Professor Saheb Nouari for helping as my committee members.

Thanks for Professor Rohit Karnik and his group at Massachusetts Institute of Technology for their real collaboration and hospitality during my visit in the summer of 2014. Special thanks to all of my colleagues and lab instructors at King Fahd University of Petroleum & Minerals; all of you have been there to support me during my wonderful Ph.D. journey.

I would like to thank my family one by one. Without their support mixed with love over the years, none of this would have happened. Their prayers always guided me and helped me to overcome difficulties.

TABLE OF CONTENTS

LIST OF TABLES

LIST OF FIGURES

LIST OF ABBREVIATIONS

AFM	:	Atomic Force Microscope
APC	:	Adipoyl Chloride
APS	:	Ammonium Persulphate
APTES	:	Aminopropyl-triethoxysilane
ARPES	:	Angle-Resolved Photoemission Spectroscopy
CA	:	Contact Angle
CNT	:	Carbon Nanotubes
CVD	:	Chemical Vapor Deposition
DI	:	De-ionized Water.
DMF	:	N, N-Dimethylformamide
FLG	:	Few-Layer Graphene
GIC	:	Graphite Intercalation Compound
GO	:	Graphite Oxide
HMDA	:	Hexamethylenediamine
HOMO	:	Highest Occupied Molecular Orbital
HOPG	:	Highly Ordered Pyrolytic Graphite

IP : Interfacial Polymerization

IPA : Isopropanol

IUPAC : International Union of Pure and Applied Chemistry

KCl : Potassium Chloride

LEED : Low-Energy Electron Diffraction

LUMO : Lowest Unoccupied Molecular Orbital

MW : Molecular Weight

PDMS : Polydimethylsiloxane

PES : Polyethersulfone

PFPA : Perfluorophenylazide

PMMA : Polymethyl methacrylate

PP : Polypropylene

PSU : Polysulfone

PVDF : Polyvinylidene difluoride

RMS : Root Mean Square

SAM : Self Assembled Monolayers

SEM : Scanning Electron Microscope

SiC	:	Silicon Carbide
TEM	:	Transmission Electron Microscope
TiC	:	Titanium Carbide
TR	:	Texas Red
UHV	:	Ultra-High Vacuum

ABSTRACT

Full Name : Feras Mohammad Abdalla Kafiah

Thesis Title : Graphene Transfer onto PP, PES and PVDF Polymeric Substrates: Development of Water Purification Membranes.

Major Field : Ph.D. in Mechanical Engineering

Date of Degree : Dec 2015

Transfer of graphene grown by chemical vapor deposition (CVD) to porous membranes with minimal defects is important for the fabrication of nanoporous (NPG) graphene membranes. The present work reports the transfer of graphene onto electrospun polysulfone (PSU) nanofiber mats and eight commercial micro/ultrafiltration membranes, namely, polypropylene (PP), polyethersulfone (PES) and six polyvinylidenedifluoride (PVDF) membranes having different pore sizes and surface characteristics. Monolayer graphene was transferred onto electrospun PSU nanofiber mat by electrospinning PSU directly onto the graphene monolayer grown over copper foil whereas a roll press transfer method was used to transfer graphene on all other membrane substrates. A newly developed electrostatic transfer method was also used for graphene transfer on the hydrophilic membrane substrates. In all cases copper was dissolved by wet etching to obtain membranes containing graphene monolayer over the polymeric micro/ultrafiltration substrates. Three parameters, namely, the roughness of the substrate, the pore size and the surface wetting (degree of hydrophobicity) were found to affect the coverage and conformality of the transferred graphene monolayer on the membrane surface. Graphene severely tore and cracked during the transfer onto the PSU mat due to its high surface roughness and

large pore size. Using the pressing method, good graphene transfer was obtained when the substrate surface had adequate hydrophobicity (Contact Angle > 90^o), and the contact angle to surface roughness (root mean square, RMS) ratio was higher than 2.5 (CA/RMS > 2.5).

Post transfer examination of graphene on polymer substrate carried out via SEM indicated a good graphene transfer with good surface coverage, but revealed the existence of defects (cracks and tears) in the graphene layer. In order to assess the extent of the defects, ion transport characteristics of the otherwise total impervious graphene was investigated by the diffusion of Potassium Chloride (KCl) ions using a Side-bi-Side diffusion cell. The graphene-PP membrane blocked 57% (43% leakage) of KCl ions, whereas the graphene-PVDF 5 membrane blocked 40% (60% leakage) of the ions. The heavy ion leakage through the graphene monolayer confirmed the presence of defects in the transferd graphene. The defects were sealed *via* interfacial polymerization (IP) of Nylon 6,6 into the defects, which allowed plugging of most of the defects. Consequently KCl ion blockage increased to approximately 80-85% (15-20% leakage) for all graphene membranes.

Bi-layer and multi layer graphene was also transferred to the PP substrate. Compared with the 57% ion blockage of monolayer graphene, the ion blockage through bi-layer graphene membrane was a little better (~ 60%) which further increased to 73% after the Nylon 6,6 defect plugging, which was lower than defect sealed the monolayer graphene (~ 84%). Surprisingly, multi-layer graphene transferred onto the PP without IP successfully blocked 82% of KCl ions. A negligible enhancement was seen after sealing defects using the IP process.

Graphene/PP membrane showed high conventional permeation fluxes at differnet pressures but at the expense of salt rejection. Biofouling resistance of graphene was alos investigated using E-coli becterial strains. Graphene reduced the static bacterial adhesion (enhanced the biofouling resistance) when transferred to hydrophilic substrates (PES & PVDF 1), wheras opposite occurred when transferred to the hydrophobic substrate (PP).

ملخص الرسالة

الاسم الكامل : فراس محمد عبدالله كافيه

عنوان الرسالة : نقل الغرافين على الأغشية المبلمرة (البولي بروبيلين و البولي ايثرسلفون و البولي فينيليدينديايفلورايد) لتطوير أغشية تنقية المياه.

التخصص : الدكتوراة في الهندسة الميكانيكية

تاريخ الدرجة : ديسمبر لعام 2015 ميلادية

يعتبر نقل الغرافين (مادة كربونية ثنائية الأبعاد و التي تأخذ شكل خلية النحل) قليل العيوب و الذي يصنع بوساطة عملية ترسيب الأبخرة الكيميائية (CVD process) إلى الأغشية المسامية مهم جداً لتصنيع أغشية الغرافين. تم في هذا البحث نقل الغرافين إلى غشاء البوليسلفون (PSU) ذي الألياف النانوية المغزولة كهربائياً و ايضاً إلى ثمانية أنواع من الأغشية التجارية و المستخدة في عملية الفلترة الدقيقة (Microfiltration) و هي: البولي بروبيلين (PP) و البولي ايثرسلفون (PES) و ستة أنواع من البولي فينيليدينديايفلورايد (PVDF1, 2, 3, 4, 5 & 6) و التي تختلف عن بعضها البعض في حجم المسام و طبوغرافية السطح.

تم نقل الغرافين أحادي الطبقة على البوليسلفون ذو الألياف النانوية بإستخدام طريقة الغزل الكهربي (Electrospinning method) و تم نقله أيضاً إلى جميع الأغشية التجارية الثمانية بإستخدام عملية النقل بالضغط (Pressing method). تم أيضاً تم تطوير و استخدام طريقة النقل الإلكتروستاتيكي (Electrostatic method) و التي تناسب الأغشية المحبة للماء. تم إذابة طبقة النحاس الحاملة للغرافين كيميائياً في جميع طرق النقل المستخدمة في هذا البحث للحصول أخيراً على الغشاء الغرافيني أحادي الطبقة. لقد وجد أن هناك ثلاثة عوامل رئيسية تؤثر على جودة الغرافين المنقول على سطح الغشاء و هي: خشونة السطح و حجم المسام و مقدار البلل السطحي.

لقد تمزقت طبقة الغرافين بشدة و ظهر فيها الكثير من العيوب السطحية عند نقلها على أغشية البوليسلفون ذو الألياف النانوية و ذلك لخشونة السطح و كبر حجم المسامات. يتم الحصول على غرافين بجودة ممتازة بإستخدام عملية الضغط عندما يكون مقدار البلل السطحي للغشاء المنقول عليه أكثر من 90° و عندما يكون ناتج قسمة

مقدار زاوية الاتصال على مقدار خشونة السطح أكثر من 2.5 و في حال كانت أقل، تكون جودة الغشاء الغرافيني المنقول سيئة جداً.

أظهرت نتائج المجهر الإلكتروني الماسح أن الغرافين المنقول كان مقبول الجودة و يغطي مساحة كبيرة و أظهرت أيضاً وجود بعض الخلل في طبقة الغرافين و التي نشأت أثناء عملية النقل. لدراسة تأثير هذه العيوب، تم عمل دراسات الحمل الايوني (Transport studies) و ذلك بتعريض غشاء الغرافين لفرق تركيز ايوني عالي على جانبيه لتسهيل إنتقال أيونات كلورين البوتاسيوم (KCl) بإستخدام وحدة مخبرية متخصصة (Diffusion cell). على سبيل المثال تمكن الغشاء الغرافيني المنقول على البولي بروبيلين من وقف 57% من الأيونات المنتقلة، فيما تمكن الغشاء الغرافيني المنقول على PVDF 5 من وقف 40% و هذا يدعم فرضية وجود العيوب السطحية. تم تطوير طريقة جديدة لتسكير و قفل العيوب السطحية في الغشاء الغرافيني و ذلك بإستخدام عملية البلمرة السطحية لبوليمر النايلون 6,6 (Interfacial Polymerization) بإستخدام خلية فرانز (Franz cell). ساعدت عملية البلمرة السطحية على زيادة نسبة منع تسرب أيونات كلورين البوتاسيوم لتصل إلى ما يقارب 80-85% و ذلك لجميع أنواع الأغشية الغرافينية المصنعه في هذا البحث.

تم نقل الغرافين ثنائي الطبقة و المصنع بطريقة الترسيب الكيميائي إلى سطح البولي بروبيلين و عند مقارنته بنفس الغشاء أحادي الطبقة، قام بمنع 60% من الأيونات المنتقلة، و عند تسكير العيوب بعملية البلمرة السطحية ارتفعت النسبة إلى 73%. تم أيضاً نقل الغرافين متعدد الطبقات على البوليبروبيلين و بشكل مفاجئ قام هذا الغشاء الجديد بمنع ما نسبته 82% من الأيونات و بعد عملية البلمرة السطحية، تحسنت هذه النسبة بشكل ضئيل. وجد أن الغرافين يحسّن مقاومة الأغشية للإتساخ الحيوي عند نقله إلى الأغشية المحبة للمياه، أما في حالة الأغشية الكارهة للمياه فوجد العكس تماماً. و أخيراً، وجد أن الغشاء الغرافيني على البوليبروبيلين يحقق معدلات تدفق عالية بالمقارنة مع غشاء التناضح العكسي التقليدي و لكن على حساب نسبة رفض الأملاح.

CHAPTER 1

INTRODUCTION

Resistance-free ultrafast transport of water molecules through a membrane while blocking all other ionic species has been the dream of the reverse osmosis (RO) based sea and brackish water desalination technology. Despite considerable efforts made during the recent past to improve the membrane based desalination technology, the current state-of-the-art RO membranes do not offer the desired high levels of permeance and are prone to fouling [1-5]. The thickness of the active (selective) layer of the state-of-the-art polymeric membranes limits the permeability, whereas fouling causes a further flux decline with time and also lowers the membrane’s salt rejection capacity [6, 7]. To realize the dream of ultrafast permeance with minimal resistance to flow, the membrane's active layer needs to be as thin as possible and. To keep the operating cost down, effective solutions to one of the major problems i.e. membrane fouling must also be found. Among various solutions being explored which target the permeability and fouling issues, an emerging approach is to find alternative membrane materials that are inherently free from the limiting factors that hinder ultrafast water transport through the membranes [8-11].

One such promising material is graphene. Graphene not only offers exceptional chemical [12], thermal [13] and mechanical [14, 15] stability, flexibility [16] and low fouling characteristics [9, 17], but most notably is the thinnest (one atom thick) separation (active) membrane layer one could have [8]. Pristine graphene, however, is almost totally impervious even to helium atoms [6, 15], and the key for its use as a separation membrane, especially for the RO process, is to create appropriately-sized pores for the selective passage of water molecules, while guaranteeing the rejection of all other ionic species [18-20]. The synthesis of membranes containing one atom-thick graphene layer with a tailored pore size for ultrafast water permeability is an area of intensive research around the globe [18, 19, 21-23].

A key step in the fabrication of an efficient graphene-based separation membrane is the careful transfer of graphene onto a suitable substrate that can provide the necessary support to its single atom-thick layer [19]. Polymeric ultra and nanofiltration membranes are best suited to act as the support substrates, since graphene is suspended over large pores is fragile, but is predicted to withstand remarkably high pressures when suspended over small pores, such as those of ultra- or nanofiltration membranes [16, 24, 25]. However, transfer of a graphene monolayer to a polymeric membrane substrate is extremely challenging. Despite recent advances in technology, known methods used to transfer graphene result in the introduction of large defects (tears, holes, and cracks) in the graphene layer [19]. These defects must be plugged and sealed to block solute permeation through the defects, and to produce an impervious graphene/polymer composite membrane, before introducing properly sized-pores to convert it to a workable separation membrane. Interfacial polymerization can be adopted to seal the defects, where suitable monomers can be made to meet interfacially inside the defects and polymerize to plug the defects [21].

The quality of the graphene transfer to a polymeric substrate largely depends on the surface characteristics of the substrate [19, 26]. Most important among these are the substrate pore size, surface roughness, and surface wettability. A smooth surface is needed to provide good and conformal adhesion of the graphene monolayer onto the substrate [27]. A small pore size would render sound mechanical support to graphene domains that may otherwise be poorly supported and tear and crack if the substrate pores are large. High hydrophobicity is needed to discourage penetration of the etchant solution between the graphene and membrane substrate; this also averts deleterious attacks on the graphene layer which would deteriorate its quality [19].

The main objective of this work is to find and develop graphene membranes by transferring monolayer graphene onto different commercial polymeric substrates. Selecting and developing the proper method that would transfer graphene with almost zero defects to the polymeric support surface is important step in the development of ultrafast water transport membranes. A careful analysis of the substrates surface characteristics would help in understanding the factors that affect the quality of transferred graphene layer. It is also important to characterize graphene membranes in terms of its quality and performance through diffusion and permeation studies and other performance criteria such as bio-fouling resistance.

Chapter 2 introduces graphene in sections. Section 2.1 discusses in short an introduction to graphene. Section 2.2 gives an overview of graphene’s history. Section 2.3 explores the properties of a graphene as a 2D sheet. Section 2.4 lists the graphene production methods and more specifically, the chemical vapor deposition (CVD). Section 2.5 covers the graphene transfer methods. Section 2.6 focuses on the techniques used to characterize the transferred graphene. Section 2.7 discusses graphene applications with a focus on its application to water purification. Finally, Section 2.8 gives a short introduction to the electrospinning process, which is a process explored in this work to produce polymeric nanofiber substrates for graphene transfer.

Chapter 3 covers the materials used in this study and the experimental procedures that we have followed to characterize the transferred graphene, defect sealing, ionic diffusion, salt water permeation and biofouling resistance evaluations.

Chapter 4 discusses the experimental results for the transfer of graphene over an electrospun nanofiber PSU mat and different commercial micro/ultra-filtration substrates. Section 4.1 summarizes the Raman spectroscopy results of different CVD graphene (Mono, bi and multi-layer graphene). Section 4.2 focuses on the preparation of a graphene/polysulfone nanofibers mat composite. Preparation of PSU nanofibers was optimized regarding electrospinning parameters, such as the concentration of PSU, voltage applied, solution feed rate, the distance between needle and collector, and finally the needle diameter. After obtaining the optimized conditions, PSU is electrospun directly over graphene. Section 4.3 details the transfer of monolayer graphene onto different commercial microfiltration membranes (substrates). The effect of the substrates' surface characteristics on graphene transferability, such as the surface roughness and wettability, are discussed. Successfully transferred graphene/substrates composites are then characterized by FESEM and KCl ionic transport measurements through them. The section also introduces a method for sealing defects (cracks and tears) introduced within graphene layer during the transfer, known as Interfacial Polymerization (IP) of Nylon 6,6. New graphene procedures developed to transfer hydrophilic substrates are also discussed in Section 4.3. Bi-layer and multi-layer graphene transfer to the polypropylene (PP) substrate are highlighted in Section 4.4 and 4.5 respectively. Finally, Section 4.6 addressing the antifouling nature of graphene after being transferred onto PP substrate. Finally, Chapter 5 provides the main conclusions of the present work.

CHAPTER 2

LITERATURE REVIEW

2.1 Introduction to Graphene

After being debated as unstable materials (thermodynamically) and deemed to be impossible to exist by Landau and co-workers, unexpectedly, a breakthrough was made when a graphene sheet without support was prepared [28-30].

Graphene [31] is simply the two-dimensional (2D) sheet of sp2-tightly packed [30] carbon atoms. Its extended honeycomb carbon network is the basic unit of the other carbon materials such as 3D diamond and graphite (3D) which are infact 2D graphene sheets stacked atop each other [28], carbon nanotubes which are 2D graphene sheets rolled on any axis [32], and fullerenes which are 2D graphene wrapped to give their carbon structure (0D) [33], Figure 2-1 displays these structures.

Some carbon materials were discovered and have been used for centuries (Graphite & diamond), and some others have been discovered and studied during the last twenty five years, namely fullerenes and carbon nanotubes [34].

Graphene has many terms according to carbon-based materials terminology [35]. The term "graphene" denotes one carbon sheet in graphite intercalation compounds and sometimes the "graphene layer" in other production and applications disciplines.

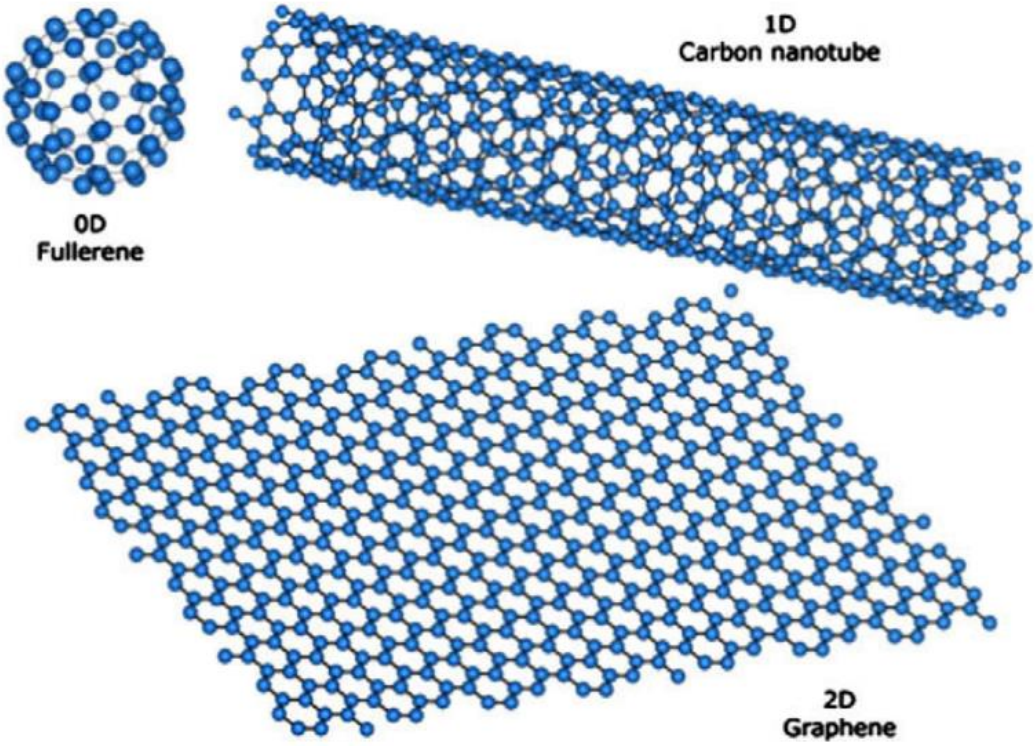

Figure 2-1 Different structures of carbon materials. Adapted from Ref. [34].

In Figure 2-2. Graphene's atomic arrangement includes the lattice (which is the honeycomb arrangement of carbon atoms) and sub-lattices (the two interpenetrated triangular structures shown in Figure 2.2-a) confined within the original lattice structure. Each sub-lattice has a carbon atom at the center of the triangle. The interatomic length between two neighboring carbon atoms (C–C) is about 1.42A° [34]. Graphene sheets stacks on top of each other to form graphite by two different stacking modes: the Bernal mode (alternating ABAB) and the rhombohedral mode (staggered, ABCABC). The interplanar distance of the resulting graphite is 3.45A° [34, 36], with an interaction of van der Waals energy between the layers of about 2 eV/nm^2 [33]. The optimal inter-planar distance for perfectly stacked graphite is considered as 3.45 A°, this spacing can be increased to higher than 1 nm in the case that the planes are rotated with respect to each other. A good example of that are the

GICs (Graphite intercalation compounds), which have a wide range of properties [31, 37, 38].

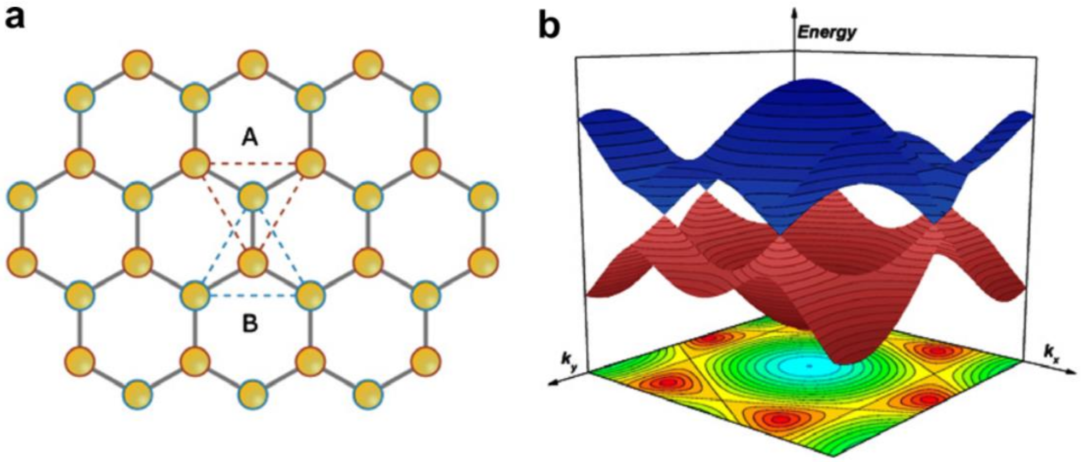

Figure 2-2 (a) The atomic structure of graphene, lattice and sub-lattice triangles A and B with one carbon atom inside each, the C-C inter-atomic distance is 1.42A°, (b) the electronic structure of graphene, the 3D Brillouin zone in red color and the valence in blue. Adapted from Ref. [34]

The carbon atom orbitals: s, px, and py hybridize to produce strong C-C-C covalent bonds with 120°angles and the well-known honeycomb structure shape. A valence bond (filled π orbitals) is formed with the remaining pz orbital of the three neighboring carbon atoms, which overlap over each other. A conduction band (empty π^* orbitals) is formed as well due to overlapping.

The electrical and thermal conductivity of graphene is associated with the valence electrons. While three valence electrons are used to form the covalent bond (σ bond), the remaining valence electron (fourth one) forms the π bond (one-third of neighbors' atoms). The fourth electron will take the z direction and be the one responsible for electrical and thermal conductivities. Compared to the remaining three shared electrons (in-plane one's), it is 103 times lower in both conductivities [31]. The unusual nature of graphene’s mechanical, electrical, and thermal characteristics and properties are with interest of many theoretical and experimental studies.

2.2 Graphene’s History

The 3D structure of graphene (graphite) has been exploited for many centuries (~ 500 years) as a marking material due to the weak force between its stacked planes, similar to the use of pencils nowadays. Graphite nowadays is used as dry lubricant for most industrial applications and has replaced more expensive lubricants such as molybdenum disulfide and boron nitride. Graphite is also used as heating electrodes in the steel industry due to its high thermal capacity (∼3000 W/mK) and electrical conductivity (∼104 Ω^{-1} cm^{-1}) [37, 39]. Graphite is used as a reinforcing agent for composite materials due to the high mechanical strength of its honeycomb structure. Carbon fiber composite materials are used in many different engineering applications. Due to the various applications discussed above, the worldwide demand for graphite has exceeded 1 million tons per year [31].

Graphene’s history is related to a great extent with the discovery of graphite oxide (GO) and its other extracted materials, namely, exfoliated GO and the graphite intercalation compounds (GICs). A German scientist Schafhaeutl discovered graphite oxides and its intercalation compounds in the 1840s when he was trying to insert a small species (such as alkali and acid metal molecules) between carbon graphite sheets. The graphite exfoliation process using nitric and sulfuric acids were reported as well [40].

Almost a decade after Schafhaeutl’s discovery, Brodie (a British scientist) modified Schafhaeutl’s method and showed great advances in estimating graphite’s molecular weight by using the same acids and oxidants, like $KClO_3$ as used today [40]. The use of oxidants not only separated the graphite layer but also oxidized the sheet's surface, which scientists termed graphite oxide (GO).

In 1960, Fernandez-Moran (a well-known electron-microscopist) introduced the micromechanical exfoliation method to separate graphite sheets. He prepared a thin graphite sheet (~15 layers, 5nm thickness) using electron microscopy [34, 41].

In 1962, for the first time, Boehm et al., partially reduced the graphite to a single and bi-layer graphite oxide and observed it under an electron microscope. Boehm concluded, "that his observation confirms the assumption that the thinnest of the lamellae consisted of single carbon layers" [40]. These researchers chemically reduced GO in dilute alkaline-hydrazine (hydrogen sulfide, or iron (II) salts) solution to a thin carbon sheet that has traces of oxygen and hydrogen. The number of layers was determined by comparing the density with known standard films with the aid of transmission electron microscopy (TEM). Similar outcomes were achieved with a process called thermal deflagration; it is used to exfoliate the GO. Despite the fact that Boehm et al. prepared reduced GO, it is not the "pristine graphene" (a graphene one-layer sheet free of contamination), which is a free standing one and could find many applications [40].

In 1969, the adsorption of gaseous organic molecules such as CO, C_2H_4 and C_2H_2C to a metallic surface (platinum) at high temperature was investigated by Morgan and Somorjai. For that, they used the low energy electron diffraction (LEED) process [40].

In 1975, van Bommel et al. [42] showed that, during the elevated temperature heat treatment of silicon carbide (SiC) and with high vacuum, the basal surface is easily covered with a layer of graphite due to the evaporation of silicon atoms.

In the 1990s, after the discovery of carbon nanotubes and fullerenes, electron microscopists started to show a great interest in different kinds of carbon materials not only under microscopes, but also experimentally [34].

In 1995, the IUPAC (International Union of Pure and Applied Chemistry) defined graphene as a single carbon layer of the graphite structure [43]

HOPG (Highly Ordered Pyrolytic Graphite) can be cleaved to yield a nanoscale one graphene-layer thickness by AFM manipulation; the transfer of graphene out of the HOPG to the required substrate was a great challenge for this process [44].

Afterwards, scientists started to prepare thin graphitic discs composed of graphene monolayers. In 1997, fewer than 80 monolayers were described [45, 46], then, fewer than 30 monolayers were achieved (< 10 nm) by rubbing graphite pillars on a support [47]. In 1999, this technique received considerable attention by Ruoff et al. [48], and they proposed its capability to produce single layer graphene.

In 2004, Kim et al. [49], attempted to mount a single graphite microdisc onto the AFM stage and applied a shearing force while controlling the pressure. However, they failed to produce the single layer graphene by this approach.

In 2004, Geim and his group at Manchester University [29, 50], brought the single-layer graphene dream within reach. They used Scotch adhesive tape to repetitively split a graphite crystal down to a single layer graphene; they then transferred the cleaved product onto a SiO_2/ Si wafer and checked it under an optical microscope, as shown in Figure 2.3.

Their groundbreaking experiments in graphite to achieve single-layer graphene won them the 2011 Nobel Prize in Physics [51]. This led to an outburst of interest in graphene as a 2D material, previously believed to be unstable at low temperatures [31, 52].

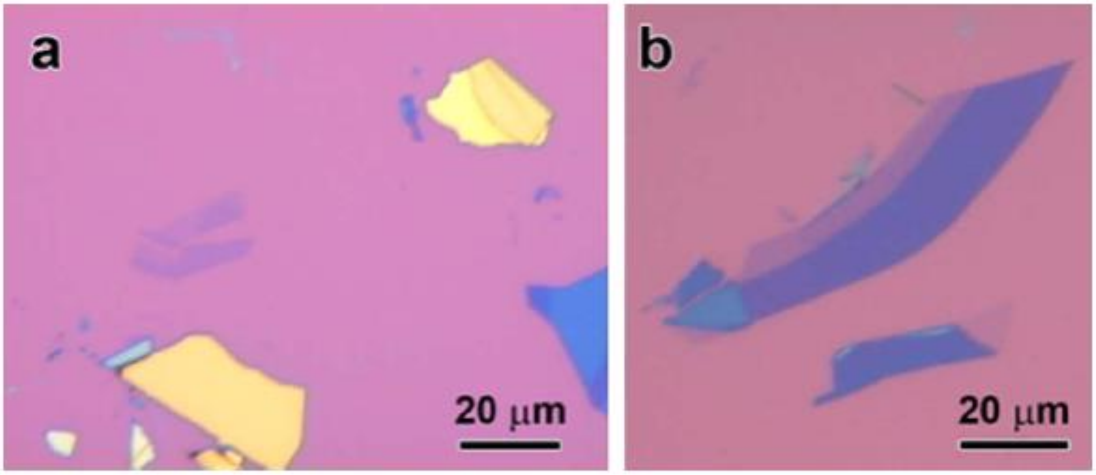

Figure 2-3 Optical micrographs for micro-mechanical exfoliated graphene on a 300 nm SiO_2 substrate, (a) yellow colored zones are for graphite, (b) purple zones are for few-layer graphene (FLG) and the light purple ones for the single-layer. Adapted from Ref. [34].

A few months later, graphene was successfully produced by epitaxial growth on metal carbides, such as SiC (a methodology called sublimation) [53], and by a chemical vapor deposition process (CVD) over metal surfaces such as copper, nickel and ruthenium [54]. For the metal substrates, there are many methods to transfer graphene from the growth substrates to the targeted ones. [55, 56].

Figure 2.4 shows a timeline of the most important stages related to graphene production and characterization.

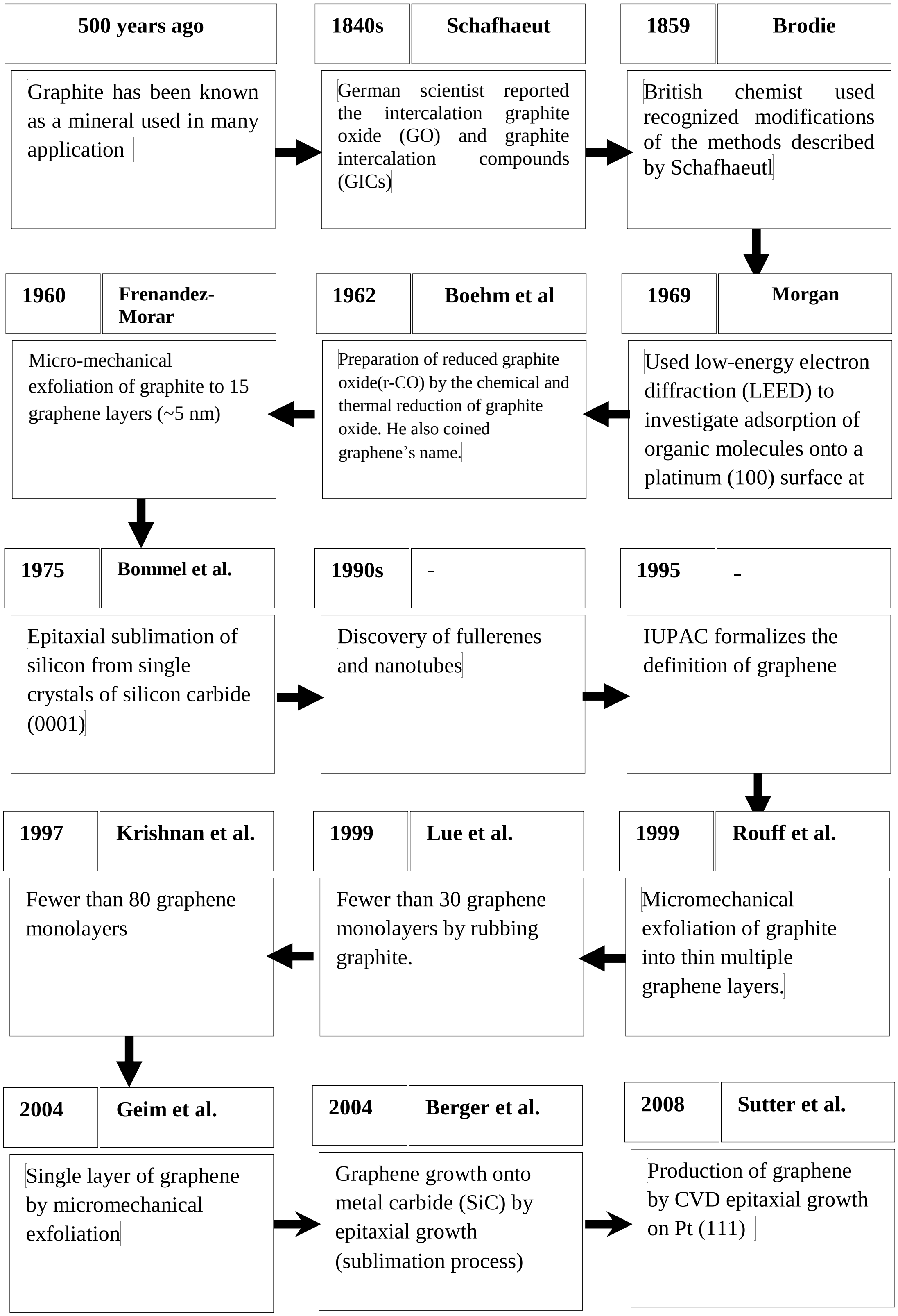

500 years ago
Graphite has been known as a mineral used in many application

1840s **Schafhaeut**
German scientist reported the intercalation graphite oxide (GO) and graphite intercalation compounds (GICs)

1859 **Brodie**
British chemist used recognized modifications of the methods described by Schafhaeutl

1969 **Morgan**
Used low-energy electron diffraction (LEED) to investigate adsorption of organic molecules onto a platinum (100) surface at

1962 **Boehm et al**
Preparation of reduced graphite oxide(r-CO) by the chemical and thermal reduction of graphite oxide. He also coined graphene's name.

1960 **Frenandez-Morar**
Micro-mechanical exfoliation of graphite to 15 graphene layers (~5 nm)

1975 **Bommel et al.**
Epitaxial sublimation of silicon from single crystals of silicon carbide (0001)

1990s -
Discovery of fullerenes and nanotubes

1995 -
IUPAC formalizes the definition of graphene

1999 **Rouff et al.**
Micromechanical exfoliation of graphite into thin multiple graphene layers.

1999 **Lue et al.**
Fewer than 30 graphene monolayers by rubbing graphite.

1997 **Krishnan et al.**
Fewer than 80 graphene monolayers

2004 **Geim et al.**
Single layer of graphene by micromechanical exfoliation

2004 **Berger et al.**
Graphene growth onto metal carbide (SiC) by epitaxial growth (sublimation process)

2008 **Sutter et al.**
Production of graphene by CVD epitaxial growth on Pt (111)

Figure 2-4 Graphene's history timeline.

2.3 Graphene Properties

Graphene (2D material) displays remarkable structure and electronic quality. Due to its unusual electronic properties, graphene has led to the emergence of a new paradigm of condensed-matter physics, where quantum relativistic phenomena exist and, of which are unobservable in high-energy physics [56].

Graphene exhibits exceptional physics; the experimental isolation of monolayer graphene showed graphene’s quantum Hall effect at an ambient temperature, an ambipolar effect, the detection of single molecule adsorption events and an extremely high carrier mobility [34].

Graphene, and most probably its bilayer, has simple electronic spectra (zero-gap semiconductors sometimes called zero-overlap semimetals), having one type of electron and hole. With three layers and above, the electron spectra turn into complicated ones. The valence and conduction bands overlap and multiple charge carriers appear. This can help to distinguish and categorize 2D graphene crystals as a monolayer, bilayer and few-layer (3 to <10) [30].

Graphene optical light absorbance has been measured at about 2.3% [57, 58], as shown in Figure 2.5. The Manchester group saw monolayer graphene under an optical microscope using a simple idea. They have used the interference effect of graphene over (300 nm) of SiO2 on a Si substrate under white lighting that enhances the optical contrast between them. This was one of the most important steps toward the development of this field [31].

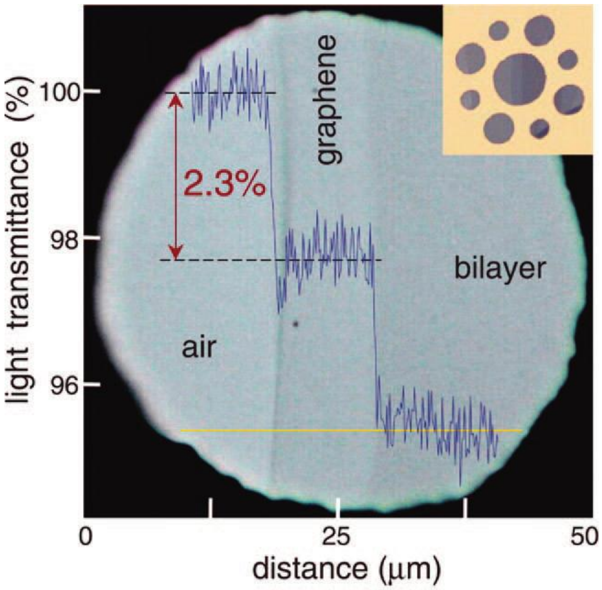

Figure 2-5 Optical light absorbance for single and bilayer graphene samples while suspended on a porous membrane. The upper corner image shows the samples with different openings. Adapted from Ref. [31].

Graphene is very strong (100 times stronger than steel) [14, 59], highly conductive (charge carrier mobility ~ 200,000 cm^2/Vs, which is higher than that of copper) [60], has a high surface area (2630 m^2/g) [61], is highly thermally conductive (~5000 W/mK, which is 10 times greater than copper) [62, 63], and flexible [16, 25, 64].

The unique physical and chemical properties offers graphene as the new, unusual and exciting material to reach a massive level of research attention. Global efforts to investigate and utilize its fundamental properties are truly underway, and graphene holds great promise for future advances within many scientific fields where it has already been utilized to enhance a large number of specific technological applications [51].

2.4 Graphene Production Methods

Various fabrication routes exist for graphene production, including mechanical [30, 65] and chemical exfoliation [66-68] of high-quality graphene, direct growth on metal or carbides substrates using the chemical vapor deposition process (CVD) [69-71], and chemical routes via graphene oxide and unzipping of carbon nanotubes [72].

At present, no single fabrication route that produces graphene sheets are suitable for all potential applications, as every route has its advantages and disadvantages [34, 51]. Several important criteria must be considered when selecting the route to graphene. Most important is the quality of graphene, followed by production concerns such as the production rate and sheet size (large-area graphene). Graphene grown over copper (Cu) by chemical vapor deposition has been found to be the most used among the other preparation processes [73]. The basic principle of the CVD process is to decompose a carbon-based gas using heat to provide a source of carbon that can then re-arrange to form graphene over a catalyst substrate [74]. The CVD process is cost effective, and not only gives reasonably high quality but also offers a large area of graphene [51, 75-77] and the sheets produced can be transferred to other substrates or used directly in an application [56, 78, 79].

These routes could be classified in different ways. Table (1) shows the Top-down and the Bottom-up approaches for graphene production classification.

Table 2.1 Top-down and Bottom-up approaches for graphene production.

Top-down Approach	Bottom-up Approach
Mechanical exfoliation	Epitaxial growth on metallic or metal carbide substrates.
Thermal decomposition of carbides	Molecular approach
Graphite oxide reduction	
Wet chemical routes	
Unrolling of carbon nanotubes (CNTs)	

Table 2.2 gives a comparative overview of different fabrication methodologies of graphene regarding the quantity, quality, and applicability, along with their essential advantages and disadvantages [80, 81].

Many important factors should be kept in mind when thinking about the scalability of graphene. **Firstly**, the fabrication route must produce a good quality 2D crystal lattice to guarantee ultimate electron mobility. **Secondly**, it must control the properties through the thickness to ensure a good application performance [31].

2.4.1 Mechanical Exfoliation (top-down approach)

The force required to separate one graphite layer (exfoliation process) is very low due to the very weak van der Waals energy between different layers (~ 2 eV/nm^2); the magnitude of this force is about 300 $nN/\mu m^2$ [49]. To exfoliate a single graphene layer, the van der Waals attraction between subsequent graphene layers (e.g. the first and second ones) must be exceeded without affecting other layers [31].

The mechanical exfoliation process produces the highest quality graphene [76] compared with other top-down approaches, but one of the disadvantages is the lack of process scalability.

For instance, slicing a sample of high ordered pyrolytic graphite (HOPG) with adhesive tape is suitable to investigate the physical properties of graphene and provides low cost with high quality [28], Nevertheless, shortcomings including low yield, lack of reproducibility, and the labor-intensive work make it difficult to scale up for mass production and limits it for fundamental studies only. Also, the graphene could become contaminated with adhesive tape material.

Mechanical exfoliation was first prepared by rubbing arrays of graphite micro-pillars with a sharp glass tip [47]. In the next step, the glass tip is again used to repetitively exfoliate sheets from the graphite crystal [82]. Mechanical exfoliation can also be

Table 2.2 Various graphene fabrication methodologies commonly applied to obtain graphene with some comparisons between them. Adapted from Ref. [51].

Fabrication method	Graphene precursor	Operating conditions	Advantages	Disadvantages	Application implications
Mechanical exfoliation	HOPG	Scotch-tape	Direct, simple, high structural and electronic quality, low cost	Delicate and time-consuming (hours), low yields, poor reproducibility, possible contamination of sample from the adhesive tape utilized.	Fundamental research. High quality single layer graphene sheets obtained with little lattice defect density and domain sizes ranging from 500 Å up to 10 µm
Chemical exfoliation	Graphite	Dispersion and exfoliation of graphite in organic solvents or through the use of surfactant complexes	Direct, simple, large-scale production, low-cost, high yield, practicability of sample handling (liquid suspension)	Time-consuming (hours), impure, possible contamination of sample from surfactant or solvents utilized	General graphene research for modified substrates. Often multiple layered graphene incorporated with structural defects originating from the fabrication process with domain size ranging from 500 Å up to 1500 Å
Reduction of GO	Graphite	Graphite exfoliation and oxidation, subsequent reduction of exfoliated graphite oxide	Facile scalability, high yields, low cost, excellent processability, practicability of sample handling (liquid suspension)	Indirect, large number of structural defects, disruption of the electronic structure of graphene owing to impurities, reduction to graphene is often not complete	General graphene research for modified substrates. Often multiple layered graphene incorporated with structural defects originating from the fabrication process with domain size ranging from 500 Å up to 1500 Å
CVD epitaxial growth	Hydro carbon gas (predominantly)	CVD under variable temperatures and pressures	Large-scale production, high qualities, uniform films, tailoring of graphene quality possible	High temperature requirements, high cost, complicated process, variable yields	Fundamental and basic research. High quality single layer graphene sheets obtained with little lattice defect density, however, graphene can be tailored to contain specific defects and impurities where these are required for beneficial implementation in given devices. Layer thickness and domain sizes are thus variable

CVD: chemical vapor deposition; **GO**: graphene oxide; **HOPG**: highly orientated pyrolytic graphite.

achieved by mounting a single micropillar on an AFM cantilever under controlled shearing force and pressure [49]. Unfortunately, the above two mechanical exfoliation approaches do not allow for the production of monolayer graphene [34]. In 1999, Ruoff et al. [48], patterned a small pillar of highly oriented pyrolytic graphite (HOPG) by plasma etching and manipulated it using the atomic force microscope (AFM) tip (Figure 2.6). The slabs observed under the microscope were more than or equivalent to 600 layers (200 nm thickness). Kim et al. [83], enhanced the method to get ∼30 layers (10 nm thickness) on SiO_2 by transferring the micro-pillars to a tipless cantilever.

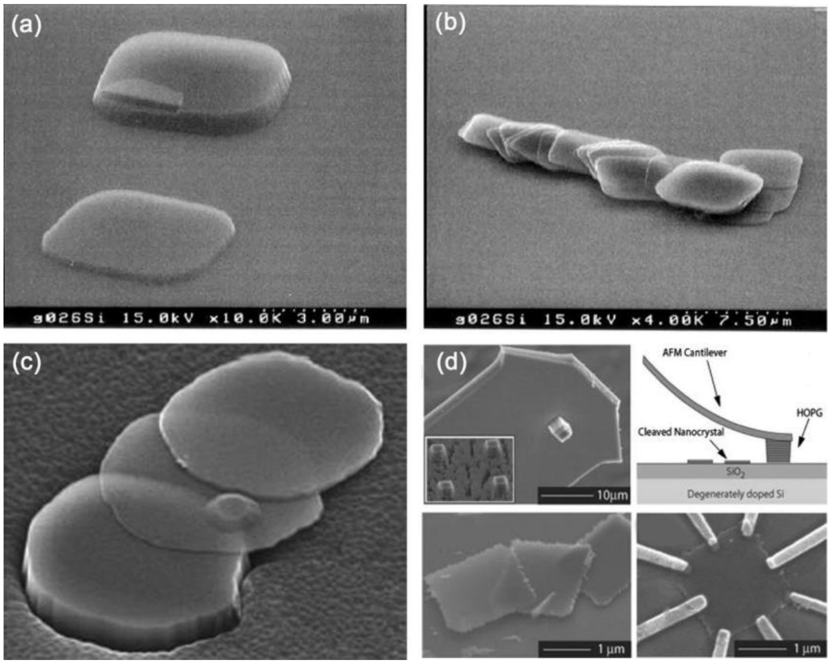

Figure 2-6 SEM micrographs of the first attempts to mechanically exfoliate graphite pillars. (a and b) Ruoff et al. peeled away layers with an AFM tip, (c and d) Kim et al. transferred the pillars to a tipless cantilever and deposited thin slabs onto other substrates in tapping mode. Adapted from Ref. [31].

In 2004, a much simpler fabrication methodology that resulted in the first isolation of single layer graphene was accomplished by Novoselov and Geim [29] (a Manchester group, see Figure 2.7). The method involves using common Scotch adhesive tape to stick and peel a dozen times, which transforms a thick graphite sheet (~1 μm) into an ultimate thin monolayer graphene. The graphene is then transferred onto a special substrate (usually 300 nm SiO_2 on top of Si wafer for optical contrast [75]) by a gentle press of the tape [29]. The graphene is then examined under a microscope and Raman spectroscopy to distinguish the location of single-layer (SLG), Bi-layer (BLG), few-layer (FLG) and multilayer graphene (MLG).

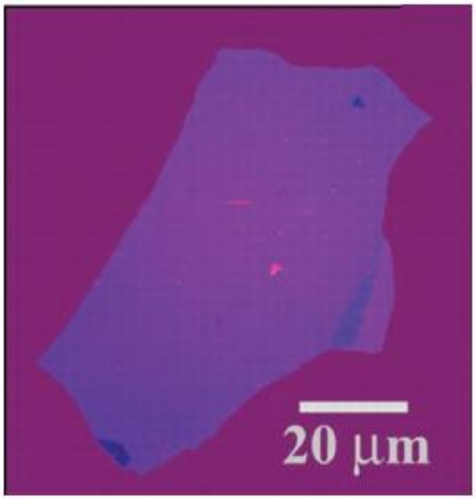

Figure 2-7 Optical microscopy of single layer graphene observed by Geim et al. at Manchester University. Adapted from Ref. [31].

As with other fabrication techniques, drawbacks exist. The drawbacks of the tape technique are mainly due to the glue residues left on the sample surface and the difficult implementation of the method for mass production. It needs a great deal of patience, as depositions put down by inexperienced scientists are often a mess of thick slabs in which locating a single layer can be extremely difficult. With practice, the technique results in high-quality crystallites, which can be more than 100 μm2 in size [31].

The residues are then found to affect and limit the graphene carrier mobility [84, 85]. To avoid such residue contamination, applying high voltages to promote graphene adhesion with the substrate was reported to be effective [86, 87].

In the end, the mechanical exfoliation process is the best fabrication technique regarding the structural and electrical quality of graphene obtained, primarily because it starts with a high-quality of graphite source [34].

2.4.2 Supported Growth

Since 1970s, there are two main different approaches to produce graphene by growing it onto solid ceramic/metallic substrates: the top-down approach by thermal decomposition of carbides, and the down-top approach, by the epitaxial growth of graphene onto metal carbide or metallic substrates by the chemical vapor deposition process (CVD) of hydrocarbon gases [34].

2.4.2.1 Thermal Decomposition of Carbides (*top–down approach*)

Researchers at the Georgia Institute of Technology initiated a fabrication technique to produce graphene, called the epitaxial method. The principle is to prepare graphene by reducing silicon carbide (see Figure 2-8) [88-90]. At a high temperature (1000°C - 1300°C) and ultrahigh vacuum, silicon atoms desorb from the substrate surface leaving behind batches of carbon-enriched sites (graphitization) [42, 91]. Recently, researchers used photolithography to make graphene devices by patterning epitaxial growth in prearranged places [92].

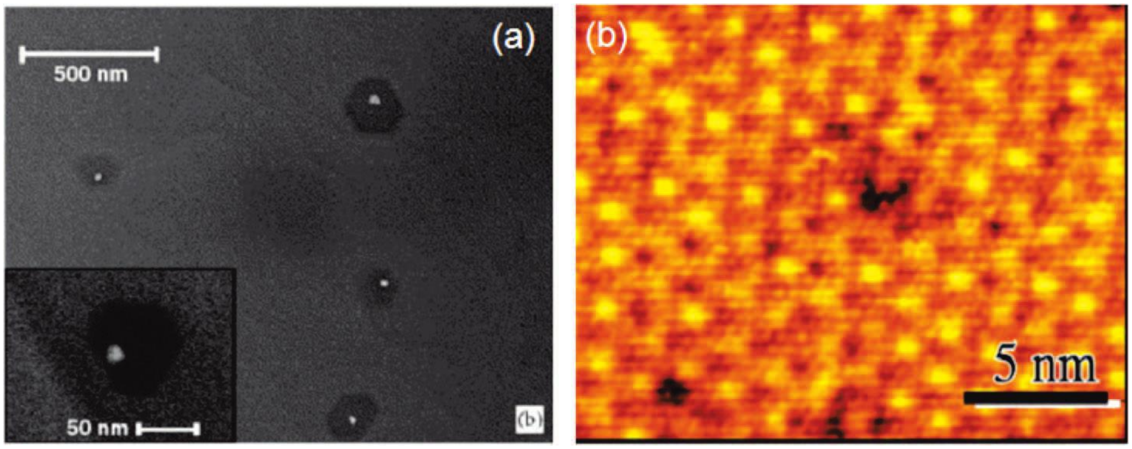

Figure 2-8 High-temperature sublimation of silicon carbide (SiC) to graphene carbon-rich zones (a) SEM image shows small hexagonal crystallites. (b) STM image shows long-range order and a low density of defects. Adapted from Ref. [31].

Varied thicknesses and limited lateral extension of graphene crystallites were noticed due to the formation of deep pits along with surface roughening that is induced during the sublimation of silicon atoms [34].

Sublimation of silicon atoms occurs at 1500°C under argon, compared to 1150°C with an ultra-high vacuum. Thus, high-temperature annealing of SiC (1650°C) improves the quality of produced graphene [34].

Other carbides have been used to produce graphene by a sublimation process. Particularly, the decomposition of ethylene gas on a titanium carbide (TiC) surface [93, 94] and on a tantalum carbide (TaC) surface [95, 96] yields monolayers graphene areas.

This technique is suitable for radio electronics, where the excellent performance of the devices could offset the cost of the SiC wafers, since the price of the SiC wafer is somewhat higher than that of silicon [76].

2.4.2.2 Chemical Vapor Deposition (CVD) (Graphene Epitaxial Growth onto Metal Carbide and Metallic Substrate) *(down– top approach)*

The main idea of the chemical vapor deposition process (CVD) is to decompose carbon-rich gases, with the help of heat, to act as source of carbon atoms source that then relocate to form a 2D graphene network at the top of the catalyst surface [97]. To grow graphene, carbon-rich gases (hydrocarbons) are exploited as precursors, and the most effective substrates are some of the transition metals (such as nickel and copper) [98, 99]. Table 2.3 describes a few examples of variable CVD process conditions and the resultant graphene quality.

Carbon-rich gas (commonly ethane or methane) is introduced in a reducing environment at high temperatures (~1000^oC) in the presence of a transition metal catalyst. The metal catalyst provides a media for the freed carbon atoms from the gas phase to adsorb (in the case of Cu) or segregate (in the case of Ni) and reassemble on its surface forming graphene sheets [99].

Transition metals have partially filled d-orbitals, or form intermediate chemical compounds that adsorb and trigger reacting constituents which facilitate low energy routes for reactions [76]. It is important to maintain a relatively high pressure during growth, if the experiment is performed under vacuum, to prevent evaporation of the metal catalyst at elevated temperatures [75].

Table 2.3 Variable CVD fabrication recipes (conditions) applied and the resultant impact on graphene quality. Adapted from Ref. [51].

Substrate /catalyst	Temperature /°C	Gas reaction mixtures (precursors)	Growth time	Special conditions	Graphene grain size	Thickness of graphene layer	Graphene quality
Nickel	1000, cooling rate ~10 °C s^{-1}	CH_4：H_2：Ar at 50：65：200 standard cubic centimeters per minute (sccm). Ambient pressure	7 minutes	Nickel thickness less than 300 nm deposited on Si/SiO_2substrate. Prior annealing of nickel substrate utilized	≤ 20 µm	~1 to 12 layers	Highly polycrystalline surface, small grain sizes and multilayered regions of graphene result in an extremely large degree of edge plane surface defects in the graphene film
Nickel	1000, cooling rate of 100 °C min^{-1}	CH_4 at 10 sccm, H_2 at 1400 sccm. Ambient pressure	5 minutes	Nickel thickness ~500 nm deposited on Si/SiO_2substrate. Prior annealing of nickel substrate utilized	3–20 µm	1, 2 and multi layered graphene regions occupy up to 87% of the film area and single layer coverage accounts for ~5–11% of the overall film	Highly polycrystalline surface, small grain sizes and areas of few layered graphene islands result in a large degree of edge plane surface defects in the graphene film
Copper	800, cooling rate not specified	H_2/CH_4 at 5 sccm and partial pressure 0.39 Torr (Ar at 80 sccm, 1 Torr)	10 minutes	Copper foil (206 nm thick)	~10 µm	1, 2 and 3 layers	Few crystallographic orientations and edge plane defects present at the grain boundaries and at variable multiple layer graphene areas
Copper	1000, cooling rate 40–300 °C min^{-1}	H_2/CH_4 at 0.06 sccm and partial pressure 0.5 Torr	< 3 minutes	Copper foil (25 µm thick)	10 µm	~95% 1 monolayer	Few crystallographic orientations and few defects present at the grain boundaries with ~5% being multiple layer graphene
Copper	~1035, cooling rate not specified	CH_4 at a flow rate and partial pressure less than 1 sccm and 50 mTorr respectively	>1 hour	Copper foil (25 µm thick) enclosure utilized	0.5 mm	1 monolayer	Single crystallographic orientation, high purity defect free single graphene crystals

Advantages of CVD process:

1. Cost effective and widely used as a fabrication route to produce a high-quality graphene [77].
2. Suitable for large area graphene synthesis [75, 77].
3. Produces defect-free and high-quality monolayer graphene with less contamination and controlled orientation [35].
4. The produced graphene layers can be transferred to target substrates [56, 78, 79] or used directly for an application.

Disadvantages and challenges of CVD process:

1. Controlling the formation of a single layer over sheet thickness while stopping the formation of multiple layers [31].
2. Although the CVD process provides large-area graphene compared to the other fabrication routes, it is difficult to scale it up to a larger scale graphene application [51].
3. Since the CVD process is performed at high temperate, it is difficult to grow graphene on insulating substrates (plastic, silicon dioxide, glass and so on) which are often necessary for many applications [100].
4. Graphene transfer to the application substrate is not straightforward since many defects (such as tears and cracks) can be developed during the transfer process [51].

Catalyst Metals (Substrate):

With the CVD method, graphene is synthesized onto many different transition metals, such as iridium (Ir) [101, 102] , ruthenium (Ru) [54, 100, 101, 103], nickel (Ni) [69, 104-107] , palladium (Pd) [108-110], cobalt (Co) [109], rhenium (Re) [111], platinum (Pt) [112], and copper (Cu) [71].

Transition metals and some of their compounds are good catalysts because of the partially filled d-orbitals and the formation of intermediate compounds that desorb and activate the species reaction at the surface of the metal. Catalysis by metals comes from their capability to provide low energy paths for reactions, either by the facile change of oxidation states or by the formation of appropriate intermediates.

In the early trials, ethylene gas decomposed on Pt substrates at ~800K and formed uniformly distributed graphene nano-sized islands. Annealing above 1000K formed a continuous layer and additional regularly shaped and large islands [34].

Recently, large domains of monolayer graphene were grown on Ru substrates by CVD of ethylene gas [54]. At 1420 K, Ethylene gas is dissolved on a ruthenium surface, and when the temperature is decreased to 1100 K, a supersaturation is prompted, which triggers the nucleation and formation of graphene [113].

The first graphene monolayer adheres strongly to the metal surface, whereas the second one is weakly bonded. The first layer acts as an adhesion layer that efficiently screens off the residual charges from the underlying substrate [34].

Graphene CVD growth on copper and nickel substrates showed major improvements regarding large area growth, better quality and transfer of graphene from the metal substrate to the application substrate [100]. Lately, developments on uniform monolayer graphene deposition on copper foils over large areas have provided access to high-quality material [76].

For that reasons copper and nickel will be the only transition metals to be covered in this literature. Ni CVD will be highlighted, but copper CVD will be explained in detail.

Nickel CVD:

Although the nickel substrate showed a major improvement in graphene production, graphene growth on nickel is often characterized by a large numbers of layers [51] and a lack of distribution over the entire substrate surface [106]. There are many factors which limit the size and quality of graphene grown onto the Ni substrate: high carbon solubility, small graphene domain sizes and segregation of carbon upon cooling inside the Ni grain, as well as grain boundaries [114].

Progress was made to produce graphene with a few layers uniformly distributed along the larger area, which was achieved *via* annealing of the nickel substrate surface to get a larger grain size, above which graphene would grow [69, 115]. Nevertheless, there are still some essential limitations as mentioned above.

As one of the limitations related to the substrate material, the phase diagram of Ni and C (Figure 2.9) shows the increase of carbon solubility in nickel metal at high temperature (>800^{o}C). The Ni and C at this temperature joins and forms a solid solution alloy. The solubility is decreased by lowering the temperature, causing carbon to diffuse out of the Ni.

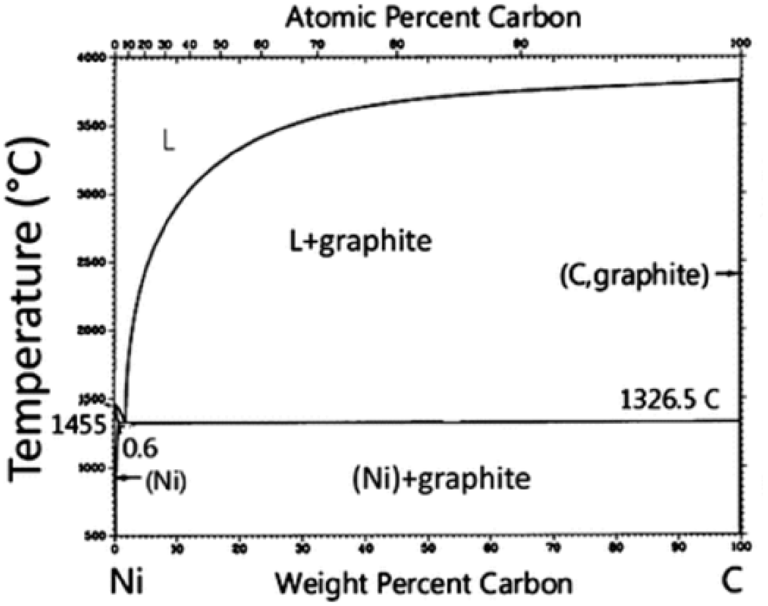

Figure 2-9 Binary phase diagrams of Ni and carbon. Adapted from Ref. [76].

The number of graphene layers varies along the Ni surface. The metastable compound (Ni_3C) promotes the precipitation of carbon atoms out of nickel. Since the grain boundaries have much higher energy compared to the grain itself, carbon preferentially precipitates at the grain boundaries to form multi-layer graphene, whereas fewer layers are grown on each grain. So, graphite thickness above the Ni grains is considerably less than that above the grain boundaries [76].

Graphene grown onto Ni can be transferred to any arbitrary substrate. The nickel layer can be easily dissolved in acidic solutions (e.g. dilute hydrochloric solution). The graphene is transferred to a polymer coating before transferring to the required substrate [69, 115] as shown in Figure 2.10.

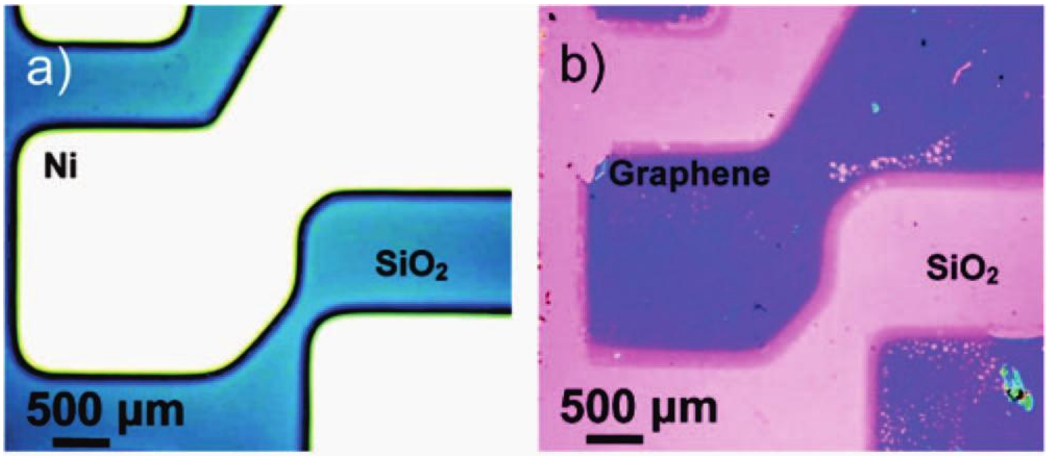

Figure 2-10 Nickel-grown graphene. (a) Optical image of a pre-patterned Ni film on SiO2/Si. CVD graphene is grown on the surface of the Ni pattern. (b) Optical image of the grown graphene transferred intact from the Ni surface in (a) to another SiO2/Si substrate. Adapted from Ref. [116].

Copper CVD:

Copper has been used as a catalyst for the growth of different types of carbon materials such as diamond, carbon nanotubes, graphite, and currently graphene [117]. unlike Ni, the Cu catalyst has gathered substantial interest as a result of its ability to grow a large area of monolayer graphene, with a domain size equal to the largest domain created by mechanical exfoliation [118].

Early [119] and subsequent follow-on [120-127] research studies have validated the growth of monolayer graphene with areas as large as 30 inches. In some studies, the copper catalyst was able to grow monolayer graphene covering 95% of the total surface area and the remaining 5% was covered with 2-3 layers graphene [117, 119]. The good coverage is due to the very low solubility of carbon atoms in copper and the grain growth after the annealing process, which facilitates the growth of graphene onto large surface areas [128]. The graphene growth onto nickel occurs *via* a carbon segregation followed by a precipitation process [129], whereas growth onto copper starts with an adsorption process that helps to control the formation of monolayer graphene over the large areas [119, 129]. Once the catalyst surface is totally covered with monolayer graphene, the growth of the next layers is stopped because of the absence of an uncovered catalyst. The catalyst plays a vital role in decomposing the carbon-rich gases. On the other hand, nickel has high carbon solubility and the segregation–precipitation process facilitates dissolving additional carbon atoms and, therefore, obtaining multi-layer graphene [129].

Thin copper films are cheap and can be easily etched by different copper etchants such as ferric chloride; this will help to transfer graphene readily to the required substrate [117].

Table 2.4 summarizes the growth parameters that can be applied to achieve the best graphene growth onto a Cu catalyst. As pointed out in the Table, copper foil thicknesses were found in the range of 25–50 µm [117].

Table 2.4 Summary of CVD parameters found in literature for the growth of graphene onto copper. Adapted From Ref. [117].

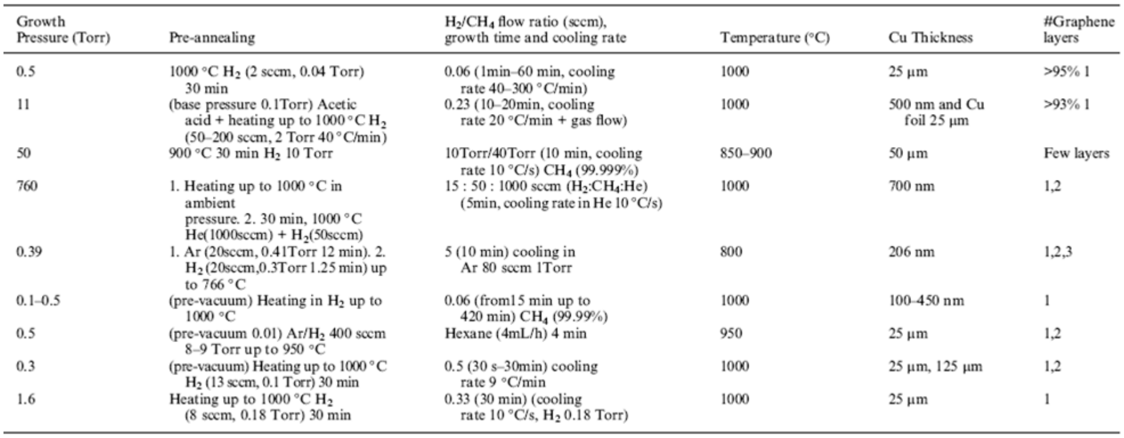

Growth Pressure (Torr)	Pre-annealing	H_2/CH_4 flow ratio (sccm), growth time and cooling rate	Temperature (°C)	Cu Thickness	#Graphene layers
0.5	1000 °C H_2 (2 sccm, 0.04 Torr) 30 min	0.06 (1min–60 min, cooling rate 40–300 °C/min)	1000	25 µm	>95% 1
11	(base pressure 0.1Torr) Acetic acid + heating up to 1000 °C H_2 (50–200 sccm, 2 Torr 40 °C/min)	0.23 (10–20min, cooling rate 20 °C/min + gas flow)	1000	500 nm and Cu foil 25 µm	>93% 1
50	900 °C 30 min H_2 10 Torr	10Torr/40Torr (10 min, cooling rate 10 °C/s) CH_4 (99.999%)	850–900	50 µm	Few layers
760	1. Heating up to 1000 °C in ambient pressure. 2. 30 min, 1000 °C He(1000sccm) + H_2(50sccm)	15 : 50 : 1000 sccm (H_2:CH_4:He) (5min, cooling rate in He 10 °C/s)	1000	700 nm	1,2
0.39	1. Ar (20sccm, 0.41Torr 12 min). 2. H_2 (20sccm,0.3Torr 1.25 min) up to 766 °C	5 (10 min) cooling in Ar 80 sccm 1Torr	800	206 nm	1,2,3
0.1–0.5	(pre-vacuum) Heating in H_2 up to 1000 °C	0.06 (from15 min up to 420 min) CH_4 (99.99%)	1000	100-450 nm	1
0.5	(pre-vacuum 0.01) Ar/H_2 400 sccm 8–9 Torr up to 950 °C	Hexane (4mL/h) 4 min	950	25 µm	1,2
0.3	(pre-vacuum) Heating up to 1000 °C H_2 (13 sccm, 0.1 Torr) 30 min	0.5 (30 s–30min) cooling rate 9 °C/min	1000	25 µm, 125 µm	1,2
1.6	Heating up to 1000 °C H_2 (8 sccm, 0.18 Torr) 30 min	0.33 (30 min) (cooling rate 10 °C/s, H_2 0.18 Torr)	1000	25 µm	1

Even though, most commonly selected CVD temperature is at 1000^{o}C, the process has also been performed at temperatures ranging from 800–950^{o}C [123, 130]. Regarding pressures, CVD is done at an atmospheric pressure of precursor gases [124] and even at lower pressures (0.5–50 Torr) [131]. Order of centimeters of monolayer graphene was grown onto copper using methane as a source of carbon. The film reported by Li et al. [119]was continuous across a large copper surface area with a low percentage (less than 5%) of the area being covered with a few layers.

Effect of Precursors

There are many different precursors (carbon-rich gases) used to produce graphene *via* the CVD process. One study [132] discussed the effect of precursors, namely the ethanol, methanol and propanol on the quality of fabricated graphene under the same fabrication conditions. Large area (3x3 cm^2), high-quality graphene was reported in the case of each precursor utilized.

A scanning electron microscope (SEM) micrograph and Raman spectra of the fabricated graphene are shown in Figure 2.11, as well as some insights about the morphology of the graphene layer.

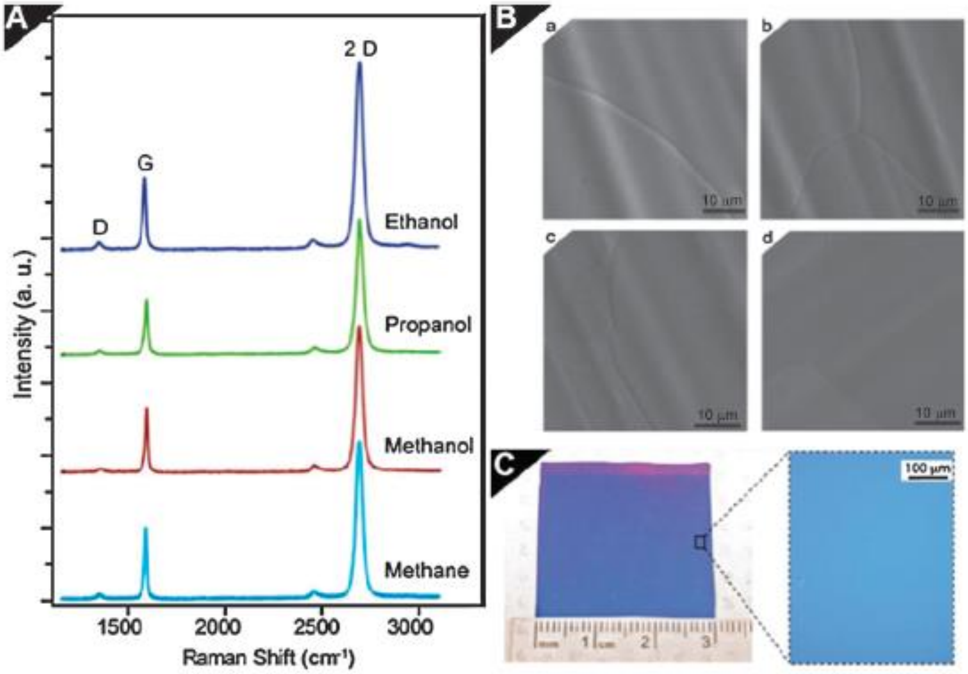

Figure 2-11 (A) Raman spectra of a monolayer CVD graphene transferred onto SiO_2/Si using different precursors. The 2D peak (I= 2700 cm^{-1}) is more than twice as high as the G peak (I= 1580 cm^{-1}), which indicates the high quality of monolayer graphene. (B) SEM micrographs of graphene on 25 µm copper foil substrates, with different precursors (a) methanol, (b) ethanol, (c) 1-propanol, and (d) methane. The images show the presence of copper surface steps and graphene wrinkles that result from the difference between the thermal expansion coefficient of graphene and copper, indicating that the graphene film is continuous and uniform. (C) A 3 x 3 cm2 CVD graphene was grown using methanol transferred to a SiO2/Si substrate. Adapted from Ref. [133].

Graphene growth onto copper starts with the decomposition of a methane precursor gas just over the copper surface at 1000°C. The growth of mainly monolayer graphene on copper foil has recently been reported using hexane at 950°C as well [125].

In other outstanding and relatively cutting-edge work [134], monolayer graphene crystals with large domains were grown by low-pressure CVD onto copper foil using methane gas as a precursor. Electron microscopy observations showed that the graphene domains had a single crystallographic orientation and in some rare cases, domains had two orientations. SEM micrographs of the fabricated graphene are shown in Figure 2.12.

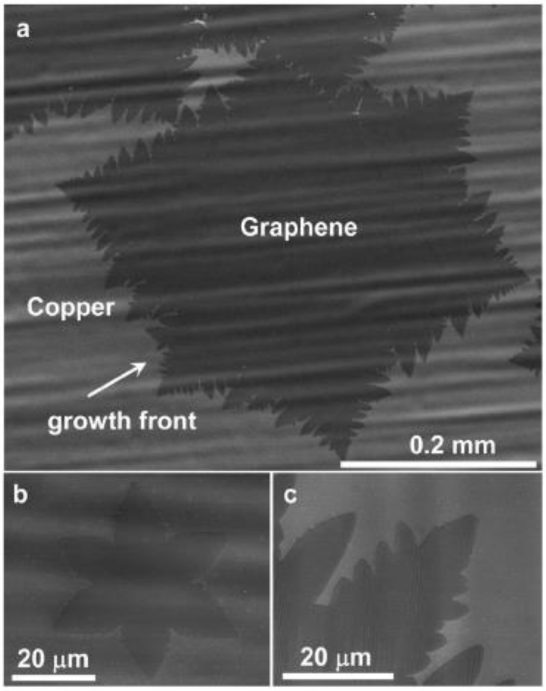

Figure 2-12 SEM micrographs of CVD graphene grown onto copper, (a) Grown graphene domain with average growth rate of ~6 mm min^{-}1, (b) graphene nuclei formed during the initial stage of growth, (c) graphene domain edge finger indicated by the arrow in (a). Adapted from Ref. [133].

Effect of Catalyst (Copper) Grain Boundary:

Unfortunately, most of the graphene fabricated by the CVD process is polycrystalline (has many domains) [135]; its mechanical, as well as electronic properties, are weakened at its domain boundaries [136, 137]. Additionally, copper grain boundaries act as the source of defects in graphene [138], and thus the degree of defect coverage will intensely influence the fabricated graphene properties.

However, at present, the percentage area of monolayer graphene coverage onto nickel is ~87%, while, for copper foils, the average is ~95%. This seems excellent and perfectly suitable for different applications [133].

The growth process passes through three stages as illustrated in Figure 2.13. Firstly, Cu foil covered with copper oxide is placed inside the CVD reactor. Copper oxide is reduced, by annealing at high temperature, in an atmospheric hydrogen environment. Grain growth and annihilation of surface defects also occur during this stage. Figure 2.13-b shows the second stage, where uniform nucleation of graphene domains occurs. The initial domains have different lattice orientations and follow the orientation of the Cu grains beneath. When growth time is increased, graphene domains size is increased as well, and finally they merge to form a continuous graphene layer [117].

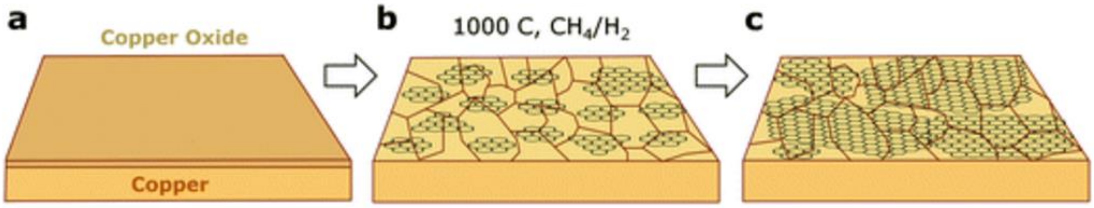

Figure 2-13 Schematic illustration for the three major steps of CVD graphene onto copper, (a) as received copper foil with copper oxide; (b) nucleation of graphene domains by exposure to CH_4/H_2 gases at 1000°C, (c) growth of the graphene domains. Adapted from Ref. [117].

There is a possibility to adjust and control the nucleation size and density of the initial graphene domains by manipulating the pretreatment parameters, the partial pressure of the methane gas and the overall growth pressure. Formation of multilayered graphene will not be continued even after further exposure to the carbon-rich precursor. It is not completely the case with graphene growth onto Ni foils, where the grain boundaries host significant thickness during growth [115, 139]. The weak adhesion between graphene and the Cu substrate allows the graphene to cover grain boundaries with the least structural defects [117].

Copper substrate pre-treatment

Pretreatment of the copper foils plays an important role in the fabrication of large graphene domains [117]. It serves several important purposes that guarantee high-quality graphene growth. **First**, the Cu foil is covered by different Cu oxides such as CuO and Cu_2O [140], which decreases its catalytic behavior. Consequently, annealing of Cu substrate in a hydrogen reducing environment at 1000°C removes these oxides [141] and increases the grain size of copper to enable growth of graphene domains. Usually, annealing takes 30 minutes, while a shorter duration has been reported with thin Cu films (less than a micrometer) [117, 122, 123, 131]. Acetic acid wet chemical pretreatment [142] has also been found to remove Cu_2O [117].

Future of CVD:

It is suspected that further work on the CVD growth of graphene utilizing copper will yield graphene with fewer bilayer regions and larger grain sizes. CVD holds great promise for the commercial production (cheap, fast, straightforward and scalable process) of large-area high-quality uniform mono-layer graphene films that are readily transferable and have the possibility of being made bespoke, when required, in terms of controllable defect density (nickel vs. copper), the presence of specific functionalities (oxygenated species), grain orientation/size and the incorporation of impurities (dopants) to specifically tailor to one's needs [133].

Another remaining challenge for the epitaxial and CVD methods is obtaining fine control over the film thickness while preventing secondary crystal formation. In an ideal case, both methods rely on the nucleation and growth of a single crystal without the formation of a boundary or seeding of a second layer. Currently, the best specimens have a variation in thickness of perhaps 1-3 layers and are polycrystalline [116].

2.4.2.3 Graphene Oxide Reduction and the Wet Chemical Routes

In contrast to the mechanical exfoliation fabrication processes, chemical exfoliation relies on weakening the van der Waals interaction force between graphite flakes by the incorporation of reactants between the interlayer spaces. Afterward, the released layer stacking is disrupted when the intercalant decomposition produces a high gas pressure. Consequently, the sp2 structure is partially reduced into a sp2 and sp3 sheet that has less π–π stacking strength. Chemical exfoliation could be used as a large-scale graphene production route since it is done in suspension, and this will improve the scalability of the process [143].

150 years ago, Brodie and co-workers [144] oxidized graphite into less aromatic carbon to determine carbon’s atomic weight and chemical exfoliation has only slightly progressed since then [145].

The oxidative intercalation of potassium chlorate in concentrated nitric and sulphuric acid produced new modified graphite flakes composed of highly re-hybridized carbon sheets carrying carboxyl and hydroxyl functional groups. This solution was primarily named as graphitic acid, but now it is called graphite oxide (GO) [146].

In 1958, Hummers and Offeman [147] reported a safer and faster fabrication procedure to produce graphite oxide. Graphite powder is mixed with a mixture of potassium permanganate, sodium nitrate, and hot sulfuric acid for many hours, keeping the temperature at 45°C [146].

Graphite intercalation compounds (GICs) produced by the intercalation of acids between the graphite layers are commonly called Expandable Graphite [148, 149]. In such graphite, the layers keep in contact but the inter-layer spacing is considerably increased, so that the volume is increased 100 times compared with natural graphite.

After the intercalation of graphite, single or a few layers are obtained by disintegrating the intercalated layers by thermal or chemical means, which produces the evolution of gases in the van der Waals space. Annealing at high heating rates such as 2000°C/min to reach 1050°C makes a CO_2 over pressure that helps in splitting the graphite oxide into separate individual layers, first observed by TEM in 1962 [146, 150-152].

Graphite oxide can be also separated into individual graphene oxide layers by an ultrasonication process (chemical means). When non-oxidized graphene is the major constituent, the solution appears as a greenish-blue color, whereas it is yellow when the concentration of graphene oxide is high [146].

Thermal shock of Graphite intercalation compounds (GICs) will increase the interlayer spacing and produce the “expanded” graphite, which is a well-known starting material for recent methods such as the synthesis of nanoribbons (see Figure 2.14) [153, 154].

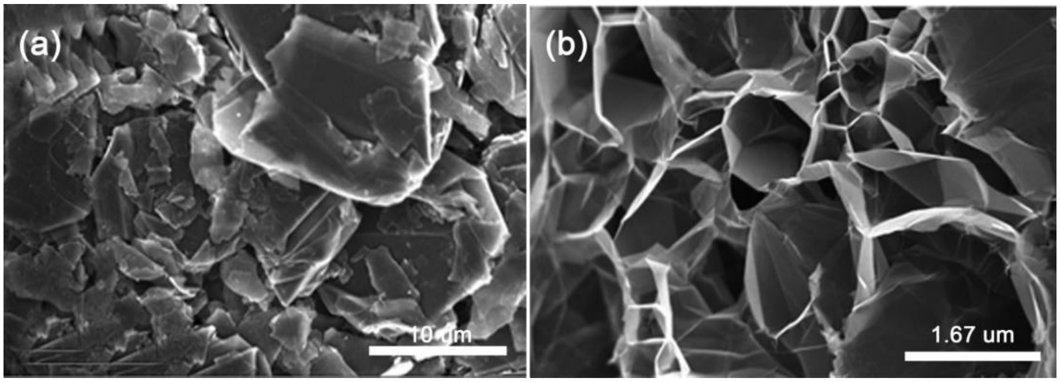

Figure 2-14 Scanning electron micrographs (SEM) of graphite, (a) before reduction, (b) after expansion by acid intercalation and thermal shock. Adapted from Ref. [116].

Despite current efforts to enhance the chemical route to graphene, the reduction from graphite to graphene remains incomplete, in which the process produces an intermediate material graphene oxide and graphene.

In 2013, researchers tried aggressively to react the potassium intercalation compound (KC_8) product with different solvents such as alcohols. The product (a graphite slab) with 30 layers was metastable and easy to scroll under high-power sonication (see Figure 2.15) [153, 155, 156].

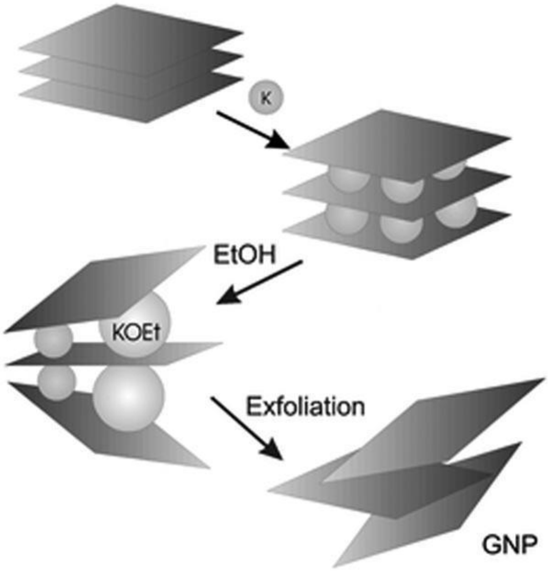

Figure 2-15 Schematic drawing of exfoliation process that produces thin graphite slabs (~30 layers). Potassium is inserted between the graphite layers and aggressively reacted with alcohols. Adapted from Ref. [116].

In 2006, Ruoff et al. [157, 158], demonstrated for the first time a solution-based process (chemical process) to produce monolayer graphene (see Figure 2.16). The process modifies the graphite chemically to produce graphite oxide (GO). With graphite first oxidized by Hummers' method, the GO produced will have layers of sheets stacked with an AB stacking arrangement; the GO is then completely exfoliated by the addition of mechanical energy [159]. The strong interaction between water and the oxygen functional groups, such as epoxide and hydroxyl in the basal plane of graphite oxide, drives water to intercalate between the layers and break them into individual ones [116].

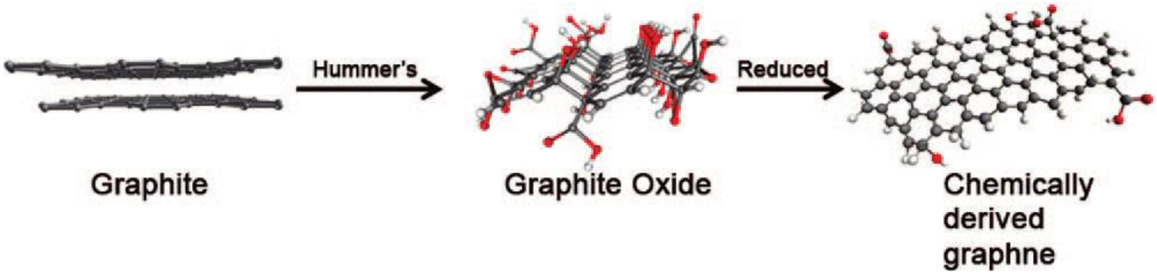

Figure 2-16 Molecular schematic shows the conversion of graphite to chemically derived graphene. Adapted from Ref. [116].

The advantages of the modified Hummer's method are its low-cost and scalability. Graphite is the starting material, and the method can readily produce large quantities of chemically derived graphene suspended in a liquid [116].

One challenge faces this process: the removal of oxygen-based functional groups may cause the reduced sheets to become less hydrophilic and quickly aggregate in solution [116].

Another method [128] includes applying ultrasound treatment in both the intercalation and solution steps. For instance, the ultra-sonication route uses water–surfactant solution [160] that forms encapsulation layers on the graphene's sides. A second application of ultrasound will transform the graphite oxide into monolayer graphene

[160, 161]. It is easy to produce high yield graphene with lower cost compared with the procedures above.

2.4.2.4 A molecular approach

When graphene domain sizes exceed a few hundreds of nanometers, the observed behavior is well described by condensed matter models of mesoscopic phenomena. Graphene is intrinsically composed of the 2D pavement of organic molecular entities, benzene rings, which confer to graphene its Janus character, with one face showing a 2D mesoscopic gas of π electrons, and the other face showing properties sensitive to the arrangement of molecular rings and edge atomic chains. To investigate the truly nanometer-scale regime, bottom-up approaches have been explored, which consist of starting from carbon precursors of small, yet well-defined, size and to converting them to graphene. One of the first strategies is the thermodynamic conversion of nano-diamond clusters into nanometer-sized graphene islands [146].

2.5 Graphene Transfer Methods

To make the CVD method more feasible and reliable to large scale applications, there must be a consistent method for transferring graphene from growth substrates to more applicable substrates [162]. Currently, graphene transfer onto desired substrates using various methods is implemented in two ways: the wet transfer method and dry transfer method. The most straightforward wet transfer method is to etch the metal away chemically to obtain free floating graphene composites that can be scooped onto chosen substrates. Other well-known wet etching methods include the standard transfer method [56], the direct transfer method [162] and the roll-to-roll transfer method [163].

Graphene on insulating substrates such as glass, SiO_2/Si wafers, and plastic sheets is required for different applications and more specifically, in electronic applications.

2.5.1 Standard Transfer Method

The standard transfer method depends primarily on using a temporary substrate which acts as a rigid support during etching of the metallic growth substrate. The polymer coatings mainly are polymethyl methacrylate (PMMA) or polydimethylsiloxane (PDMS); it also prevents folding and tearing of the graphene layer [56]. The process shown in Figure 2.17 starts with a spin coating of PMMA or PDMS on top of CVD graphene. The cured PMA/graphene/Cu is then floated over a copper etchant, such as ferric chloride, to remove the copper layer and leave graphene supported by a polymeric coating. The delicate graphene/PMMA film is washed by de-ionized water baths and transferred by fishing or scooping to the target TEM grid. Finally, the PMMA is lifted with acetone, and the graphene/TEM grid is rinsed in isopropanol (IPA) [162].

Unfortunately, the use of these polymers requires some wet etching and chemical steps that contaminate the graphene and can also damage it.

Copper is removed by wet etching using chemicals such as ferric chloride; this chloride was observed to leave some iron residue, causing, contamination of the graphene surface [164], which is a serious problem in some of the applications [51].

Different etchants in addition to ferric chloride [$FeCl_3$ in HCl/ H_2O (1M-5M)] [165, 166] can be used for copper etching such as: HCl, HNO_3 [167, 168], $Fe(NO_3)_3$ in H_2O

(1M) [79] and $(NH_4)_2SO_8$ (0.1M) [163] . Although $CuCl_2$ can be reused multiple times by a regeneration process, it is not commonly used due to its high toxicity compared with other etchants [76].

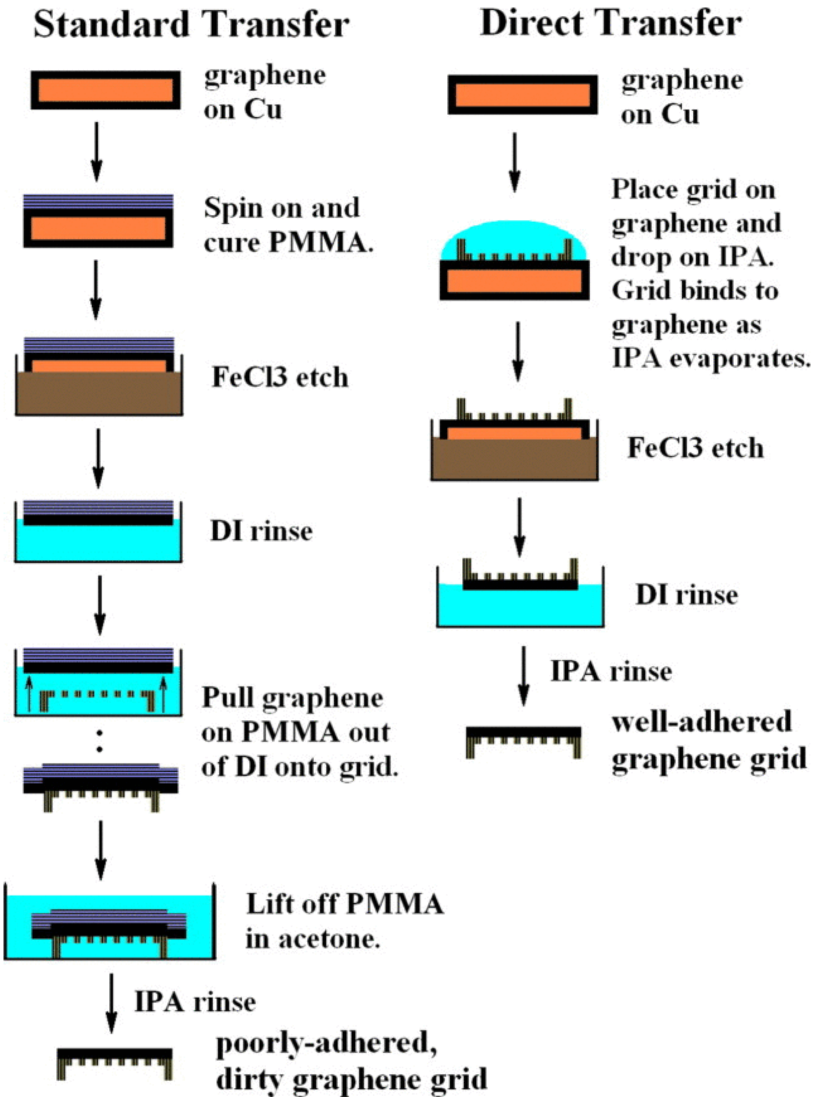

Figure 2-17 standard (e.g., PMMA) transfer method left side compared with the direct transfer method right side. Adapted from Ref. [162].

$FeCl_3$ removes copper effectively without leaving any gaseous products or precipitate. Therefore, it is most commonly used [169]. On the other hand, etching copper with nitric acid leads to the formation of H_2 gas bubbles that may cause cracking in the graphene layer. The HCl etching rate is very low and discharges corrosive vapor. The HNO3 etchant can also damage the graphene structure network.

After copper etching, the graphene is rinsed in water and fixed to the application substrate before removing the support layer, which finally leaves a single layer of graphene on the target surface [100].

Recently, it has been reported that the copper foil can be evaporated off following the growth, to leave grown graphene standing directly on the application substrate [170]. This procedure will be useful for direct deposition of graphene onto any substrate without transfer [76].

Graphene cracking and tearing due to the method of transfer initially used, and the intrinsic mechanical properties of monolayer graphene are the main disadvantages of the standard transfer method.

To minimize such cracks and tears within transferred graphene, it is critical to maintain good adhesion between the transferred graphene layer and the target substrate. Substrate hydrophobicity and surface roughness controls this adhesion. Substrate pre-treatment by hydrophobic self-assembled monolayers [perfluorophenylazide (PFPA) [171] and aminopropyl-triethoxysilane (APTES) [172]] can also improve the adhesion of graphene [76].

Li et al. [79] improved the contact between graphene and the substrate support by adding a second PMMA layer; they obtained a graphene film with a much lower cracks and tears density.

2.5.2 Direct Transfer Method

The direct transfer method is gentler and cleaner compared to standard transfer methods. It is perfect for the fabrication of a wide range of electronic, chemical and optical devices that need a uniform, large graphene domain [162]. To avoid damage of the graphene film during the Cu etching step, a stiff substrate support is preferred. In the standard transfer method, a polymer support such as PMMA is coated *via* spin-coating, whereas in the direct transfer method, the target substrate acts as the support, such as the TEM grid. To attach the graphene, the TEM grid is placed on top of the CVD graphene/Cu, and a drop of isopropanol (IPA) is gradually placed on top of the grid to wet both the grid and the underlying graphene [162]. Surface tension and the evaporation of IPA are used to attract the graphene/Cu with the TEM target and at the same time, provide a rigid graphene support during the Cu etching step. As the IPA evaporates, surface tension draws the graphene and grid together into intimate contact [173].

To reach the maximum adhesion strength, the evaporative surface tension must be strong enough to warp either the Cu foil or the TEM grid, so the TEM target thickness and Cu foil must be selected carefully [162].

Optical microscopy was used to confirm the adhesion quality between the graphene and TEM grid; manifest contrast differences between non-adhered and adhered regions were observed using optical interference analysis [162]. Figure 2.18.

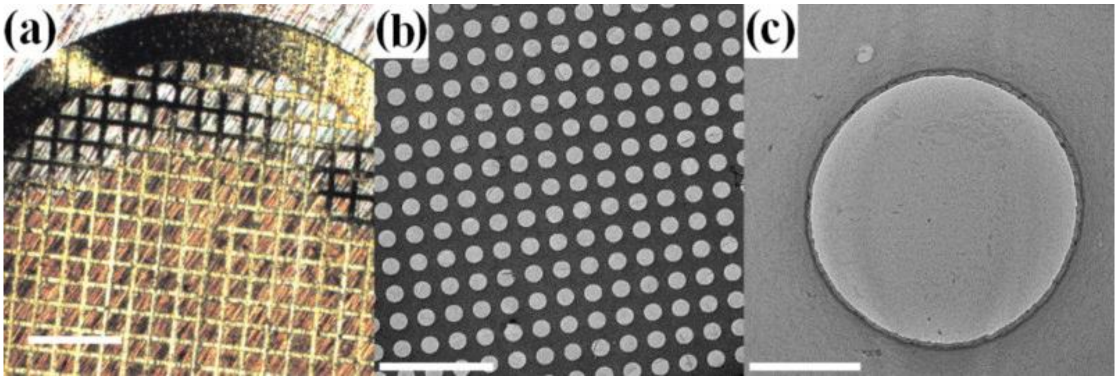

Figure 2-18 (a) Optical micrograph of complete adhesion between graphene/Cu and TEM grid (top edge not yet adhered). Scale bar =0.5 mm, (b) part of a grid frame showing large graphene. Scale bar =10 µm, (c) single graphene domain covering the TEM hole. Scale bar =0.5 µm. Adapted from Ref. [162].

Baking the sample on top of a hot plate for 10 to 20 minutes at 120 °C evaporates any remaining IPA, and therefore strengthens the graphene/TEM grid adhesion. After removing the Cu foil by floating the sample over an $FeCl_3$ (0.1 g/mL) solution for 2 hours, it is washed with de-ionized (DI) water and rinsed in IPA to remove any organics and Cu etchant [162].

2.5.3 Roll – to – Roll Transfer

One group of researchers [163], successfully transferred graphene onto a thermal release tape by utilizing the roll-to-roll method. Figure 2.19 shows the roll-to-roll transfer of a graphene film grown on a flexible plastic support. The thermal adhesive tape is proposed to be the key for transferring very large area graphene from copper to plastic substrates. A plastic substrate, up to 30 inches diagonally, (Figure 2.19-c) was obtained. The authors validate a large area touchscreen and claim excellent uniformity over the entire substrate. Some residual thermal tape is also apparently transferred onto the substrate, as indicated by the bright patches in the image in Figure 2.19-d of a single layer graphene. However, after three transfer cycles, a relatively clean surface, free of defects, is visible [76] (Figure 2.19-e).

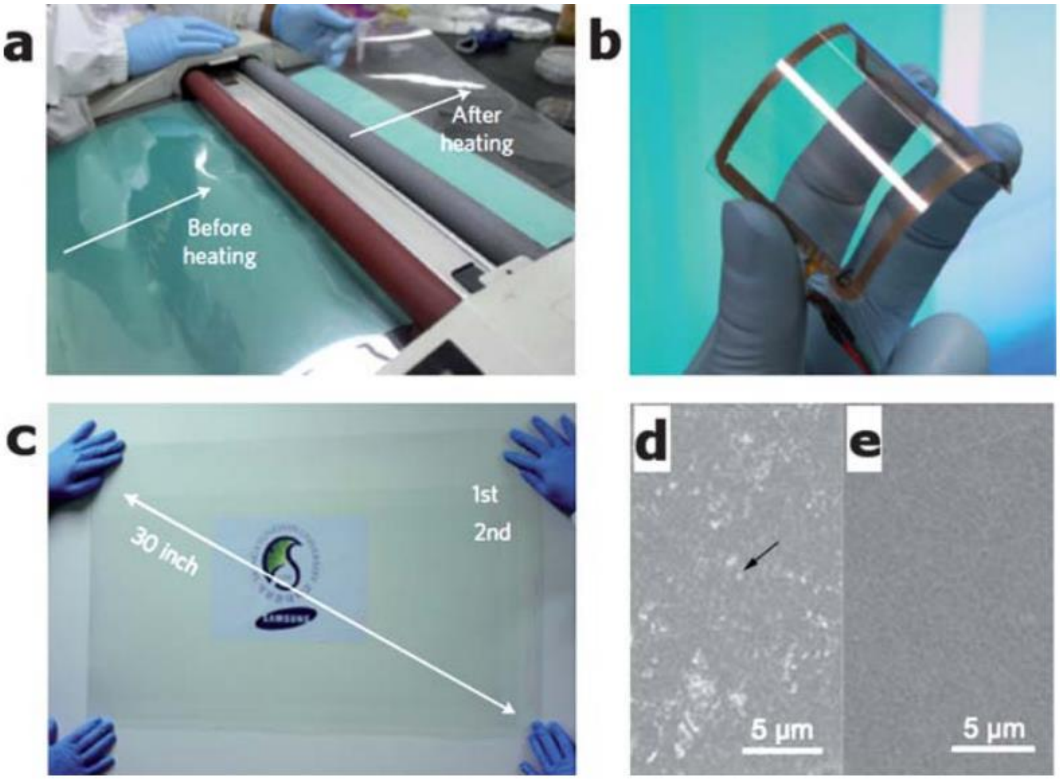

Figure 2-19 (a) Transfer of graphene onto PET substrates by roll-to-roll method at 120°C using thermal release tape, (b) a flexible graphene/PET touch screen panel, (c) 30 inch graphene/PET sheet, (d) SEM micrograph of monolayer graphene transferred, the arrow indicates tape residues and some defects, (e) SEM micrograph of a three layers of graphene transferred. Adapted from Ref. [163].

2.6 Graphene Characterization

There are many different characterization techniques used to study and identify the graphene quantitatively and qualitatively.

2.6.1 Optical Microscopy

Monolayer graphene on an appropriate substrate shows optical contrast under an optical microscope at a specific wavelength range. Graphene on top of commonly used SiO_2/Si wafers adds a small optical path to the Fabry-Perrot cavity created by the SiO_2 layer on silicon; by modifying the SiO_2 thickness to 90 or 300 nm, the reflected light intensity is maximal at about 550 nm [174]. The method consists of displaying the green channel image normalized by its value on the bare substrate [34]. The short optical path, added by graphene as thin as a monolayer, can be easily seen by the contrast between graphene and the substrate can then be as high as 12% [34] (Figure 2.20).

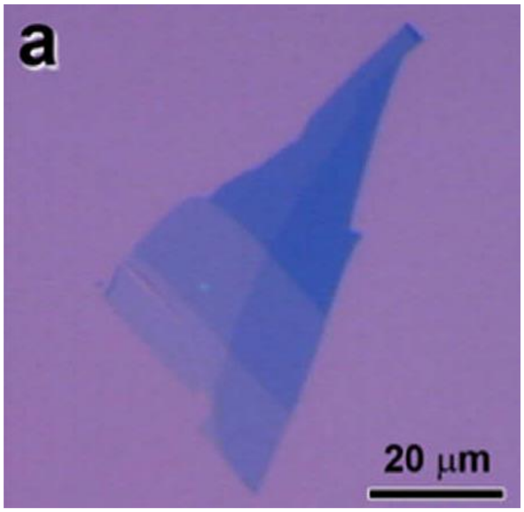

Figure 2-20 Optical micrograph of graphene over SiO2/Si wafer under an optical microscope. Adapted from Ref. [34].

Graphene is also visible on 50 nm Si_3N_4 using blue light [174], 72 nm Al_2O_3 on silicon wafer [175], and on 90 nm polymethyl-methacrylate (PMMA) using white light [176].

Although the interference effect of optical microscopy is a good method for recognizing thin materials, it might not distinguish whether graphene is mono, bi, or multilayered. It is important to know how many graphene layers are produced since most of the remarkable properties of graphene are dependent on its thickness [31].

2.6.2 Atomic Force Microscopy (AFM)

Atomic force microscopy (AFM) was one of the first techniques employed to prove that the thinnest graphitic flakes first identified optically were monolayer graphene [34].

However, a question immediately arises: what should the apparent height of graphene be on a SiO_2 substrate with a typical 1-nm RMS roughness? [34]. Surprisingly, a single-layer graphene on oxidized wafers consistently appears to be 0.8–1.2 nm thick with any supplementary layer on top of it adding the expected 0.35 nm thickness, which corresponds to the native van der Waals inter-layer distance [177].

Although AFM is too slow and limited in lateral scan size to be used as a primary identification method, and despite the apparent extra height, AFM soft imaging modes are the best way to monitor the topological quality of substrate-supported graphene samples during the successive steps of device processing [34].

2.6.3 Transmission Electron Microscopy (TEM)

TEM has recently arisen as a structural characterization tool for suspended graphene that can span low magnification imaging, as well as atomic-scale details as shown in Figure 2.21.

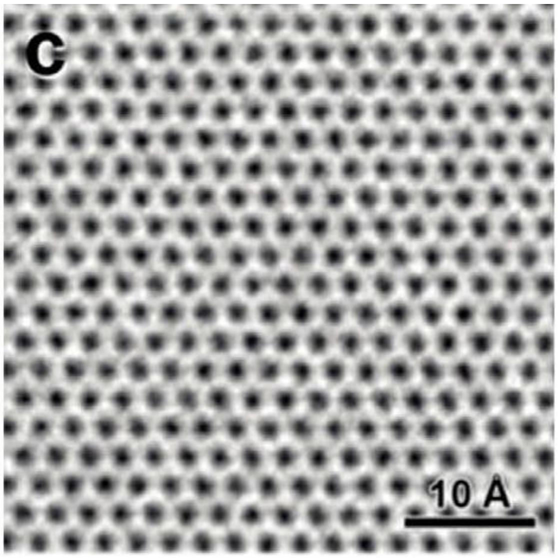

Figure 2-21 TEM (Transmission Electron Microscope) Image for Graphene Identification. Adapted from Ref. [178].

Moreover, single-atom thick graphene makes suspended graphene the ideal support film for high-resolution, spherical aberration-corrected TEM studies of individual defect sites [34].

Moreover, single-atom thick graphene makes suspended graphene the ideal support film for high-resolution, spherical aberration-corrected TEM studies of individual defect sites [65, 179] and adsorbed atoms as light as carbon and hydrogen [178].

Electron diffraction studies can be used to qualitatively distinguish a single from a bilayer, since both exhibit a six-fold symmetry, but the ratio of the intensities for the [2110] and [1100] spots is inverted [180] for the two objects as predicted by Horiuchi et al. [181].

2.6.4 Angle-Resolved Photoemission Spectroscopy (ARPES)

It (ARPES) provides direct evidence of the electronic structure of graphene and other carbon-based materials, and it should be mentioned here [34].

When shining a substrate with 10–300 eV photons, photoelectrons are extracted from the substrate surface, the momentum and energy of which can be analyzed with as little as 15 meV resolution to reconstruct the energy band diagram (Figure 2.22) [182]. In the case of graphene, the relativistic Dirac-like linear dispersion near the Brillouin zone K corner [183, 184] and the chirality of the charge carriers can be directly observed, as well as the emergence of small band gaps due to graphene inter-layer or substrate-graphene interactions [184].

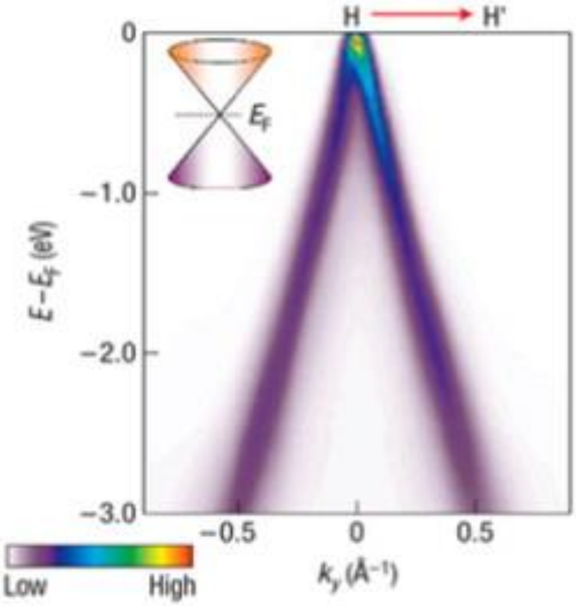

Figure 2-22 Energy band diagram of graphene. Adapted from Ref. [34].

2.6.5 Raman Scattering

Raman scattering is a fast and non-destructive technique that provides direct insight into the electron–phonon interactions, which implies a high sensitivity to electronic and crystallographic structures [34].

It has therefore been extensively applied to the structural investigation of carbon materials, and more particularly, of nanotubes [38].

Raman spectra of carbon materials show similar features in the 800–2000 cm^{-1} region, which is also of interest for graphene [185-187]. The G peak at around 1560 cm^{-1} corresponds to the E_{2g} phonon at the center of the Brillouin zone. The D peak, at 1360 cm^{-1}, is due to the out-of-plane breathing mode of the sp_2 atoms and is active in the presence of a defect [188].

The D band is an efficient probe to assess the level of defects and impurities in graphene. It is, for example, completely silent for high-quality graphene such as that obtained by micromechanical exfoliation, except in proximity to the edges. However, a major fingerprint of graphene is the D’ peak (sometimes labeled as 2D peak) at about 2700 cm^{-1} (Figure 2.23) [34].

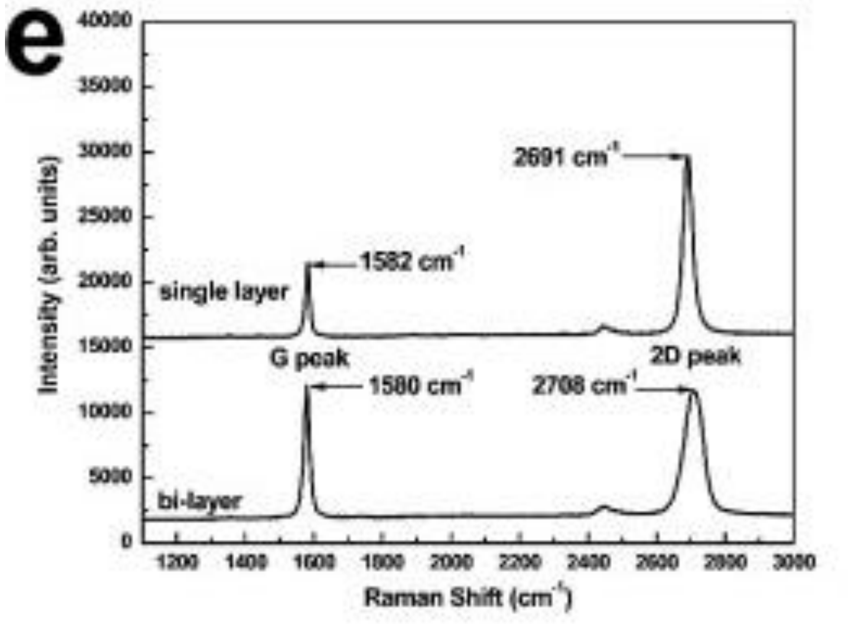

Figure 2-23 Raman spectroscopy of graphene. Adapted from Ref. [34].

The shape, position, and intensity relative to the D band of this peak depend markedly on the number of layers [189, 190].

The isolated graphene monolayer exhibits a symmetrical Lorentzian peak centered on 2640 cm^{-1} that can shift to 2655–2665 cm^{-1} for loosely stacked graphene layers, as in SiC-templated graphene [189].

For two or more layers, a second peak centered on 1685 cm^{-1} emerges and eventually dominates the first peak for more than three layers. Beyond five layers, the Raman multi-peak profile becomes hardly distinguishable from that of bulk graphite, which is a complex group of bands between 2600 and 2750 cm^{-1} [185].

Ultimately, it was not a directly topographical technique, but instead Raman spectroscopy that emerged as the most useful way to probe the thickness of mechanically exfoliated flakes. Although less than obvious, this makes good sense because the features of graphite and graphene directly reflect changes in electronic structure from the stacking of successive layers 80-86. Observations of gradual changes in the Raman spectrum allow one to infer the number of layers (up to the screening length) in a "fingerprint" fashion (see Figure 2.24) [31].

The major features of the Raman spectra of graphite and graphene are the G band at ∼1584 cm^{-1} and the 2D band at ∼2700 cm^{-1}. The G band is due to the E_{2g} vibrational mode, and the 2D band is a second-order two-phonon mode. A third feature, the D band at ∼1350 $cm\text{-}^{1}$, is not Raman active for pristine graphene but can be observed where symmetry is broken by edges or in samples with a high density of defects. changes in the positions and relative peak heights of the G and 2D bands indicate the number of layers present for a given flake. The location of the G peak for single layer graphene is 3-5 cm^{-1} higher than that of bulk graphite, while its intensity is roughly the same. The 2D peak shows a significant change in both shape and intensity as the number of layers is decreased. In bulk graphite, the 2D band is comprised of two components, the intensities of which are roughly 1/4 and 1/2 that of the G peak for the low and high shifts, respectively. For single layer graphene, the 2D band is a single sharp peak at the lower shift, with an intensity roughly 4 times that of the G peak. It was investigation of these trends that finally enabled scientists to reliably confirm the identity of mechanically exfoliated flakes [31].

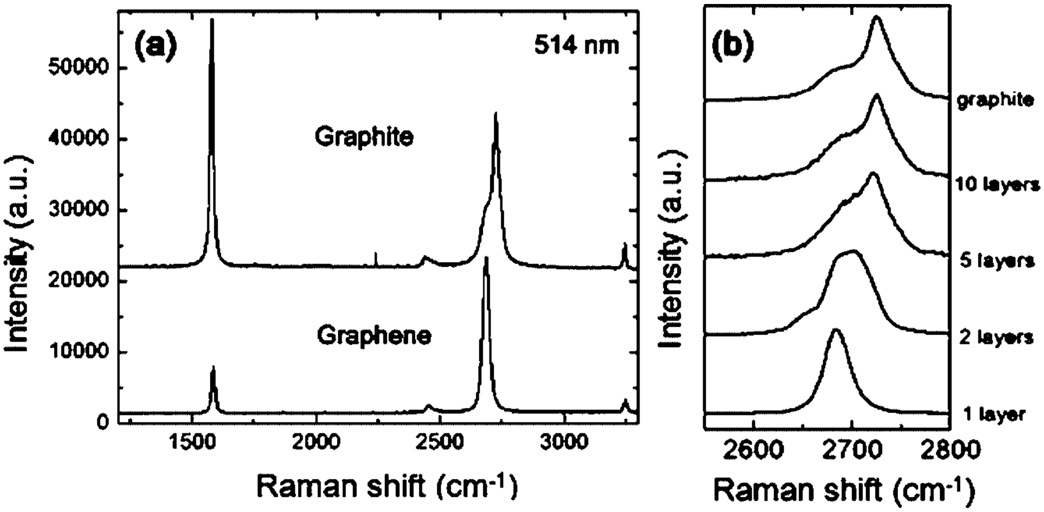

Figure 2-24 Raman spectroscopy of graphene. Both the G (near 1584 cm^{-1}) and 2D (near 2700cm^{-1}) peaks undergo significant changes due to the thickness of AB-stacked flakes. Adapted from Ref. [31].

2.6.6 Rayleigh Scattering

In contrast to Raman spectroscopy, Rayleigh scattering results from the elastically scattered photons that are much more abundant. Therefore, a Rayleigh scattering measurement is five orders of magnitude faster than Raman scattering [34].

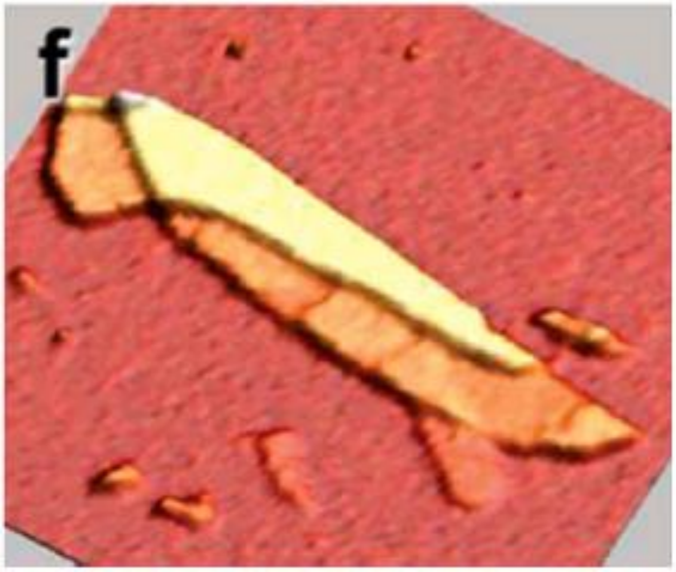

Figure 2-25 Rayleigh scattered image of graphene. Adapted from Ref. [31].

Rayleigh scattering has been shown to offer another quick and non-invasive method to image graphene, and even identify the number of layers of a given sample (N < 6) since the monochromatic contrast varies linearly with thickness, as shown in Figure 2.25 [191]. The contrast of 0.08 at 633 nm (He–Ne laser), with a dependence on the frequency of the incident light with a spatial resolution of 800 nm, has been found experimentally [34].

2.6.7 Scanning Tunneling Microscope (STM)

Scanning tunneling microscopy (STM) has long been used to observe the electronic topography of graphite [192-194]. In these experiments, only three carbons of the six-member rings are visible due to the AB stacking of graphite (see Figure 2.26) [195]. In this arrangement, the electron density is considerably higher for the three R-carbons (those that eclipse carbons in the sheet just below), and hence, they are the only ones visible by STM. This is as opposed to what was expected for single layer graphene, in which the six carbons are completely equivalent and thus should all appear with equal intensity. This was indeed confirmed by ultrahigh vacuum STM images taken at Columbia by Flynn and others [195]. Their measurements also gave evidence of the high crystal quality of mechanically exfoliated samples, which showed few-to-no defects over tens of nanometers [31].

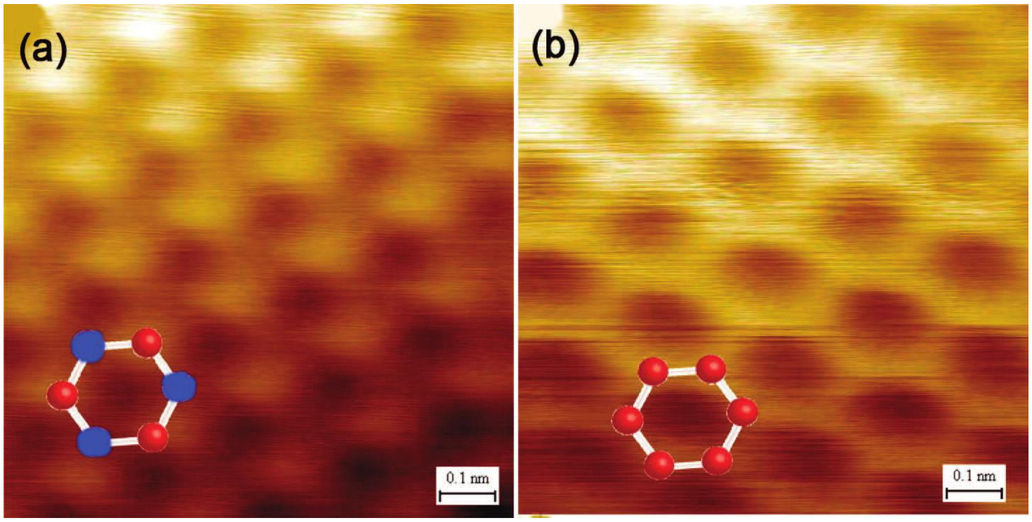

Figure 2-26 (a) STM image of graphite showing only the three carbons that eclipse a neighbor in the sheet directly below. (b) In contrast, all six carbons are equivalent and thus visible in mechanically exfoliated single-layer graphene. Adapted from Ref. [31].

2.6.8 Scanning Probe Microscopy

Scanning probe microscopy was perhaps the most obvious choice for verification of crystallite thickness. The method is relatively slow, but the 0.34 nm (3.4 Å) step height for each successive layer is well within the detection limits of modern atomic force microscopes (AFMs). Resolving the substrate-graphene height profile proved difficult, however, due to the differences in tip attraction/repulsion between the insulating substrate and semi-metallic graphene. This issue was exacerbated under ambient conditions by the preferential adsorption of a thin layer of water on graphene. With such complications, reports of substrate-graphene height profiles by atomic force microscopy have typically ranged from 0.6 to 1.0 nm for single layers [31].

Scanning probe microscopy has a too-low throughput to search for graphene, whereas scanning electron microscopy is unsuitable because of the absence of clear signatures for the number of atomic layers [30].

2.7 Graphene Applications

Graphene as a carbon-based nanomaterial is attractive from the standpoint of science and technology due to its exceptional properties. It is very strong (100 times stronger than steel) [14, 59], highly conductive (charge carrier mobility ~ 200,000 cm^2/Vs that is higher than of copper) [60], has high surface area (2630 m^2/g) [61], highly thermal conductive (~5000 W/mK, means 10 times greater than copper) [62, 63], highly transparent (absorbs only 2.3% of incident light) [57, 58], and flexible.

With the aforementioned unusual properties, graphene open doors for many application disciplines. It is used in electronic applications as transistors [196], chemical and biosensors, transparent conducting electrodes and optoelectronics, and medical applications such as tissue engineering [197] and drug delivery [198]. It is used in energy applications such as solar cells [199], fuel cells[200] and storage fields like supercapacitors [201], hydrogen storage [202] and rechargeable batteries [203]. Its environmental application is mainly in water purification [204].

Water purification is considered as one of the fastest growing and most important applications for graphene due to the massive potential. Defect-free graphene is impervious to almost all small species including He. Graphene stands over a porous substrate and blocks all ions that may pass through, and then selective pores with specific pore size are opened to have what is called a graphene membrane [204].

2.7.1 Graphene Membranes for Water Purification

Demands for fresh water are challenging and increasing nowadays. These demands drive new technologies that increase energy efficiency, minimize feed water pretreatment and decrease plant capital cost.

One promising source of potable water is the world's virtually limitless supply of seawater, but so far desalination technology has been too expensive for widespread use.

Now, researchers are trying to come up with a new approach using a different kind of filtration material: sheets of graphene, a one-atom-thick form of carbon which may be far more efficient and possibly less expensive than existing desalination systems. One common method of desalination, called reverse osmosis, uses membranes to filter the salt from the water. However, these systems require extremely high pressure - and hence, energy use - to force water through the thick membranes, which are about a thousand times thicker than graphene.

Because graphene is the subject of research into many different applications, there has been a great deal of work on finding ways of making it inexpensively and in large quantities. Moreover, for desalination, because graphene is such a strong material - pound for pound, it is the strongest material known - the membranes should be more durable than those presently used for reverse osmosis.

Also, the material needed for desalination does not need to be nearly as pure as for electronic or optical uses, "A few defects don't matter, as long as they don't open up" and allow salt to pass through.

Many methods were found for the production of graphene monolayer. Few of these methods are used for the production of large-scale graphene. The problem in graphene research is always the transfer of the monolayer from production substrates to the application substrates. Many transfer methods have been developed, but still it is challenging in term of defects with respect to graphene layer and large-scale transfer (scalability).

The need for graphene membranes is pressing nowadays. Its impermeability in its pristine (defect free) state, ability to maintain stable sub-nanometer pores and superior mechanical strength make graphene membranes superior in filtration applications. Large area, high-quality graphene on porous structures could be used as a platform on which to create high-efficiency porous graphene membranes

In 2008, Bunch et al. [15], applied a pressure difference across monolayer graphene layer and measured its mass and elastic constants. Graphene showed impermeability to standard gases including helium and it supported pressure differences larger than 1atm. It also showed a stiffness comparable to bulk graphite (E ~ 1 TPa).

In 2009, Li et al. [71], produced a large area graphene by growing over Cu substrate catalyst using the CVD process. The graphene grown was mostly single layer with less than 5% being a few layers. Monolayer graphene not only covered the Cu grains, but it also covered the grain boundaries.

The same year, Jiang et al. [205], used the first principle functional theory to explore graphene permeability and selectivity. Selectivity in the order of 10^8 and 10^{23} for H_2/CH_4 were found for nitrogen-functionalized and all hydrogen passivated pores respectively. They are considered among the first groups suggested for the use of graphene in gas separation.

In 2010, Suk et al. [206], used molecular dynamics simulations to study water transport through a graphene membrane and compared their results with less than 10 nm thickness carbon nanotube membranes. CNT membranes provided higher water flux in the case of smaller diameter pores due to the frequent rupture of the hydrogen bonding network and L/D defect-like water orientation in the graphene pore. The opposite was found in the case of higher diameter pores as a result of the more bulk-like water neighbors and the reduced permeation energy barrier at the entrance.

The same year, Garaj et al. [207], produced a graphene trans-electrode membrane for chemical sensing (DNA molecules). They transferred graphene over a 200*200nm aperture in a SiN layer on a Si chip. Once immersed in the ionic solution, the trans-electrode membrane showed remarkable ionic insulation with small and stable conductance. They claimed to have demonstrated the first realization of DNA translocation using graphene membranes. Merchant et al. [208], developed a graphene device capable of probing DNA molecules. The device has a 1-5 nm thickness and 5-10nm pore size. Results showed that the current blocked by DNA translocation is higher than conventional silicon nitride (SiN) nanopores having the same diameters. The large current noise is reduced by coating the graphene membrane with a thin TiO2 layer; this also provides a more hydrophilic nature that will enable more studies of DNA translocation dynamics through membrane pores.

Schneider et al. [209], developed a graphene device for probing DNA molecules. They transferred mono and multilayer graphene onto a silicon nitride micro-sized membrane (5µm hole) and then opened nano-size pores using a highly focused TEM electron beam.

In 2011, Humplik et al. [10], reviewed the separation mechanisms along with the transport phenomena in nanomaterials including graphene, nanotubes, and zeolites that could be used in different separation methods such as reverse osmosis, capacitive deionization, and multi-stage flash.

In 2012, Cohen-Tanugi and Grossman [8] simulated saltwater flow across free standing graphene using classical molecular dynamics. Separation performance of graphene depends on three factors: namely, the pore size within the graphene, applied pressure, and chemical functionalization. Pore size and chemistry play the critical role; when these pores were functionalized with hydroxyl groups, the water flux was doubled but at the expense of salt rejection. Results showed that water permeability is higher by several orders when compared with the reverse osmosis (RO) process. O'Hern et al. [19] produced a graphene composite membrane by the transfer of monolayer CVD graphene over a polycarbonate substrate. Both pressure-driven and simple osmosis diffusion studies showed the size selectivity of graphene membranes. Results showed that CVD graphene has intrinsic defects (1-10nm) that allow permeation of very small molecular species. The membrane showed considerable selectivity towards the higher molecular species.

Koenig et al. [23] used the ultraviolet-induced oxidative etching process to create pores within graphene membranes. They measured the transport of gases (H_2, Co_2, Ar, N_2, CH_4 and SF_6) through membranes by a pressurized blister test and mechanical resonance. Their results were found to be comparable with theoretical models in the literature based on the diffusion through angstrom-sized pores. Nair et al. [6] developed micrometer-thick GO membranes that were impermeable to liquids, vapors and gases, by spray and spin coating of GO flakes suspended in water. Their membrane was surprisingly permeable to water while blocking other species; they attributed this to the low friction of water flow through two-dimensional capillaries formed by closely spaced graphene sheets.

In 2014, Boutilier et al. [22], independently stacked graphene layers on a porous substrate to understand the gas transport through intrinsic defects and tears within graphene membranes. They developed a model to illustrate how defects and tears leak different types of gases through these membranes. The model showed a minor contribution from such defects on membranes leakage and suggested that the selectivity of graphene membranes can be controlled by controlling the support substrate pore size. O'Hern et al. [20] introduced reactive defects into the graphene by gallium ion bombardment, followed by acidic potassium permanganate ($KMnO_4$) oxidative etching to enlarge those defects. Transport measurements through the graphene showed that the pores were cation-selective at short oxidation times. At long oxidation times, graphene prevented large molecular species but allows salt permeation. Selectivity of graphene is controlled by etching time.

Celebi et al. [18] reported the efficient mass transfer through bi-layer graphene membrane. Free-standing graphene was developed by the transfer of graphene to a SiNx frame punctured with holes having 4µm diameters. The freestanding graphene was then drilled to open up nanopores using a focused ion beam (FIB); pores with (14nm-1um) diameters were achieved by using Ga based FIB and <10nm diameters were achieved using He based FIB. This wide range of pore size allowed them to study the quantitative analysis of mass transport phenomena, such as atmospheric pressure effusion, through atomically thin apertures, Graphene membranes showed distinct effusive, transition, and collective flow regimes to gases, liquids, and water vapor compared with other 2d thin materials.

In 2015, O'Hern et al. [21] successfully sealed defects (intrinsic and larger defects) within graphene membranes. After the transfer of CVD monolayer graphene onto a polycarbonate substrate, nanoscale defects and leaks (~3.5nm) were sealed by atomic layer deposition (ALD) of hafnia (H_fO_2). Larger defects were closed by interfacial polymerization of Nylon 6,6. Diffusion studies showed that the sealed graphene membranes were effectively stopped 92% of potassium chloride ions (KCl).

2.8 Electrospinning Process.

Due to its many advantages and a wide application of its products, electrospinning is considered as the most convenient process for producing micro and nanofibers [210-212].

The process utilizes a very high electric voltage applied to a polymer melt or solution to derive fibers in different morphologies and structures downward to a collected plate or any substrate. Figure 2.27 represents one of the process modes (which could be horizontal, as well as the perpendicular orientation shown), that can be from top to bottom and from bottom to top [212].

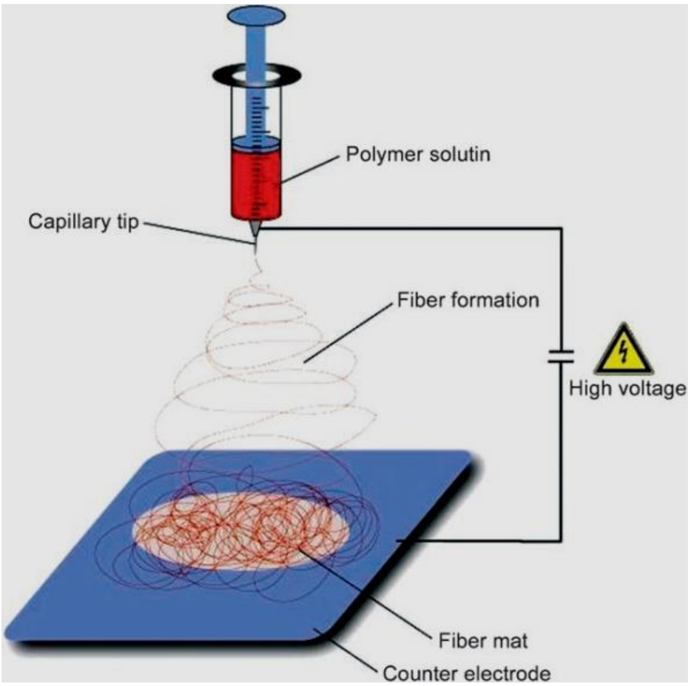

Figure 2-27 Schematic diagram for the simple Electrospinning process with a perpendicular electrode.

As the jet of drawn solution travels from top to bottom, the solvent evaporates during the jet's passage through the zone of instability after which the whipping action of the jet leaves fibers collected over the substrate (counter electrode) [213, 214].

Various types of polymers have been electrospun from a solution and melt form, and been modified/not modified, had some additives incorporated [212]. Metals, metal oxides [215, 216], ceramics, organic/organic, organic/inorganic and inorganic/inorganic composite systems can be electrospun as well [217-224].

As many researchers suggested [225-228], parameters affecting the production of nanofibers using the electrospinning process can be categorized into four major categories, listed in Table 2.5. Upon reviewing the literature, one can find sub-parameters changing from one research group to another, and this depends on their understanding of the process as well as the importance of those parameters from their study perspectives.

Table 2.5 Main parameter categories affecting nanofibers morphology.

1) Polymer Parameters
• Molecular weight.
• Molecular weight distribution
2) Polymeric Solution Parameters
• Concentration.
• Viscosity.
• Surface tension.
• Electrical conductivity.
3) Electrospinning Process Parameters
• Applied voltage.
• The distance between capillary tip and collection screen.
• Flow rate.
• Nozzle orifice diameter.
4) Ambient Condition Parameters
• Temperature.
• Humidity.

CHAPTER 3

MATERIALS AND EXPERIMENTAL PROCEDURE

This chapter gives details of the materials used and the experimental procedures that followed during this work. Most of the materials were purchased from different international suppliers, and few of them were purchased locally. Materials are mainly the CVD graphene, polymeric substrates, and chemicals. The experimental procedure mainly focuses on the different transfer methods used to transfer graphene to the target substrates. Some other experiments were done to check the integrity of graphene layers, such as the ionic transport study and the interfacial polymerization process that is used to seal defects within a graphene layer. A description of the characterization procedure was also highlighted, such as SEM, FESEM, AFM, Contact Angle measurements, Raman spectroscopy and Florescent microscopy examination.

3.1 Materials

Materials used in this study are grouped into (1) the CVD graphene sheets (mono, bi and multiple- layer), (2) the commercial micro/ultra-filtration polymeric substrates and (3) chemicals used in preparation and testing of graphene/polymer composite membranes.

3.1.1 CVD Graphene on Copper Substrate

Monolayer and bilayer graphene grown on a copper (Cu) substrate (25μm thickness thick Cu foil) using a low-pressure CVD process were commercially purchased from ACS Material Company, USA. Graphene was grown onto both sides of the copper foil. Multilayer graphene was prepared in collaboration with Dr. Ahmed Ibrahim at KFUPM, Saudi Arabia (KSA) under the conditions shown in Table 3.1. The CVD process used to produce multi-layer graphene was an atmospheric one.

Table 3.1 Multilayer graphene CVD process parameters.

Substrate	**Temperature /°C**	**Gas reaction mixtures (precursors)**	**Growth time**	**Special conditions**
Copper, 35 μm with 99.9% purity	1000, cooling rate ~18 °C min^{-1}	$CH_4 : H_2$ at 2.5: 97.5	3 min	Annealing time 30 min

3.1.2 Polymeric Substrates

Table 3.2 lists the commercial membranes (substrates) used in this study. We purchased Polypropylene (PP) from Sterlitech Co., USA. Polyvinylidene difluoride (PVDF(1) to PVDF(5)) substrates with two different pore sizes (10, 20 mm) and Polyethersulfone (PES) membranes (substrates) were procured from Novamem Advance Separations Company, Switzerland. PVDF (6) with 100nm pore size was purchased from Millipore Co., USA. Although PVDF substrates (1), (2), (3) and (4) listed in the Table have the same pore size (10nm), according to the manufacturer, they have different pore structures and surface wettability.

Table 3.2 Polymeric substrates characteristics.

No.	Substrate	Pore size (nm)	Thickness (µm)	Surface wetting	pH range
1	PP[1]	100	75-110	Hydrophobic	1-14
2	PES[2]	20	20	Hydrophobic	2-12
3	PVDF(1) [2]	10	50	Hydrophobic	0-12
4	PVDF(2) [2]	10	50	Hydrophobic	0-12
5	PVDF(3) [2]	10	50	Hydrophobic	0-12
6	PVDF(4) [2]	10	50	Hydrophobic	0-12
7	PVDF(5) [2]	20	25	Hydrophobic	0-12
8	PVDF(6) [3]	100	125	Hydrophobic	N/A

1 Supplied from Sterlitech Co. (http://www.sterlitech.com/).

2 Supplied from Novamem Co. (http://www.novamem.com/).

3 Supplied from Millipore Co. (http: //www. merckmillipore.com/).

3.1.3 Chemical Materials & Compounds

Polysulfone (M_w =35,000g/mol) was purchased from BOC Sciences, and the solvent N,N-Dimethylformamide (DMF) (density= 0.944g/cm^3) was purchased from Alfa Aesar. The copper etchant was prepared by mixing 5% (wt/vol) of Ammonium persulphate (Eurostar Scientific LTD) with De-ionized water. Potassium chloride (KCl) and Hexane was purchased from Merck group chemicals, Germany. Hexamethylenediamine was supplied by Fluka Chemicals, Adipoyl chloride from Sigma-Aldrich and finally Texas red®-X, Succinimidyl Ester, a mixed isomers dye from Life Technologies Company, USA.

3.2 Experimental Procedure

3.2.1 Electrospinning of Polysulfone (PSU) Nanofibers

Polysulfone (PSU) pellets were dissolved in N, N-Dimethylformamide (DMF) at 45^{o}C using a magnetic stirrer until uniform and a homogenous solution was obtained. Table 3.3 shows the wt/vol concentration ratios used in this investigation.

Table 3.3 (wt/vol) % concentrations of PSU in DMF

No.	Weight of PSU in (g)	Volume of DMF in (ml)
1	17	100
2	22	100
3	25	100
4	27	100
5	30	100

Electrospinning was carried out using a NANON A-1 apparatus (MECC Ltd., Japan), that operates up to 30 kV voltage and has a 150 mm distance between nozzle and collector. The process started by preparing the syringe (5ml) with a specific amount of solution, fixing it inside the chamber and adjusting the other process parameters such as (the voltage to be applied, distance and feed rate, etc). The tip used for electrospinning had a 0.8mm inner diameter, and aluminum foil was used as a collector. The electrospinning apparatus controlled the feed rate and voltage and it could be adjusted automatically. See Figure 3-1.

PSU nanofiber mats produced were characterized by checking their morphologies and average fiber diameters. Morphology was observed by SEM at different magnifications (1000X, 5000X, and 10000X). Average nanofiber diameters were measured from high magnification SEM micrographs using ImageJ software (http://rsb.info.nih.gov/ij/), in which averages were taken for around 250 readings of every mat, and their standard deviations, minima and maxima were calculated.

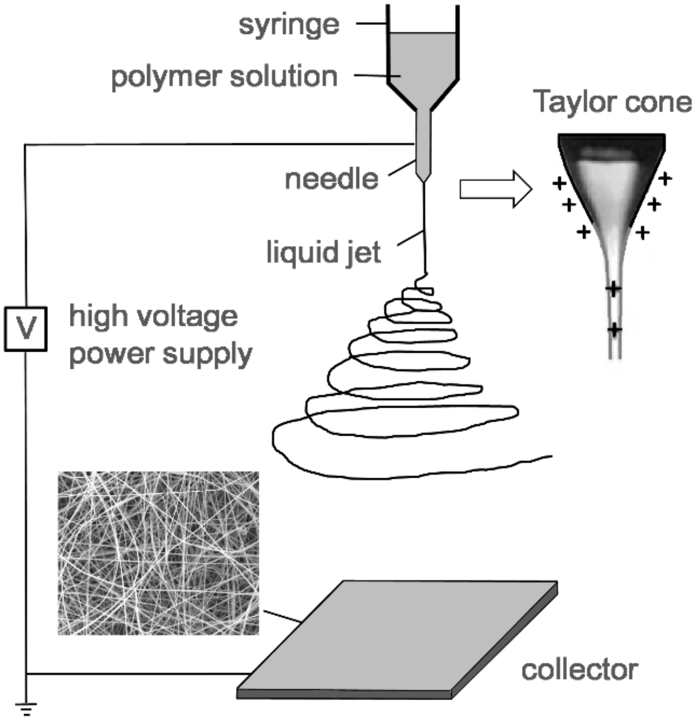

Figure 3-1 Schematic Diagram for electrospinning setup.

3.2.2 Graphene Transfer onto PSU Electrospun Nanofibers

The direct transfer process was developed to transfer graphene onto PSU nanofibers. As received CVD monolayer graphene (Figure 3.2-a) was cut into small pieces (2 cm X 2 cm) and floated over an APS Copper etchant for 5 minutes to remove one side of the graphene (which is, in fact, deposited on both sides of the Cu foil during the graphene CVD production process) as shown in Figure 3.2-b. The CVD Cu/graphene was then placed over the electrospinning collection table (collector) with the graphene facing upward, as shown in Figure 3.2-c. PSU nanofibers were then electrospun over a Cu/graphene coupon under optimized conditions (PSU concentration = 25% (wt/vol), voltage = 20 kV, feed rate = 1.5 mL/min, distance between needle and collector = 150 mm and needle diameter = 0.8 mm). PSU nanofibers were allowed to be deposited over graphene for 30 minutes to form a thick layer with a thickness of roughly ~ 200 µm.

The Cu/graphene/PSU mat composite was then floated onto an APS Cu etchant for nearly 2 hrs (Figure 3.2-d). The composite was then washed with de-ionized water to remove any entrapped etchant liquid and then air-dried (Figure 3.2-e&f).

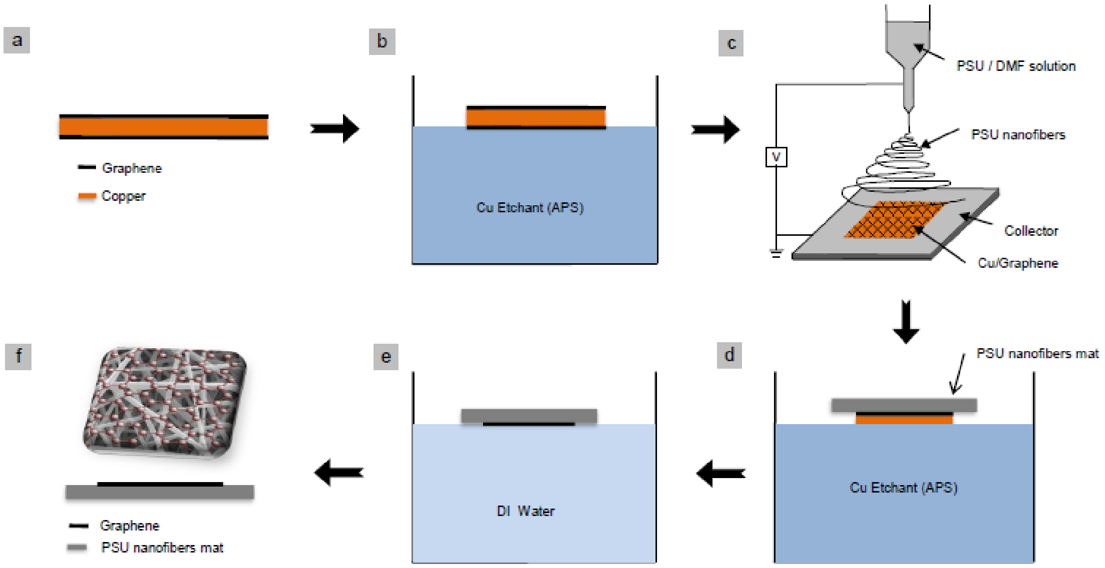

Figure 3-2 Schematic drawing of monolayer graphene transfer onto polysulfone (PSU) nanofiber mat. (a) CVD copper/graphene as received, (b) removal of one side graphene by floating over Cu etchant (APS) for 5 min, (c) electrospun of PSU nanofibers over Cu/graphene to produce Cu/graphene/PSU mat composite, (d) removal of Cu substrate by again floating over APS etchant, (e) rinsing the graphene/PSU mat composite with de-ionized water for 2 min, (f) graphene/PSU mat composite after air drying ready for characterization.

3.2.3 Graphene Transfer onto Polymeric Substrates using Pressing Method

The graphene transfer process onto commercial polymeric membranes was adopted from O’Hern et al. [19], which is a modification of the direct transfer method developed by Regan et al. [162]. The process, as shown in Figure 3.3, begins with the removal of graphene from one side (which is, in fact, deposited on both sides of the Cu foil during graphene production) by floating a 1x1 cm^2 piece (graphene/Cu) over the etchant (APS) for 5-7 minutes. This was followed by dipping in de-ionized water multiple times to remove any entrapped etchant. This step provides a monolayer graphene on one side of Cu foil. The graphene monolayer was attached to the target substrate membrane by sandwiching them with the graphene/Cu between two glass slides and roll pressing with a glass rod (see Figure 3.3-b). A gentle pressing was used to allow conformal graphene attachment to the substrate surface while minimizing damage to the graphene monolayer (see Figure 3.3-c).

The transfer process was then completed by etching away the Cu using the same APS etchant (Figure 3.3-d), leaving behind a well-attached graphene monolayer on the target membrane. The graphene membrane was then passed through two de-ionized water baths for complete removal of the etchant and finally the membrane samples were air-dried, (see Figure 3.3-f).

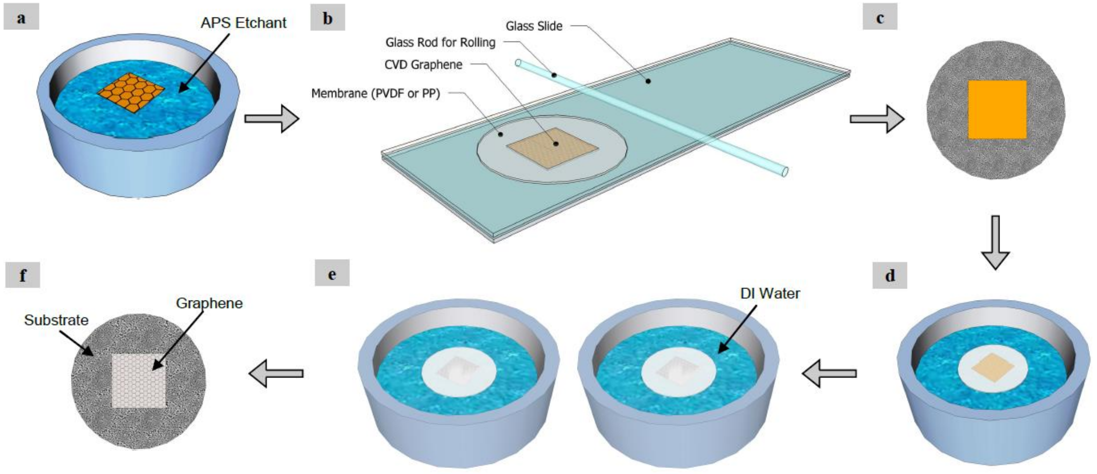

Figure 3-3 Schematic drawing of monolayer graphene transfer onto polymeric substrate, (a) Step (1): removal of graphene from one side of the copper by floating over 5.0% (wt/vol) APS etchant for 5-7 min, (b) Step (2): graphene attachment to target substrate by sandwiching it between two glass slides and gentle rolling of a glass rod, (c) graphene attached to target substrate, (d) Step (3): copper removal by floating copper side over the same APS etchant solution (e) Step (4): washing of transferred graphene by floating on two de-ionized water baths, (f) monolayer graphene on porous polymeric membrane is ready for further study and characterization.

3.2.4 Graphene transfer onto Hydrophilic Polymeric Substrates using Electrostatic Generation.

The copper etchant easily wets hydrophilic substrates. The pressing transfer process is no long applicable for such substrates. Therefore, we developed a new transfer method to transfer graphene onto hydrophilic substrates, and we named it the Electrostatic Transfer Process. The process starts with the removal of one-sided graphene by floating over 5% (wt/vol) APS etchant, as shown in Figure 3.4-a. The Cu/graphene is then attached to the polymeric substrate using an electrostatic generator by exposing the composite to -18kV negative charges with a special electrode, as shown in Figure 3.4-b. The Cu/graphene/substrate is then floated over concentrated APS etchant (25% wt/vol) to etch away the Cu and leaves only graphene attached to the substrate (see Figure 3.4-c). Etching at this concentration is performed and completed in 20 minutes. It is also important at this step to keep the electrostatic electrode on top of the composite during the etching process, as this will help to maintain the contact between the graphene and substrate and prevents etchant solution penetration. The graphene/substrate is then washed by two de-ionized water baths of 10 minutes each and finally air dried.

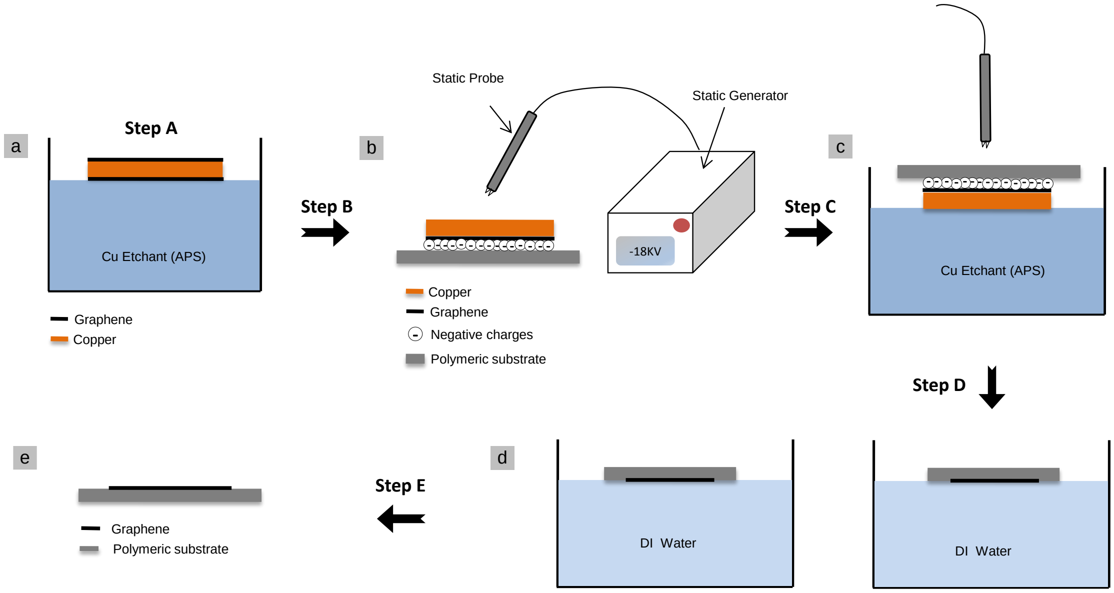

Figure 3-4 Schematic illustration of the electrostatic transfer of graphene onto hydrophilic substrates. (a) Step A: removal of one side graphene by floating over APS etchant for 7 min, (b) Step (2) Attachment of Cu/graphene to the polymeric substrate by discharging of negative charges using static generator working at 18 kV, (c) Step C: chemical etching of Cu substrate by floating over APS Cu etchant for ~ 20 min, continuous electrostatic charging is needed to prevent the etchant penetration between graphene and polymeric substrate, (d) Step D: washing of graphene/polymeric substrate composite with two de-ionized water baths for 10 min each followed by air drying, (e) Step E: the graphene/polymeric substrate ready for characterizations.

3.2.5 Ionic Transport Studies through Graphene Membranes

Ionic transport through the composite graphene-based membrane was studied using a 0.5 M KCl solution. A 7 mL Side-bi-Side glass diffusion cell from Permegear Inc., USA (Figure 3.5) was used for this purpose. The cell is composed of two glass chambers having equal volume and form a 3 mm interfacing orifice when clamped together.

Both cell chambers were cleaned with de-ionized water and air-dried before the composite graphene membrane was placed between them. The active side of the membrane (graphene side) faced the left chamber. The two chambers of the cell were then clamped using a rubber screw and both sides of the membrane were then washed with ethanol to remove any water bubbles close to the membrane surfaces.

To remove any entrapped ethanol from the previous stage, the left cell side was washed with 0.5M KCl solution and the right side with de-gassed de-ionized water three times. A diffusion transport study was performed with 7 mL of 0.5 M KCl solution introduced into the left chamber of the cell, and 7 mL de-ionized was introduced in the right chamber. Both solutions were magnetically stirred using small magnetic stir bars during the diffusion process to minimize concentration polarization effects. Potassium and chloride ions diffused through the graphene membrane toward the de-ionized water side. The diffusion rate of the ions was measured by monitoring the change in conductivity with time, using an eDAQ conductivity isoPod electrode (eDAQ Pty Ltd, USA) dipped in the de-ionized water side of the diffusion cell, as shown in Figure 3.5. Conductivity was recorded every 15 seconds for 10 minutes. The diffusion flux was then calculated from the conductivity data.

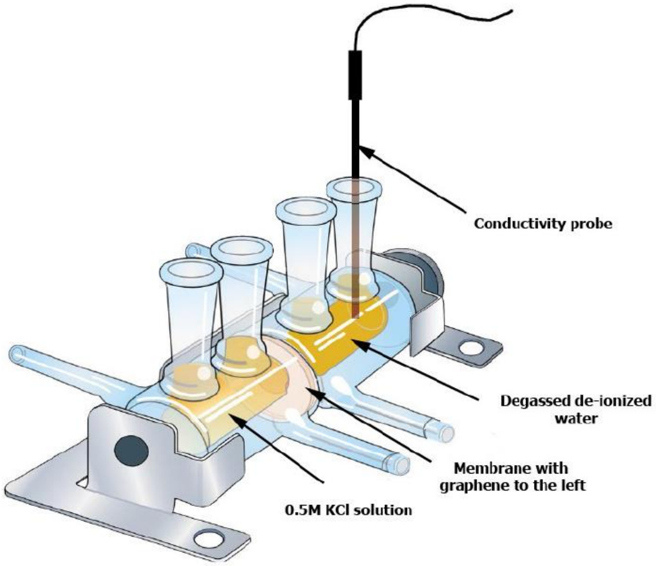

Figure 3-5 Side-bi-side diffusion cell with 7ml volume and 3mm orifice supplied from PermeGear Inc.

3.2.6 Interfacial Polymerization (IP) for Sealing Graphene Defects

As mentioned earlier, the transfer process introduces large tears and cracks in the graphene layer. These tears and cracks need to be plugged and sealed in order to prepare a defect-free graphene composite membrane before introducing pores of controlled size. This defect plugging was achieved via interfacially polymerizing Nylon 6,6 into the defects [21]. A Franz cell (purchased from Permegear Inc., USA) (see Figure 3.6-a) was used to carry out the interfacial polymerization. The cell has two chambers; the upper one was filled with a 27mM Adipoyl chloride (APC) solution in hexane (referred to as solution A), and the lower chamber was filled with 45mM Hexamethylenediamine (HMDA) solution in de-ionized water (referred to as solution B). Solution B was labeled with Texas Red (TR) fluorescent dye, which, after the polymerization process, clearly delineates the presence of Nylon 6,6 zones on the membrane surface. Labeling was performed by reacting Texas red with HDMA in Dimethylformamide (DMF). Firstly, Texas red dissolved in anhydrous DMF at 5 mg/mL; then, HDMA dissolved separately in the DMF at 100 mg/mL. Finally, 7 µL of HDMA/DMF was placed in an eppendorf tube and reacted with 93 µL of TR/DMF very slowly to allow the reaction to occur. The bottom of the cell was first filled with solution B, and the graphene membrane was gently placed over the orifice with the graphene side facing down. The upper chamber was then placed over the membrane and filled with solution A, after which the two chambers were clamped tightly together using stainless steel clamps.

Nylon 6,6 polymerization takes place at the interface when Solution A from the upper chamber travels downwards and penetrates through the graphene defects and meets

Solution B at the other side of the graphene monolayer. Since graphene is impermeable, the only way for the two monomer solutions to meet each other is through the defect sites in graphene (tears and cracks). Thus, interfacial polymerization occurs selectively at defect sites and plugs the defects. At defect sites where graphene is absent, aqueous Solution A will not wick into the hydrophobic membrane, whereas Solution B will wick into the membrane due to capillary action, locating the Solution A / Solution B interface on the graphene side of the membrane. Since the amine is typically more soluble in hexane than the acyl chloride is in water, HMDA diffuses into the organic phase, and the Nylon 6,6 is located inside the membrane, as shown in Figure 3.6-b.

IP was performed for 5 minutes then, the upper part was rinsed with hexane and ethanol five times each to remove any residual APC that may have become entrapped into the membrane. The graphene membrane was removed from the cell and washed with ethanol and de-ionized water to wash away residual HMDA, and finally air dried.

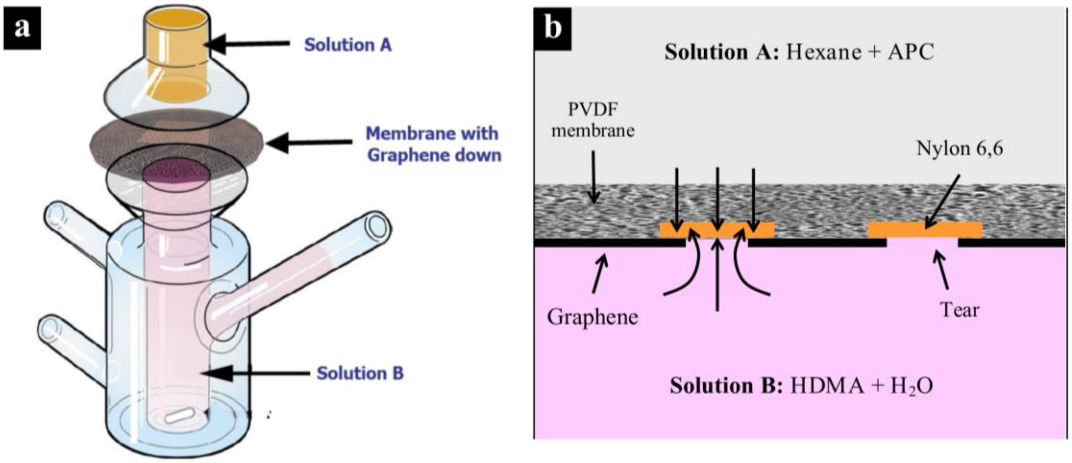

Figure 3-6 (a) 9mm jacketed Franz cell with flat ground joint and 5ml receptor volume, supplied from PermeGear Inc. (b) (a) Schematic drawing explains the synthesis of Nylon 6,6 using IP process.

3.2.7 Static Bacteria Adhesion Test

Several recent researches used a non-pathogenic E. coli strain as a model bacteria to study the membrane's biofouling. The E. coli cells were prepared by incubating and harvesting in Trypton (TT) media at 37° C. The K12 wild-type strain MG 1655 type was grown overnight in a nutrient broth solution and shaken at 160rpm using a rotary shaker. Aliquots of the pre-culture were inoculated into fresh medium and incubated in the same conditions to an absorbance at 600 nm of 0.50 ± 0.025. Cells were harvested by centrifugation at 4000g for 10 minutes at 4° C, washed twice with a sterile 0.9% NaCl solution at 4° C, and re-suspended again in the 100 mL 0.9% NaCl solution to a concentration of 5x10^8 CFU/mL. The bacterial solution was transferred to narrow test tubes. Membrane coupons, with dimensions of approximately 1 cm by 1 cm, were cut from the flat sheets and placed very carefully in 10 mL cell suspension (1 x 10^9 cells/mL) in sterile tubes. The tubes were then placed in a beaker that was kept inside an incubator at a temperature of 37° C for 1 h. The individual tubes were then gently shaken every 15 minutes to ensure complete exposure of the membrane surface to the bacterial suspension. The membrane coupons were then rinsed gently for a few seconds with a bacteria-free broth media to remove weakly bound cells. After exposure to bacteria, the specimens were dried with dry nitrogen for a few minutes. The membrane coupons were then observed under a FESEM, and 6 images were taken across the membrane of surface and the number of bacteria cells per mm surface area was calculated.

3.2.8 Water Permeability Test

A mild brackish water was first prepared by mixing 2000 ppm NaCl in de-ionized water at room temperature. The feed solution was then sucked and pumped (using Eldex Model 1SMP Pulseless pump, USA) through the graphene membranes using the permeation cell shown in Figure 3.7. The pressure was fixed and kept constant using pressure gage that can goes up to 1400 psi (RS Components Ltd, UK). The stainless steel membrane cell (Sterlitech, USA) was the dead end one which has the conventional filtration type with a 5 mm orifice. The permeate was collected after 10 minutes and the volume was measured and the flux was calculated. Permeate salt % was measured using conductivity probe. The water flux and salt rejection were measured at three different pressures (50, 100 and 200 psi) and data were plotted.

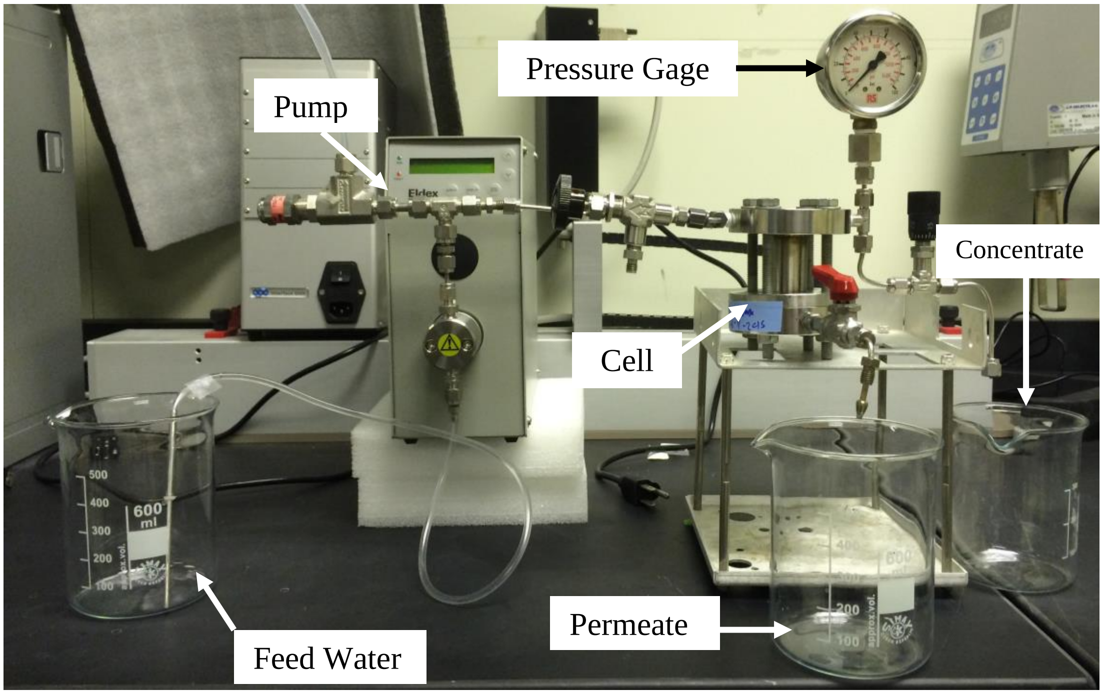

Figure 3-7 Permeation cell used for water flux measurements.

3.3 Characterization Procedures

3.3.1 SEM and FE-SEM Characterization

SEM analysis was carried out using a ***Jeol 4600 instrument***. Substrates were coated with a thin gold layer by a sputtering process; there was no need to coat the graphene membrane since graphene is a conductor. A FE-SEM (***TSCAN-MIRA 3 LM***) was used whenever higher magnification was needed; low voltage (2-5 KV) was used for both microscopes since graphene is conductive. Increasing the working voltage will disturb the images and sometimes distort the spot area.

3.3.2 AFM Characterization

Atomic Force Microscopy (AFM) Examination was performed using a ***Dimension Icon-Bruker instrument***. The working mode was the tapping mode. After cleaning the samples and placing them on the AFM stage, 5 µm X 5 µm (25µm^2) sections were scanned in different places of the samples, and 2d as well as 3d profiles were captured. Three sections were taken to estimate the surface roughness and to calculate the average mean square (RMS value).

3.3.3 Contact Angle Measurement

The wettability of the electrospun polymeric mats was determined using the ***Kyowa-DM 501 contact angle instrument***. De-ionized water was considered for contact angle measurement between the water droplet and the electrospun mat. A half-angle sessile drop method was used for measuring the water contact angle. Static measurements and contact angle image were captured after 100 msec of the droplet being dropped on the surface.

3.3.4 Raman Spectroscopy

Raman spectroscopy, using an ***iHR320 (HORIBA Jobin Yvon Inc)*** was performed using a monochromatic laser beam with 530 nm excitation. Samples were scanned from 1000 cm^{-1} to 3000 cm^{-1} Raman shifts; this range covers all peaks related to graphene and carbon materials.

3.3.5 Fluorescent Microscope Characterization

An upright fluorescent microscope (***Olympus BX61***) was used to highlight the Nylon 6.6 zones within the graphene membrane. The microscope has a fluorescent filter cube turret above the objective lenses, coupled with a digital camera. The light source is a xenon arc type lamp. Samples were labeled with Texas Red fluorescent dye and illumination was done by green and red lighting.

CHAPTER 4

RESULTS AND DISCUSSION

This chapter, in general, discusses the experimental results for the transfer of graphene over a PSU mat and different commercial microfiltration substrates. Section 4.1 summarizes the Raman spectroscopy results of different CVD graphene (mono, bi, and multi-layer graphene), Raman spectroscopy is a good technique to determine not only the existence of graphene but also the number of graphene layers. Section 4.2 focuses on the preparation of a graphene/polysulfone nanofibers mat composite. Preparation of PSU nanofibers is optimized regarding electrospinning parameters such as the PSU solution concentration, voltage applied, solution feed rate, the distance between needle and collector, and finally the needle diameter. After obtaining the optimized conditions, PSU is electrospun directly over graphene. Section 4.3 details the transfer of monolayer graphene onto different commercial microfiltration membranes (substrates). The effect of substrates' surface characteristics on graphene transferability such as the surface roughness and wettability are discussed. Successfully transferred graphene/substrates composites are then characterized by FESEM and KCl ionic transport measurement through them. The section also introduces a method for sealing defects (cracks and tears) introduced within the graphene layer during the transfer, known as Interfacial Polymerization (IP) of Nylon 6,6. New graphene procedures developed to transfer hydrophilic substrates are also discussed in Section 4.3. Bi-layer and multi-layer graphene transfer to the polypropylene (PP) substrate are highlighted in Section 4.4 and 4.5 respectively. Finally, Section 4.6 addresses the antifouling nature of graphene after being transferred onto a PP substrate.

4.1 Raman Spectroscopy for Mono, Bi and Multilayer Graphene

Raman spectroscopy was performed on the purchased CVD mono and bilayer graphene as well as on the prepared multi-layer one (within KFUPM). Raman was also performed on pure Cu to determine if there were any peaks within the scanning shift range of graphene. The most two important features of the Raman graphene fingerprint are the G peak at ~1580 cm^{-1} shift and the 2D peak at ~2670 cm^{-1} [31, 229]. The other peaks shown in Figure 4.1 are result of the background (copper) that can be clearly seen on the copper Raman spectrum. For monolayer graphene, the 2D peak is a single one, with an intensity (I_{2D}) roughly 3-4 times that of the G peak (I_G). The intensity (I_G) of the G peak increases almost linearly as the graphene thickness increases [230]. Since the 2D peak is almost three times the G peak ($I_{2D}/ I_G =3$) as measured from Figure 4.1, the purchased CVD product has monolayer graphene.

Figure 4.2 shows the Raman spectrum of bi-layer graphene. Compared to mono-layer spectrum, I_{2D}/ I_G is approximately less than two ($I_{2D}/ I_G < 2$) which suggest that bi-layer graphene one.

Figure 4.3 shows the Raman spectrum of multilayer graphene prepared at the KFUPM labs. Compared to the monolayer spectrum, as well as the bilayer graphene, the multilayer graphene's I_{2D}/ I_G is approximately less than one ($I_{2D}/ I_G <1$).

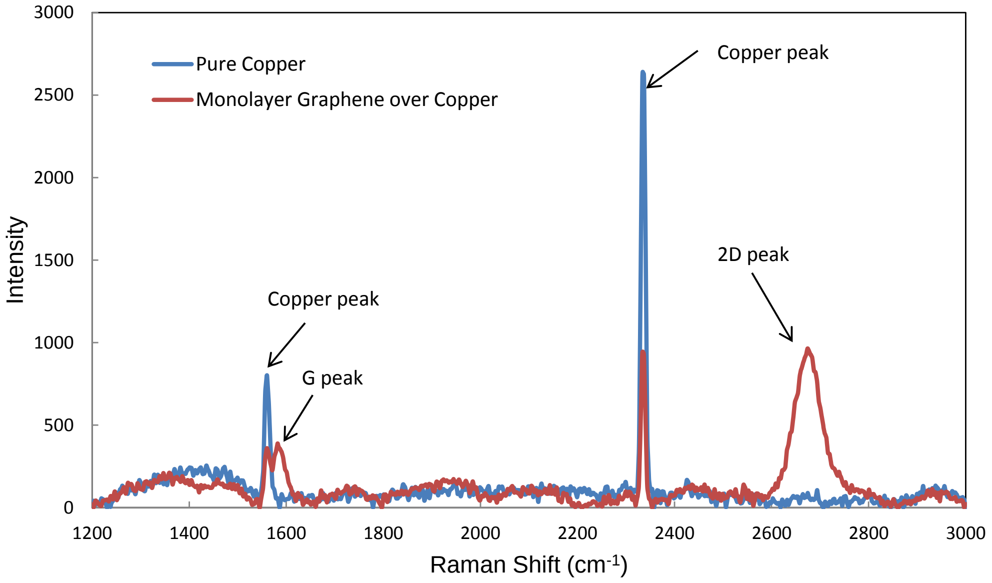

Figure 4-1 Raman spectroscopy for the received monolayer graphene grown onto copper using low-pressure CVD process and for pure copper.

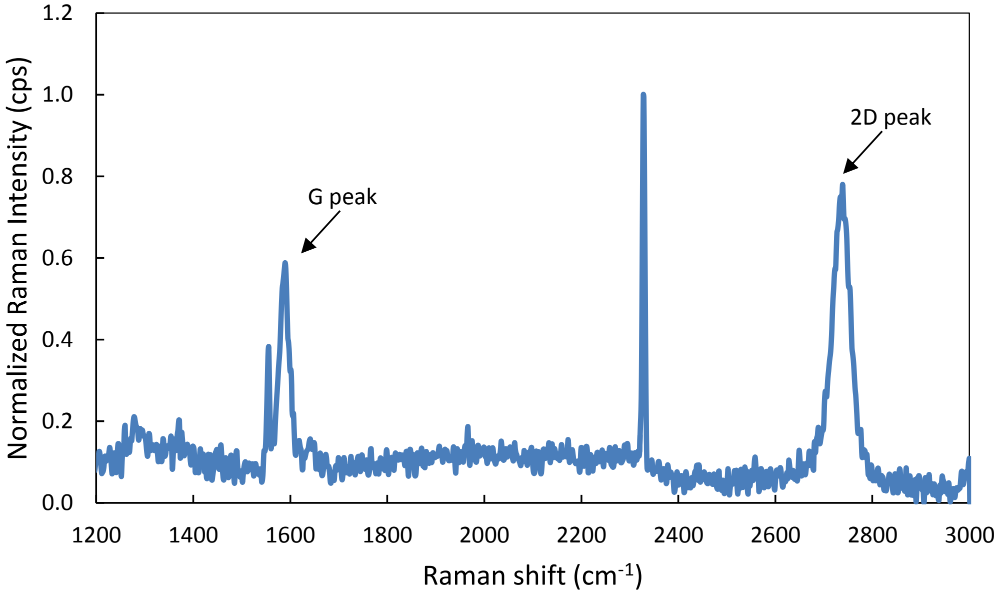

Figure 4-2 Raman spectroscopy for the received bi-layer graphene grown onto copper using low-pressure CVD process.

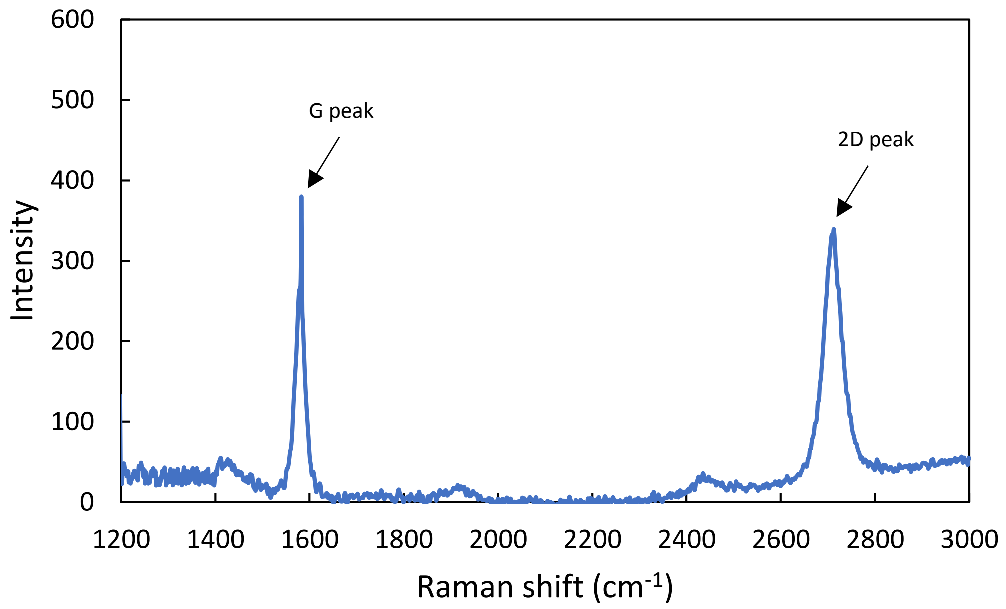

Figure 4-3 Raman spectroscopy for the received multi-layer graphene grown onto copper using atmospheric pressure CVD process.

4.2 Preparation of Monolayer Graphene-polysulfone (PSU) Nanofibrous Membranes

The idea is to produce graphene/PSU electrospun nanofibers membrane that can be used in air separation as well as water purification applications. The electrospinning of PSU nanofibers was first optimized by controlling the PSU concentration, the applied voltage, the solution feed rate, the distance between the nozzle and the collecting plate. The optimized conditions were then fixed, and PSU nanofibers were electrospun over a CVD monolayer graphene. The graphene/PSU mat was then characterized.

4.2.1 Preparation and Characterization of PSU Nanofibers

Table 4.1 shows the electrospinning parameters which were studied on the left-side, and extracted data such as average fiber diameters, standard deviation, minima and maxima on the right side. PSU concentrations of 17%, 22%, 25%, 27% and 30%

(wt/vol) *(Samples PSU 1 to PSU 5)* were studied keeping the voltage at 20 kV, the feed rate at 4 ml/hr and the distance between the nozzle to the collector at 150 mm. The PSU concentration was then fixed at 25% (wt/vol) for reasons to be discussed in section 3.1. Voltages from 20 kV to 30 kV, with 2 kV increments (samples PSU 6 to PSU 11) were tested, keeping the feed rate at 4 ml/hr and the distance at 150 mm. Feed rates of 1 ml/hr, 1.5 ml/hr, 2 ml/hr, 3 ml/hr and 4 ml/hr (samples PSU 17 to PSU 21) were selected after fixing the voltage at 20 kV and the distance at 150 mm. Finally, the effect of distance between the nozzle to the collector was studied by adopting 60 mm, 80 mm, 100 mm, 120 mm and 150 mm distances (samples PSU 12 to PSU 16) keeping the voltage at 20 kV and the feed rate at 4 ml/hr.

Table 4.1 Matrix of electrospun samples with a variation of different parameters along with some extracted data. Noted that: PSU 3, 6, 16 and 21 are with same results.

Polysulfone (PSU) in DMF Samples					**SEM Extracted Data**			
Sample	Concentration (wt/vol)	Voltage (kV)	Distance (mm)	Feed Rate (ml/hr)	Ave. Fiber Diameters (nm)	Standard Div.	Min (nm)	Max (nm)
PSU 1	17.00	20.00	150.00	4.00	Fibers with droplets and beads			
PSU 2	22.00	20.00	150.00	4.00	Beaded Fibers			
PSU 3	25.00	20.00	150.00	4.00	1054.3	395.8	280.6	3024.5
PSU 4	27.00	20.00	150.00	4.00	1448.6	379.7	785.6	2804.7
PSU 5	30.00	20.00	150.00	4.00	2096.9	902.3	935.6	5252.9
PSU 6	25.00	20.00	150.00	4.00	1054.3	395.8	280.6	3024.5
PSU 7	25.00	22.00	150.00	4.00	1068.9	388.1	198.2	2255.0
PSU 8	25.00	24.00	150.00	4.00	1147.2	404.8	413.2	2684.6
PSU 9	25.00	26.00	150.00	4.00	1239.3	404.3	327.2	2858.4
PSU 10	25.00	28.00	150.00	4.00	1274.8	450.1	317.0	2924.2
PSU 11	25.00	30.00	150.00	4.00	1314.1	407.1	662.1	2206.7
PSU 12	25.00	20.00	60.00	4.00	1199.4	445.6	405.2	3116.0
PSU 13	25.00	20.00	80.00	4.00	1264.0	477.0	286.0	2806.0
PSU 14	25.00	20.00	100.00	4.00	1184.0	473.0	327.0	3269.0
PSU 15	25.00	20.00	120.00	4.00	1158.7	376.1	577.8	2589.4
PSU 16	25.00	20.00	150.00	4.00	1054.3	395.8	280.6	3024.5
PSU 17	25.00	20.00	150.00	1.00	609.0	219.0	177.0	1389.0
PSU 18	25.00	20.00	150.00	1.50	699.4	219.1	158.7	1796.6
PSU 19	25.00	20.00	150.00	2.00	750.0	315.3	236.9	1748.1
PSU 20	25.00	20.00	150.00	3.00	952.0	360.0	335.0	2857.0
PSU 21	25.00	20.00	150.00	4.00	1054.3	395.8	280.6	3024.5

Effect of PSU Concentration on fiber morphology

The concentration or the amount of polymer in solution is an important factor in determining fiber morphology [231]. Too high a concentration will hinder the solution from being pumped [232] [233]; on the other hand, too low a concentration will lower the amount of polymer chain entanglements that are required to keep the jet from breaking down [234].

At the concentration of 17% (wt/vol), there was insufficient polymer entanglement to stabilize the jet and as a result, many droplets and beads formed, as shown Figure 4.4-a. As the concentration increased to 22% (wt/vol), the jet was stabilized but many beads still appeared in the nanofiber morphology (Figure 4.4-b). This may have been due to the high solution surface tension, which, at this concentration, will have more of a controlling effect than the electric force (which is responsible for stretching fibers) [226]. Yuan et al. [225] suggested that the lower viscosity and conductivity of the lower concentration PSU solutions could be the possible reasons which lead to the formation of beaded fiber morphology. These beads began to disappear as the concentration reached 25% (wt/vol) and uniform fibers without beads were obtained (Figure 4.4-c). An increase in the concentration was responsible for increasing the average fiber diameter (Figure 4.4-d and e) and broadness of the fibers (Figure 4.4-f).

Figure 4.4-f shows the relation between average fiber diameters and concentration. As the concentration increases the average fiber diameter increases and becomes broader. The plot shows took only three concentrations (25%, 27% and 30% (wt/vol)) and excluded 17% and 22% which did not allow accurate average fiber diameter measurements due to the presence of excesive droplets and beads. Demir et al. [235]

studied the relationship between fiber diameter and solution concentration during polyurethane electrospinning where they reported that the average fiber diameter increased with concentration according to a third power law.

Many researchers have studied the effect of an increase in concentration on the electrospinning process and average fiber diameter [236-245]. They found the same trend in this study, and they added that increasing the concentration will, in some cases, increase fiber length [241], decrease the tendency of bead formation, and cause the fibers to become smoother and more uniform. Fong et al. [236], found that as beads became bigger, the distance between them became larger and changed shape from spherical to spindle-like, with increasing viscosity, before reaching uniformity.

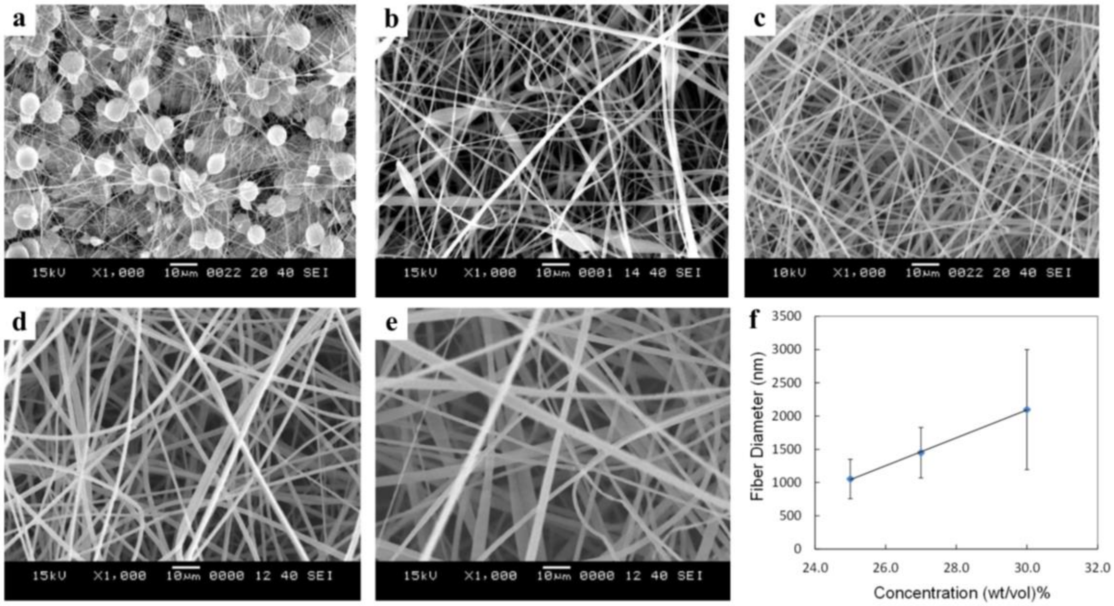

Figure 4-4 Effect of PSU concentration on morphology and diameters of nanofibers, keeping feed rate at 4mL/hr, the voltage at 20kV and distance at 150mm. a) SEM for 17%(wt/vol), b) 22%(wt/vol), c) 25%(wt/vol), d) 27%(wt/vol), e) 30%(wt/vol), f) variation of average fiber diameters with concentration.

Effect of Applied Voltage on fiber morphology

In the literature, applied voltage was found to be the most contradictory parameter affecting nanofiber morphology; the average fiber diameters were found to be either directly [244, 246-252] or inversely [234, 242, 253-260] proportional to the applied voltage, and in some cases, in between [231, 232, 239, 259, 261-263].

Average fiber diameters were found to increase with increasing voltage, as shown in Figure 4.5. The solution concentration used was 25% (which provides uniformity in structure and the lowest fiber diameters), with a 4 ml/hr feed rate and a distance of 150mm between the nozzle and collector. Figure 4.6 shows SEM micrographs for PSU nanofibers with a variation of voltages ranging from 20 kV (Figure 4.6-a) to 30 kV (Figure 4.6-f) with 2 kV increments.

Although increasing the voltage will increase the elongational force that is responsible for fiber thinning, the time for the jet to travel downward will be shortened. As a result, there will be insufficient time for full solvent evaporation. In addition, a higher voltage will cause more mass flow, and all of these factors will favor fiber diameter increase [235, 250].

Some researchers found the presence of beads with increasing voltages [242, 254, 264, 265] and they attributed this to the instability of the jet at the needle, in which the Taylor cone is receding [251]; another other reason is the steep increase in the spinning current [266]. However, in this study, beads at high voltages were not observed.

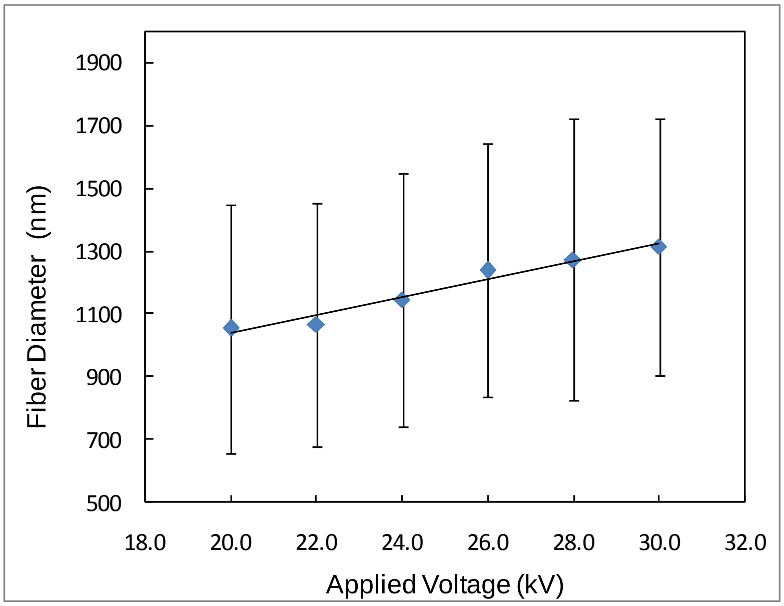

Figure 4-5 Variation of average fiber diameters with applied voltage, keeping feed rate at 4mL/hr and distance at 150mm.

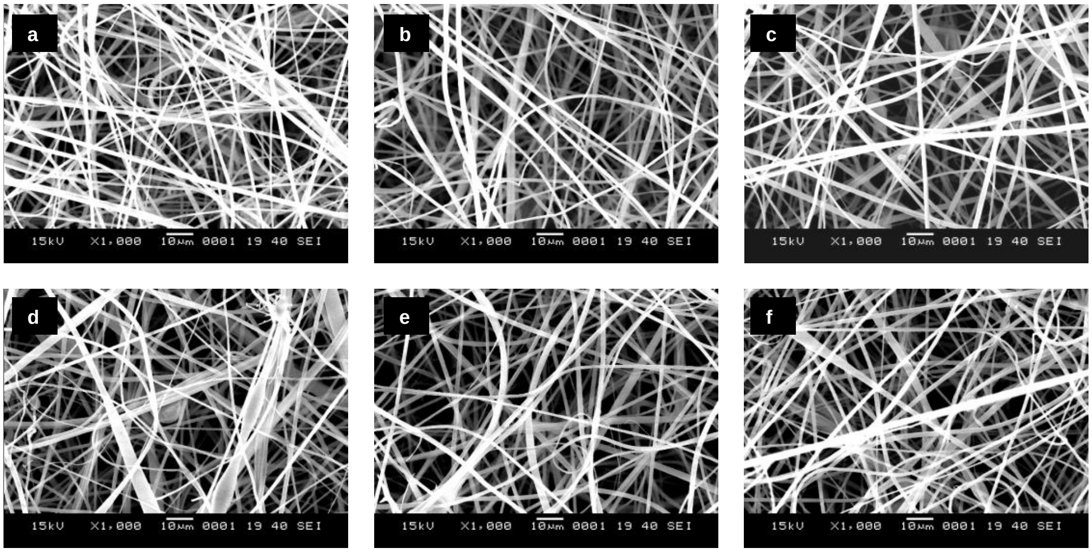

Figure 4-6 Effect of Electrospinning voltage on the morphology and diameters of nanofibers, keeping feed rate at 4mL/hr and distance at 150mm. A) SEM for 20kV, B) 22kV, C) 24kV, D) 26kV, E) 28kV, F) 30kV.

Effect of solution feed rate on fiber morphology

In other words, the feed rate represents the amount of solution to be electrospun [226, 267] and it is very important to control it because it is related to the Taylor cone stabilization. The feed rate in this study was varied from 1 ml/hr to 4 ml/hr, keeping the voltage at 20 kV, distance at 150 mm and 25% (wt/vol) concentration, as seen in Table 4.1.

Average fiber diameters were found to increase with and increasing feed rate (Figure 4.7-f), and many research groups proved this, [226, 234, 239, 268-270]. They attributed this trend to the smaller time needed for the jet to reach the collector, resulting in a lower solvent evaporation rate that leaves thicker fibers.

At lower feed rates (1 ml/hr), as shown in Figure 4.7-a, some beads (red marks) were noticed and started to disappear with an increasing feed rate (Figure 4.7-e). This is because the low amount of polymer coming out of the needle with high voltage will make the jet unstable and discontinuous; this will increase the surface tension and favor the formation of beads.

It was also noticed (Figure 4.7-f and Table 4.1) that the broadening of fiber diameters with an increasing feed rate where the standard deviation of readings at 1 ml/hr is almost half that of the 4 ml/hr feed rate could be attributed to the increased time needed for the lower feed rate nanofibers to achieve complete solvent evaporation.

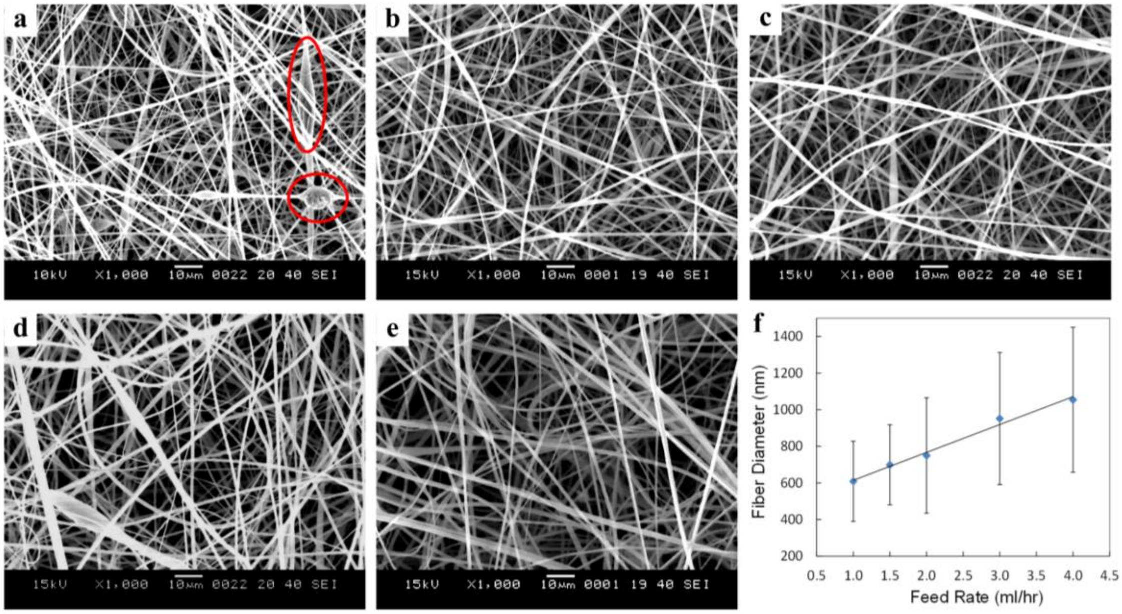

Figure 4-7 Effect of solution feed rate on the morphology and diameters of nanofibers, keeping the voltage at 20kV and Distance at 150mm. a) SEM for 1ml/hr, b) 1.5ml/hr, c) 2ml/hr, d) 3ml/hr, e) 4ml/hr, f) Variation of average fiber diameters with feed rate.

Effect of distance between nozzle and collector on fiber morphology

The distance between the nozzle and collector influences two important parameters related to fiber morphology. The first is the jet traveling time, in conjunction with the solvent evaporation rate, and the second is the field strength, which is defined as the voltage over distance [234, 266].

Decreasing this distance will shorten the time for the jet to travel, and increases the field strength that will result in higher fiber diameters [239, 252, 271, 272]. Figure 4.8a-e shows SEM micrographs for 25% (wt/vol) PSU nanofibers electrospun at 20 kV voltage, 4 ml/hr feed rate and different distances, varied from 60 mm to 150 mm. When changing the distance a slight decrease in average fiber diameteris noticed; fiber diameters at a distance of 60 mm were measured to be 1199.4 ± 445.6 nm, whereas at a distance of 150 mm, the diameters were decreased to 1054.3 ± 395.8 nm.

This slight decrease in fiber diameter could be attributed, as mentioned above, to the extra time needed for solvent evaporation, which causes fiber thinning from one side, and to the lower field strength, which result in a lower stretching force from the other side. Unlike some results found in the literature [242, 243, 257], the distance between the nozzle and collector was not found to relate to the appearance of beads which could be related to the polymer and solution properties. **Megelski et al**. [243] found that the average fiber diameter does not change significantly with distance, and their observations are consistent with the findings of this study. However, on the other hand, they found some elongated beads along polystyrene (PS) fibers.

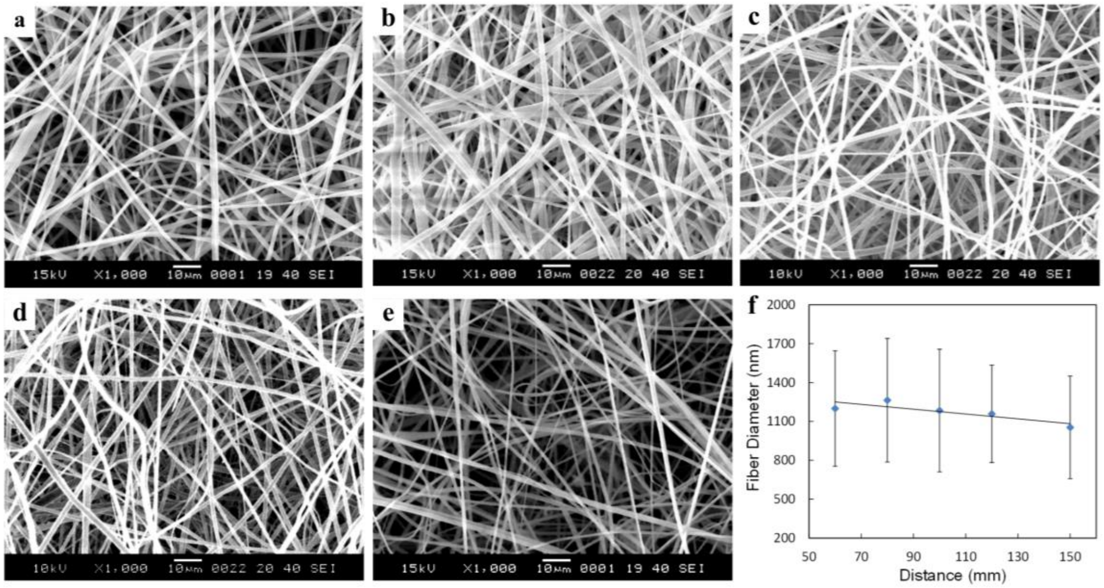

Figure 4-8 Effect of distance between nozzle and collector on the morphology and diameters of nanofibers, keeping the voltage at 20kV and feed rate at 4ml/hr. a) SEM for 60mm, b) 80mm, c) 100mm, d) 120mm, e) 150mm, f) Variation of average fiber diameters with a nozzle to collector distance.

In conclusion, the best average fiber diameter (around 700nm) with uniform structure and without beads was found where the concentration is 25% (wt/vol), the applied voltage is 20 kV, with a 1.5 ml/hr feed rate and distance of 150 mm. These parameters are then used to electrospin a PSU nanofiber mat onto CVD monolayer graphene.

4.2.2 Monolayer Graphene Transfer onto PSU Mat

The idea here is to electrospin PSU nanofiber mats directly over monolayer CVD graphene, and then etch the copper using an APS copper etchant as explained in Section 3.2.2. Figure 4.9 shows the experimental transfer procedure of graphene onto the PSU electrospun nanofibers mat. Figure 4.9-a shows the CVD graphene during the electrospinning of PSU nanofibers. The voltage was 25 kV, the feed rate was 1.5 mL/min, the distance from spinneret and collector was 150 mm, and the PSU concentration was 25% (wt/vol), as labeled in Figure 4.9-b. The complete etching of copper lasted for 20 minutes.

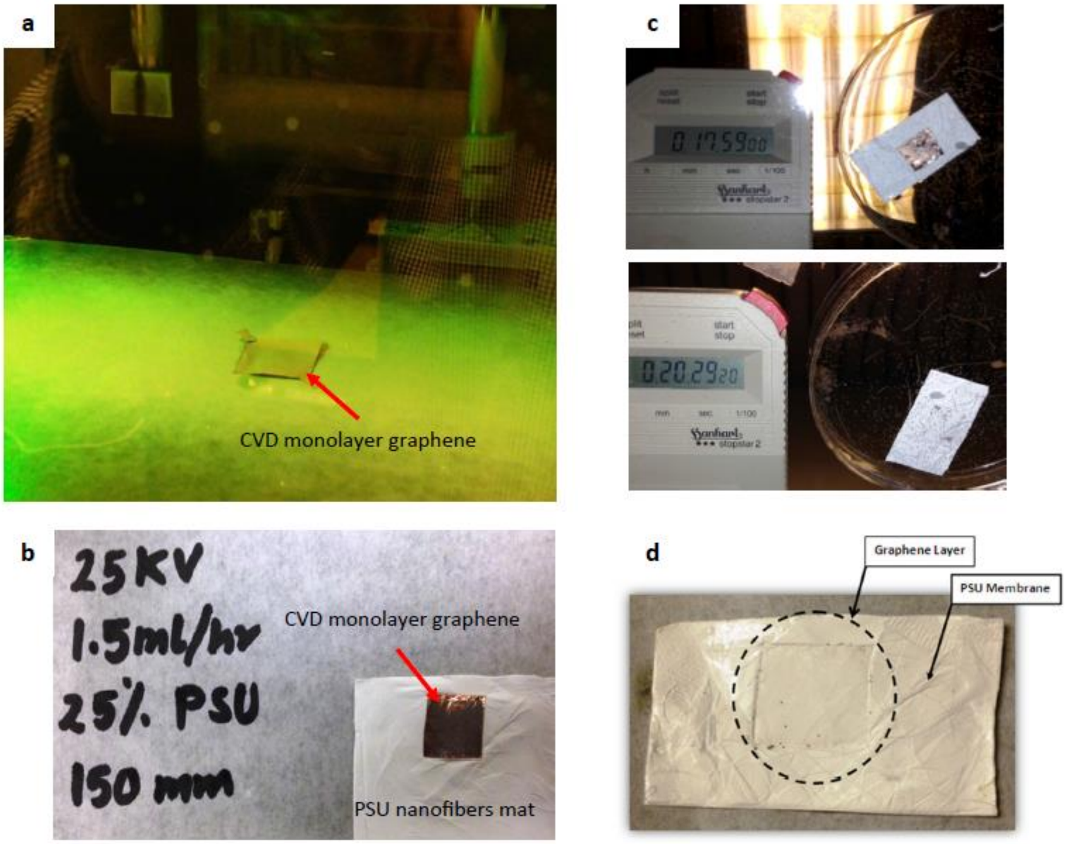

Figure 4-9 (a) Cu/graphene stands over the electrospinning collector plate during electrospinning of PSU nanofibers, (b) the graphene/PSU mat before etching of copper, (c) graphene/PSU mat during the etching process, the copper is completely removed after 20 minutes, (d) the graphene/PSU mat composite ready for further characterization.

The graphene/PSU mat composite was then characterized by Raman spectroscopy, as shown in Figure 4.10. The results show no graphene above the PSU mat, as the Raman shifts for PSU mat with and without graphene are identical. This does not necessarily mean that the graphene is not covering, but it may mean that the graphene has transferred with poor quality (with tears and cracks). SEM characterization was performed to check whether graphene was present or not, and to examine the quality if it was.

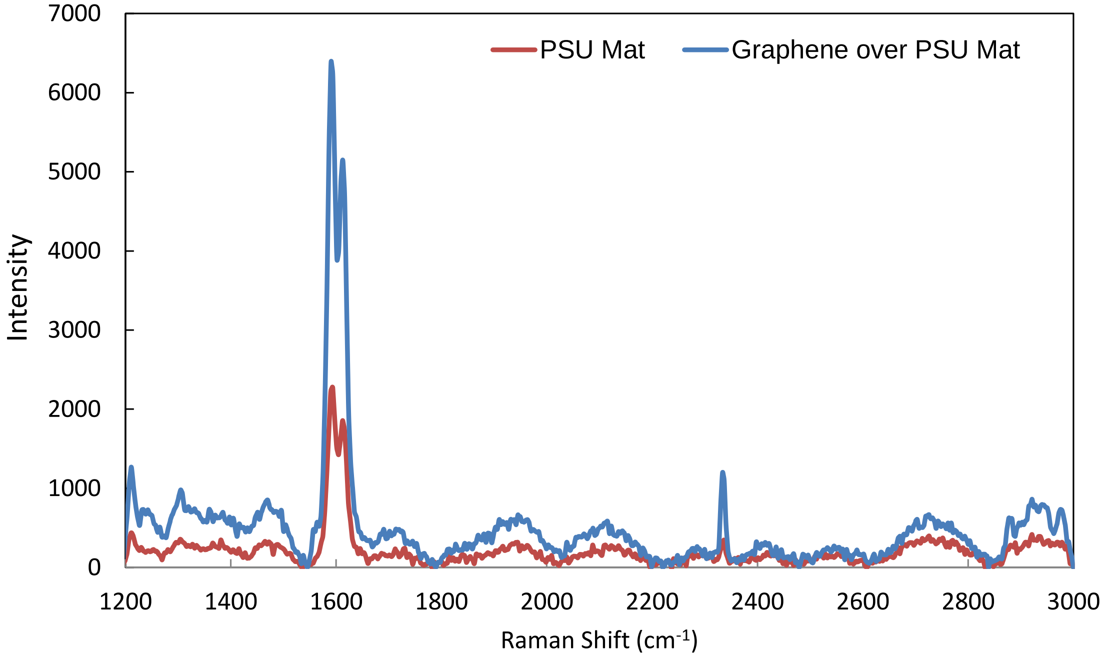

Figure 4-10 Raman shifts of PSU mat and graphene/PSU mat composite.

Figure 4.11 shows clearly that graphene covers the PSU mat but with very poor quality. Graphene was severely torn during the copper etching step, as shown in Figure 4.11-a; less severely torn graphene zones were also noticed, as shown in Figure 4.11-b.

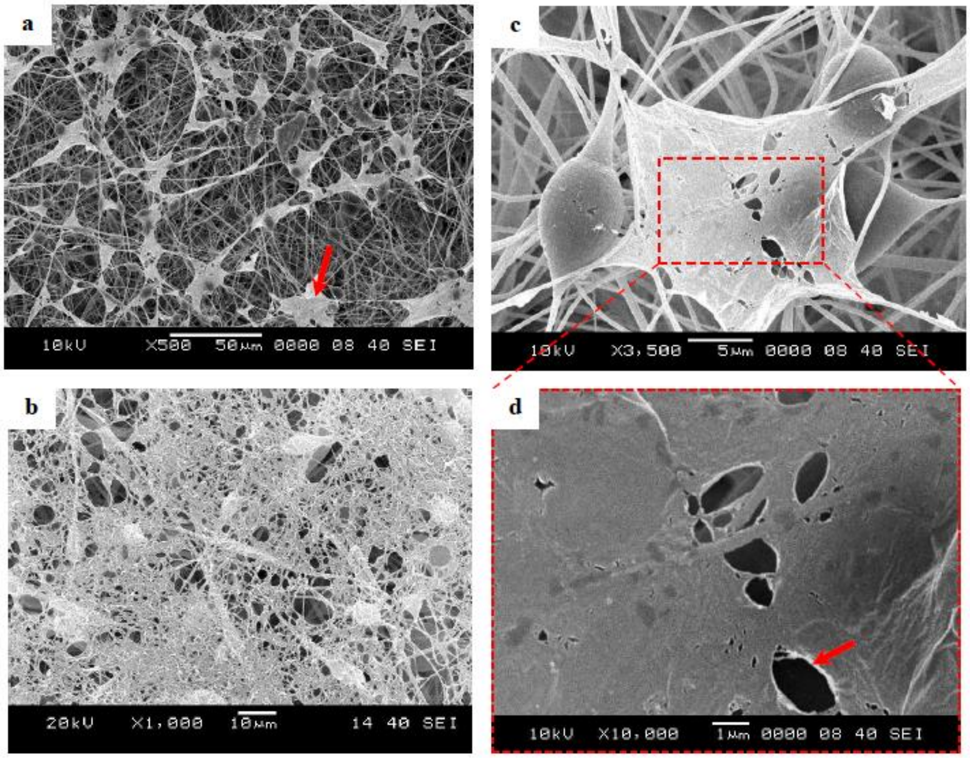

Figure 4-11 SEM of graphene over PSU nanofibers mat, (a) low magnification micrograph shows the electrospun nanofibers and batches of torn graphene as indicated by arrow, (b) higher magnification micrograph shows how graphene tears, (c) graphene area at high magnification, (d) high magnification micrograph shows only graphene and the tears as indicated by arrow.

Bunch et al. [273], reviewed recent experimental and theoretical advances in the understanding of how graphene adheres and conforms to different substrates. Three parameters were found to affect the quality of transferred graphene, namely surface roughness, porosity and wettability (degree of hydrophobicity). The substrate surface should be smooth to have good contact between the graphene and substrate, and the pore size should be as small as possible to minimize the number of suspended graphene domains that may tear during the transfer process. The surface should be of a quite high hydrophobicity to keep the membrane non-wetted by the etchant during etching of the copper in the transfer process. Otherwise, the etchant solution will penetrate between the graphene and substrate and, in this case, the graphene will certainly be detached and lost. In addition, contact must be maintained between the graphene and substrate throughout the etching process [26].

According to the above literature explanation, graphene tore due to the high roughness and large pore size of the PSU mat. Figure 4.12 shows the pore size distribution of the PSU mat. The average pore size was found to be approximately 7µm; that makes the PSU mat rough and large pores fail to provide the needed support to hold the graphene domains during the transfer process. Furthermore, the mobility of nanofibers within the electrospun mat also contribute to the tearing the graphene layer.

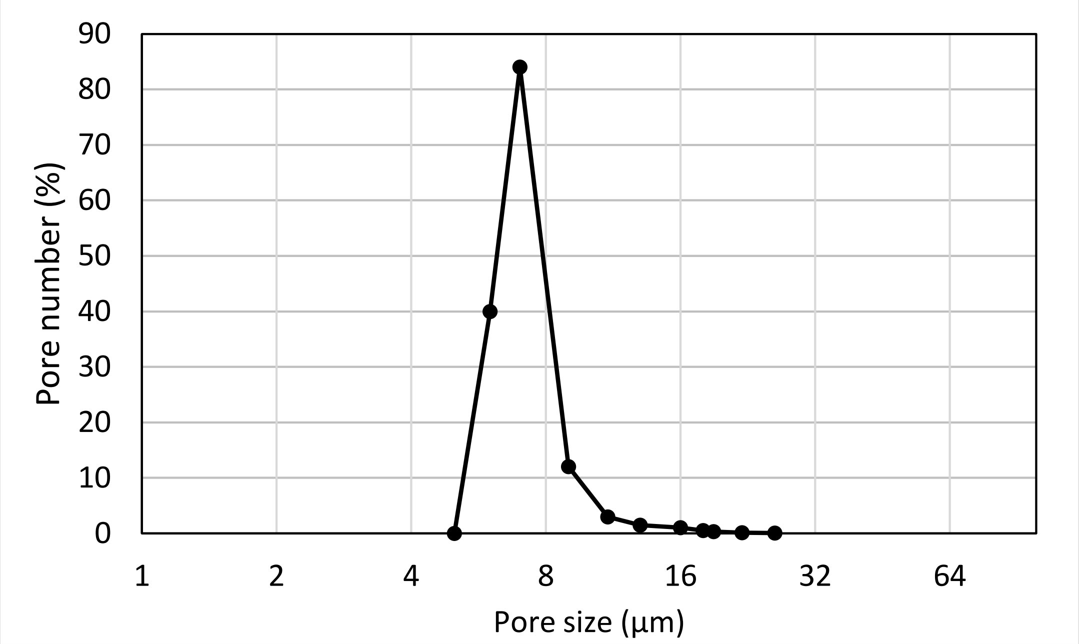

Figure 4-12 Deferential pore number of PSU mat, average pore size is approximately 7µm.

It was thus clear that the electrospun nanofibers mats are not the right substrate for graphene transfer and the efforts to proceed with transfer of graphene on electrospun nanofiber mats was abandoned.

4.3 Monolayer Graphene Transfer onto Polymeric Commercial Microfiltration Membranes

In this section the transfer of monolayer graphene onto different commercial microfiltration substrates is reported. The effect of a substrate's surface characteristics on graphene transferability was studied.

4.3.1 Surface Characterization of Polymeric Substrates

Eight different commercial polymeric membrane substrates were purchased from different sources. The selection of the membranes was based on the pore size and the surface wetting characteristics. Table 4.2 provides the list and characteristics of the commercial membranes selected for the study.

Table 4.2 Characteristics of as received polymeric substrates.

No.	Substrate	Pore size (nm)	Thickness (µm)	Surface wetting	pH range
1	PP$^{(1)}$	100	75-110	Hydrophobic	1-14
2	PES$^{(2)}$	20	20	Hydrophobic	2-12
3	PVDF 1$^{(2)}$	10	50	Hydrophobic	0-12
4	PVDF 2$^{(2)}$	10	50	Hydrophobic	0-12
5	PVDF 3$^{(2)}$	10	50	Hydrophobic	0-12
6	PVDF 4$^{(2)}$	10	50	Hydrophobic	0-12
7	PVDF 5$^{(2)}$	20	25	Hydrophobic	0-12
8	PVDF 6$^{(3)}$	100	125	Hydrophobic	N/A

1 Supplied from Sterlitech Co. (http://www.sterlitech.com/).

2 Supplied from Novamem Co. (http://www.novamem.com/).

3 Supplied from Millipore Co. (http://www. merckmillipore.com/).

FESEM, AFM analysis and contact angle measurement were carried out for all substrates to evaluate their surface characteristics.

Figures 4.13 to 4.20 show SEM, AFM micrographs and contact angle measurements for all bare substrates (before graphene transfer). FESEM was used to explore the surface morphology, which was then followed by AFM characterization to check surface roughness. Three sections were taken to explore the surface profile and to calculate the average root mean square (RMS), surface roughness and 3D profiles were also captured to check and confirm surface roughness.

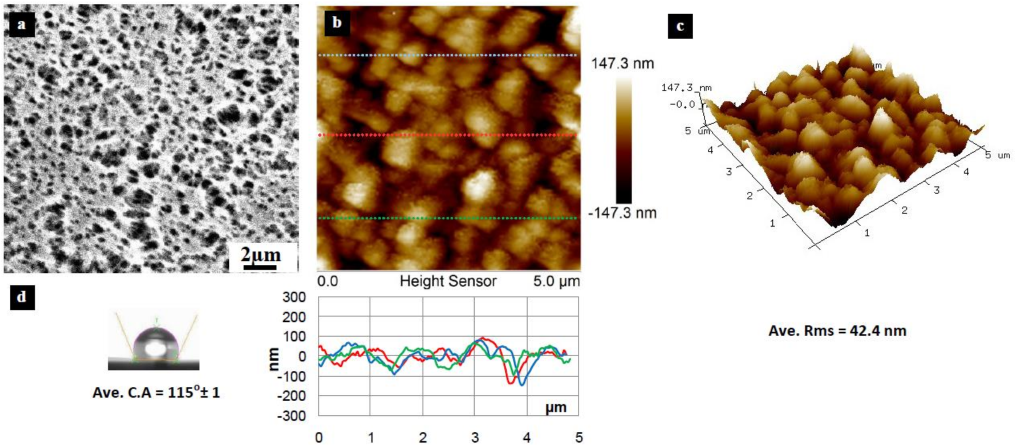

Figure 4-13 Surface characteristics of a received PP substrate (100 nm pore size), (a) SEM micrograph, (b) 5x5 µm^2 AFM image (at top) and three section profiles (at bottom) with an average RMS equal to 42.4 nm (c) 3D profile for the selected area, (d) surface contact angle (CA) with an average equal to 115° ± 1.

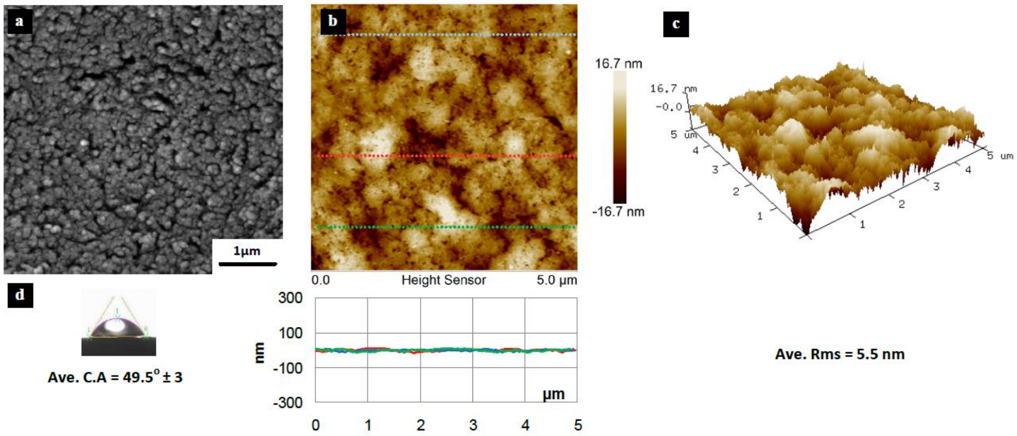

Figure 4-14 Surface characteristics of a received PES substrate (20 nm pore size), (a) SEM micrograph, (b) 5x5 µm^2 AFM image (at top) and three section profiles (at bottom) with an average RMS equal to 5.5 nm (c) 3D profile for the selected area, (d) surface contact angle (CA) with an average equal to 49.5° ± 3.

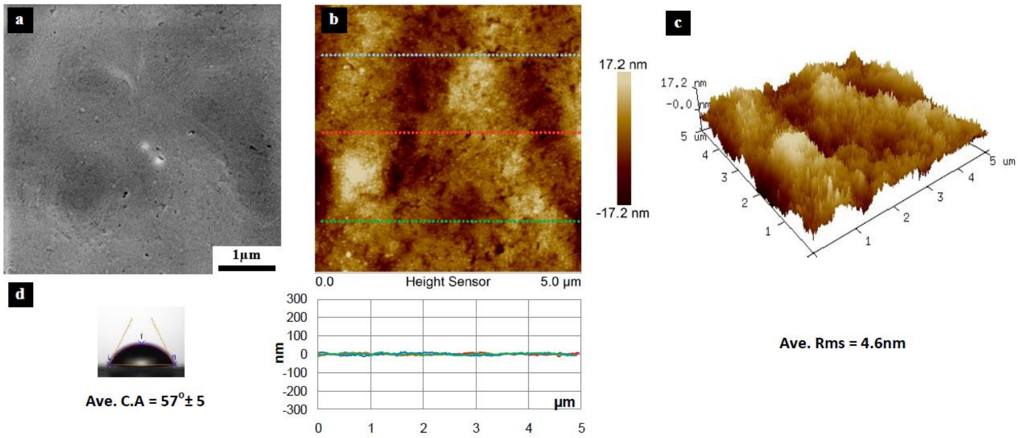

Figure 4-15 Surface characteristics of a received PVDF 1 substrate (10 nm pore size), (a) SEM micrograph, (b) 5x5 µm^2 AFM image (at top) and three section profiles (at bottom) with an average RMS equal to 4.6 nm (c) 3D profile for the selected area, (d) surface contact angle (CA) with an average equal to 57º ± 5.

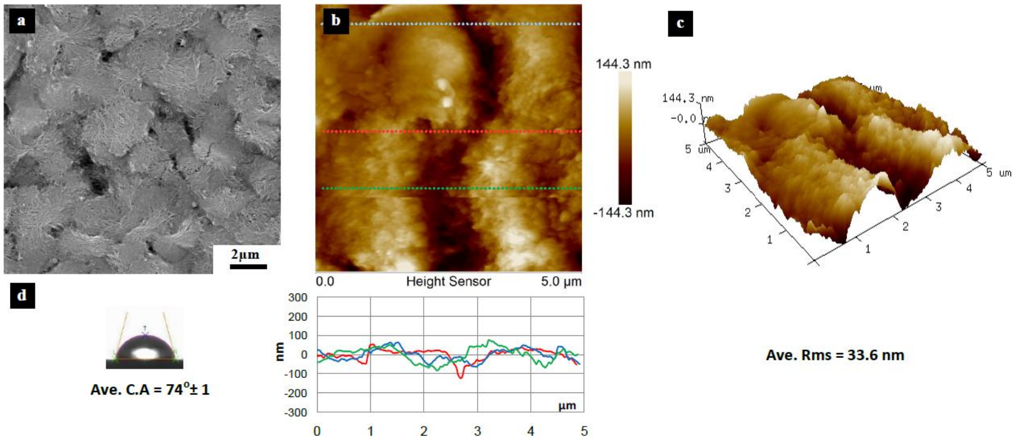

Figure 4-16 Surface characteristics of a received PVDF 2 substrate (10 nm pore size), (a) SEM micrograph, (b) 5x5 µm^2 AFM image (at top) and three section profiles (at bottom) with an average RMS equal to 33.6 nm (c) 3D profile for the selected area, (d) surface contact angle (CA) with an average equal to 74º ± 1.

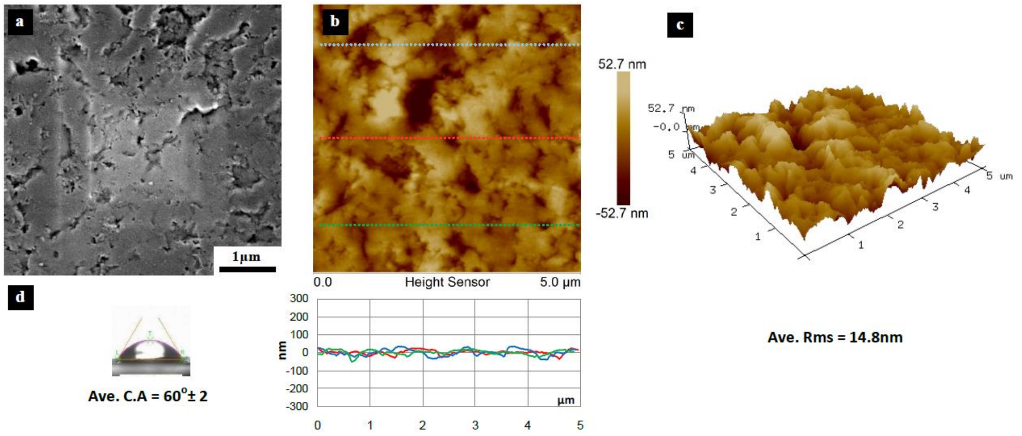

Figure 4-17 Surface characteristics of a received PVDF 3 substrate (10 nm pore size), (a) SEM micrograph, (b) 5x5 µm^2 AFM image (at top) and three section profiles (at bottom) with an average RMS equal to 14.8 nm (c) 3D profile for the selected area, (d) surface contact angle (CA) with an average equal to 60º ± 2.

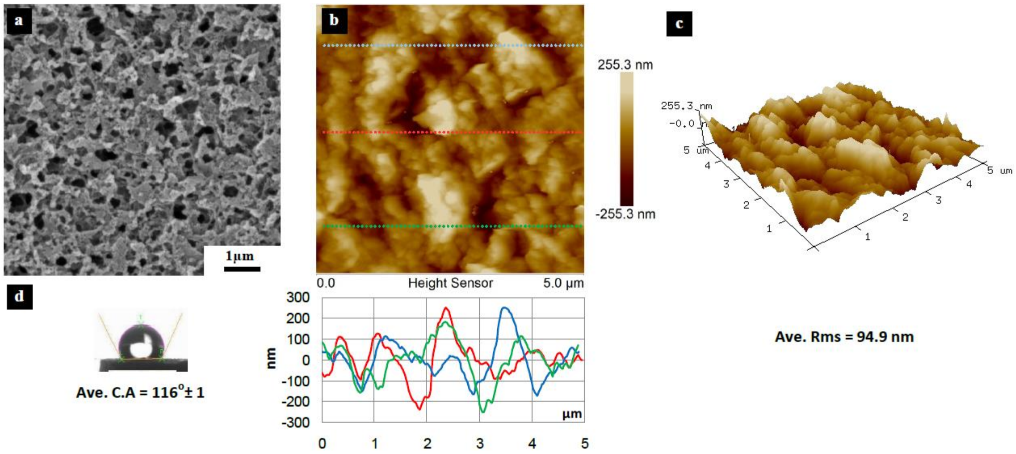

Figure 4-18 Surface characteristics of a received PVDF 4 substrate (10 nm pore size), (a) SEM micrograph, (b) 5x5 μm^2 AFM image (at top) and three section profiles (at bottom) with an average RMS equal to 94.9 nm (c) 3D profile for the selected area, (d) surface contact angle (CA) with an average equal to 116° ± 1.

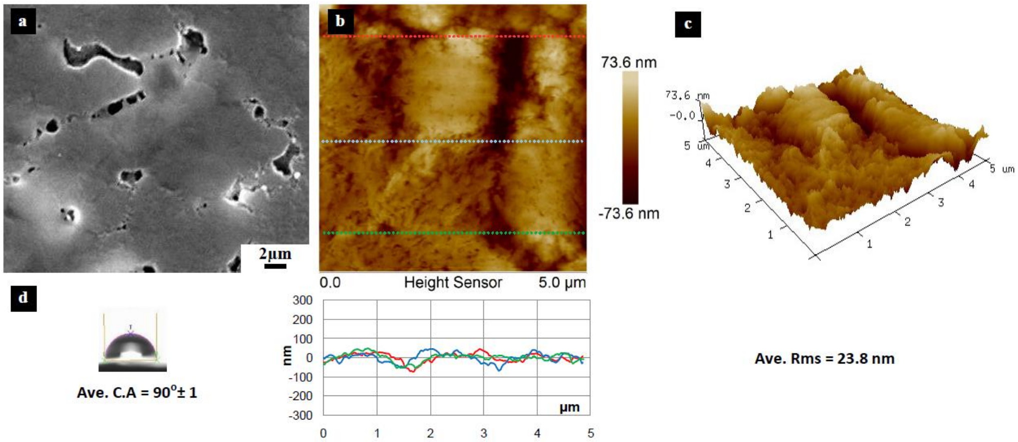

Figure 4-19 Surface characteristics of a received PVDF 5 substrate (20 nm pore size), (a) SEM micrograph, (b) 5x5 μm^2 AFM image (at top) and three section profiles (at bottom) with an average RMS equal to 23.8 nm (c) 3D profile for the selected area, (d) surface contact angle (CA) with an average equal to 90° ± 1.

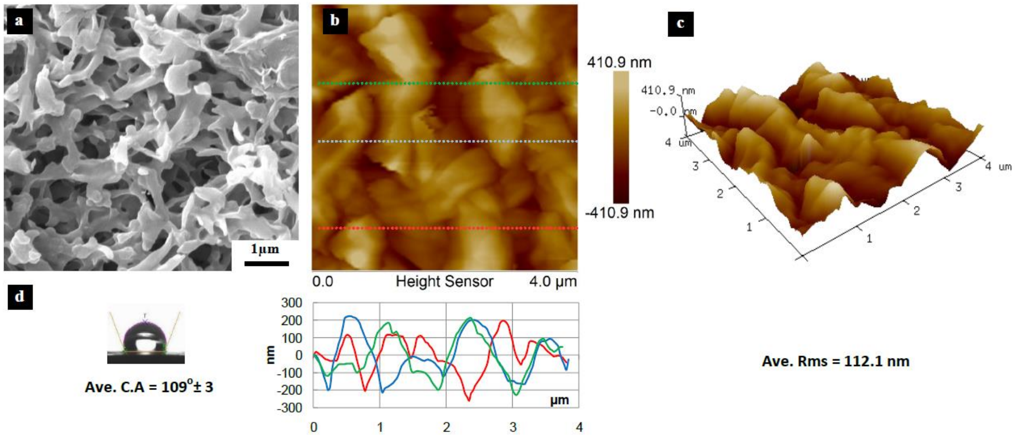

Figure 4-20 Surface characteristics of a received PVDF 6 substrate (100 nm pore size), (a) SEM micrograph, (b) 5x5 μm^2 AFM image (at top) and three section profiles (at bottom) with an average RMS equal to 112.1 nm (c) 3D profile for the selected area, (d) surface contact angle (CA) with an average equal to 109° ± 3.

A PVDF 6 substrate with 100 nm pore size (as shown in Figure 4.20) was found to have the roughest surface (RMS = 112 nm) and a high CA of 109^o due to its large pore size and network structure as seen in the SEM image (Figure 4-20). PVDF 1 substrate with 10 nm pore size was found to have the smoothest surface (RMS = 4.58 nm) and a very low average contact angle (CA= 57^o). The SEM image confirms that PVDF indeed has a smooth surface (Figure 4.15).

Figure 4.21 summarizes the surface characteristics of all of the substrates. As shown in Figure 4.21, the contact angle tends to increase with the surface roughness i.e. the rougher surface are more hydrophobic than smoother surface. This observation is consistent with other findings [274] [275] which also report that the rougher surfaces exhibit high hydrophobicity.

It is not always necessarily true that smaller pore size substrates should have smoother surfaces. PVDF 4, shown in Figure 4.18, has a 10 nm pore size (according to the manufacturer) and higher roughness (RMS= 94.9 nm), when compared to the other 10 nm pore size PVDF substrates (PVDF 1, 2 &3). This has to be related with the substrate cross-sectional porosity and pore structure, i.e. it has a porous surface on the active side and a smoother surface on the opposite side.

Based on the contact angle measurements, four of the eight substrates are considered hydrophilic. These include PES, PVDF 1, PVDF 2 and PVDF 3 (CA<90 ^{o}). The rest of the substrates have a CA>90 ^{o} and are thus considered as hydrophobic.

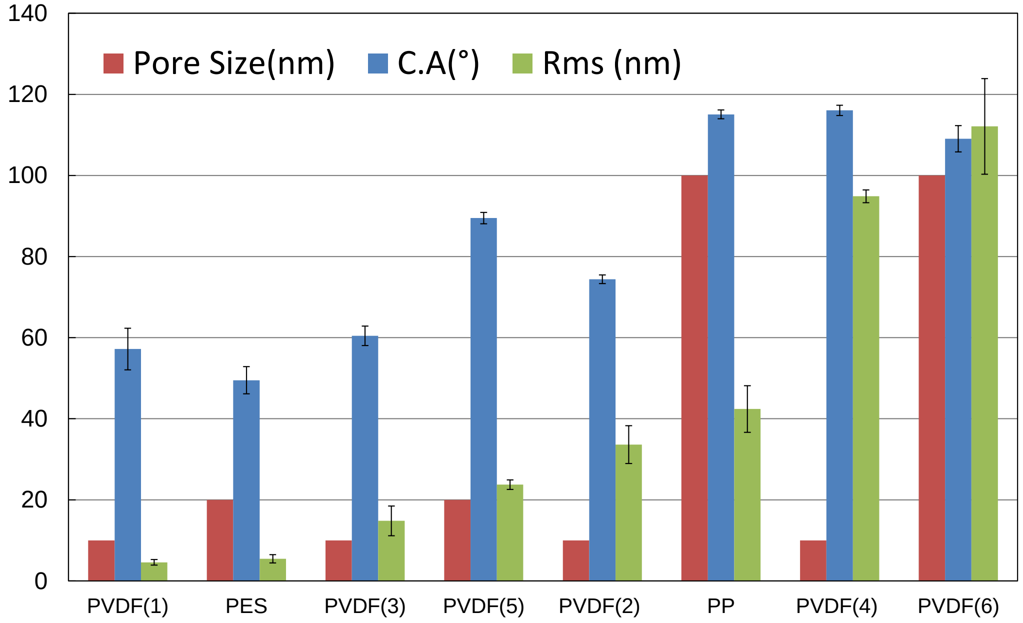

Figure 4-21 Substrates surface characteristics: pore size, the contact angle (C.A) and surface roughness (RMS value).

4.3.2 Etching of Copper Substrate with Graphene.

1 cm^2 pieces of monolayer, bilayer and multilayer graphene samples were floated over 5% (wt/vol) APS solution and the time to achieve complete copper dissolution was recorded, Figure 4.22a-j shows that a monolayer graphene over copper needs almost 180 minutes to completely dissolve copper and yield a free standing graphene monolayer.

The copper substrate was etched within approximately 140 minutes in the case of bi-layer and multi-layer CVD graphene, as shown in Figure 4.23a-h.

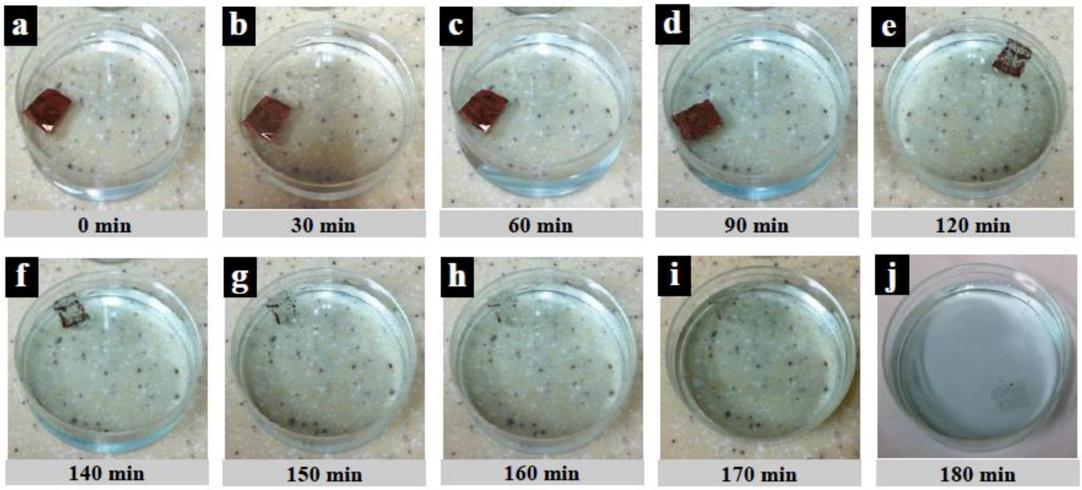

Figure 4-22 Monolayer graphene, time needed for copper etching process

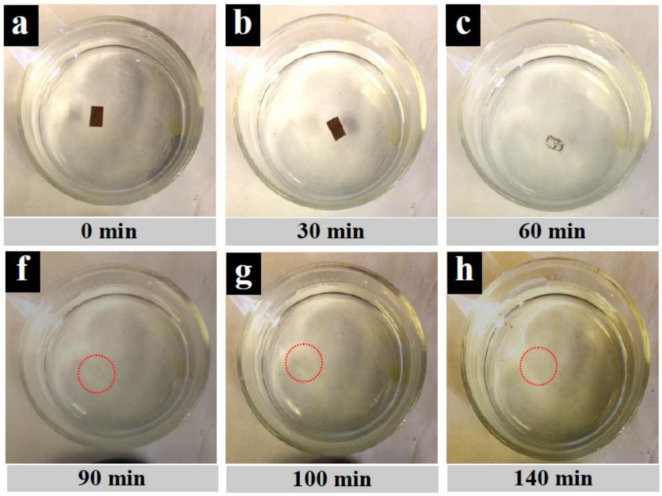

Figure 4-23 Duration time needed to etch completely copper for bilayer and multilayer CVD graphene.

4.3.3 Monolayer Graphene Transfer onto Polymeric Membranes (Preparation of Graphene Membranes)

Monolayer graphene was transferred onto eight different polymeric substrates using the pressing method as described in Section 3.2.3. The resultant transfer could be categorized into three different transferability events of no transfer at all, poor-quality transfer and good-quality transfer.

No transfer (or failed transfer) is encountered when copper/graphene detached from the polymeric substrate during the copper etching step, as shown in Figure 4.24. The good and poor-quality transfers occured when graphene was successfully transferred to the polymeric substrate, but with either a low degree of defects (tears and cracks) or with a high degree of such defects.

Table 4.3 Graphene transferability summary to different polymeric substrates.

No.	**Substrate**	**Pore size (nm)**	**C.A (^{o})**	**RMS (nm)**	**C.A/ RMS**	**Graphene transfer**	**Graphene quality**	**Reason**
1	PP	100	115±1.1	42.4±5.8	2.7	Yes	Good	Low roughness
2	PES	20	50±3.3	5.5±1.0	9.2	Failed	N/A	N/A
3	PVDF 1	10	57±5.1	4.6±0.7	12.4	Failed	N/A	N/A
4	PVDF 2	10	74±1.1	33.6±4.7	2.2	Failed	N/A	N/A
5	PVDF 3	10	60±2.4	14.8±3.7	4.1	Failed	N/A	N/A
6	PVDF 4	10	116±1.3	94.9±1.6	1.2	Yes	Bad	High roughness
7	PVDF 5	20	90±1.4	23.8±1.2	3.8	Yes	Good	Low roughness
8	PVDF 6	100	109±3.2	112.1±11.8	1.0	Yes	Bad	High roughness

Four substrates, PES, PVDF 1, PVDF 2 and PVDF 3 onto which the attempt to transfer monolayer graphene failed were all hydrophilic with water contact angles of lower than 90^o. As the hydrophilic surface gets wets easier as compared to hydrophobic surfaces, the hydrophilic nature of the above four substrates allowsed the APS etchant to penetrate between the substrate and the Cu/graphene layers. This caused interfacial detachment of graphene from the substrate. This detachment process of graphene from the substrate is illustrated in Figure 4.24. The etching process starts with a floating substrate/graphene/Cu composite over the etchant, as shown in Figure 4.24-a. After 30 seconds, the etchant starts to wet the hydrophilic polymeric substrate and penetrates between the substrate and graphene/Cu (Figure 4.24-b). This process continues with time, as shown in Figure 4.24-c, where after approximately 90 seconds, a large air bubble forms between the substrate and graphene/Cu (Figure 4.24-d). The air bubble continues to enlarge and finally causes detachment.

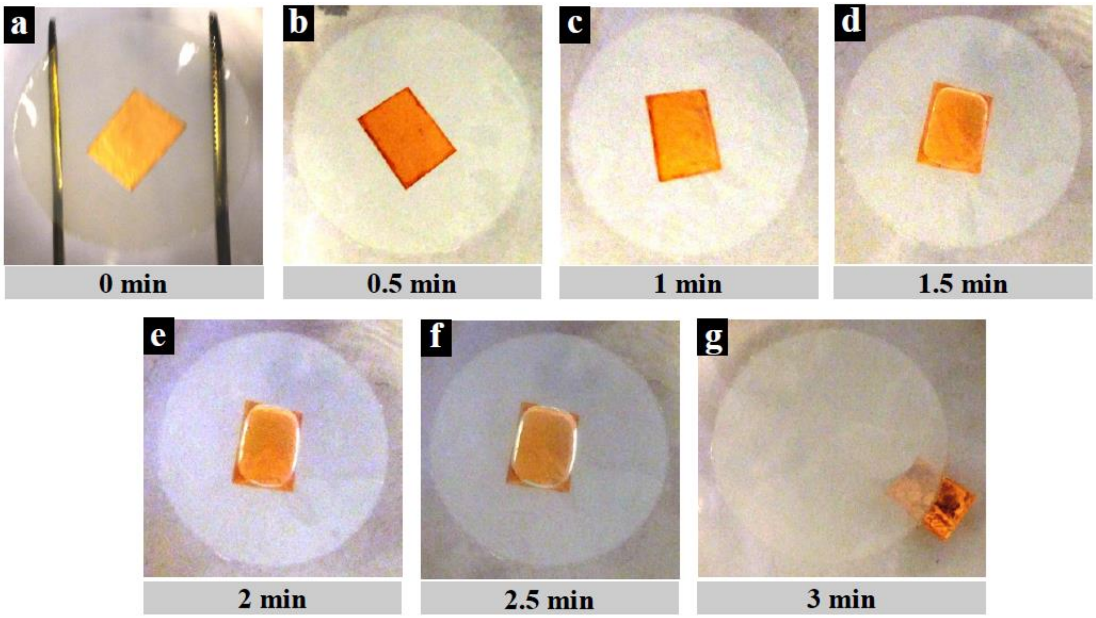

Figure 4-24 Copper/graphene and PVDF 1 substrate detachment process during copper etching step in transfer process, (a) Cu/graphene attached to substrate and floated over APS etchant, (b) after 30 sec, etchant started to penetrate between copper/graphene and substrate from edges (dark regions), (c) after 60 sec, (d) air bubbles get entrapped between Cu/graphene and substrate, (e) after 2 min, air bubble becomes enlarged (f) air bubble tries to cover all the attachment area, (g) Cu/graphene and substrate detachment is completed.

It was thus evident that the polymeric substrate should have an adequate degree of hydrophobicity to prevent etchant penetration between the substrate and graphene interface.

The remaining four substrates (PP, PVDF 4, PVDF 5 and PVDF 6) were hydrophobic with the water contact angle ranging form CA=90^o (PVDF 2) to CA=116^o (PVDF 4). Two of the four substrates, PP and PVDF 5 were smoother as compared to the PVDF 4 and PVDF 6. The PP had a surface roughness = 42.4 nm RMS whereas the RMS surface roughness of PVDF 5, PVDF 4 and PVDF 6 were 23.8 nm, 94.9 nm and 112.1 nm respectively.

4.3.3.1 SEM Characterization of Graphene/Polymeric Substrate Membranes (PP, PVDF 4, PVDF 5 & PVDF 6)

Surface roughness of the substrate has a critical impact on the quality of transferred graphene. Figures 4.25 & 4.26 show SEM micrographs for the successfully transferred graphene over PP and PVDF 5 substrates respectively. An approximately 1x1 cm^2 of monolayer graphene can be viewed by the naked eye as shown in the figure inset at the upper right corner. The FESEM micrographs (Figures 4.25-a & 4.26-a) show a good-quality transferred graphene with some defects (tears and cracks) as indicated by the white arrows. At higher magnification (Figures 4.25-b & 4.26-b) the well-known wrinkles associated with 2D materials can be observed. The presence of these wrinkles provides an evidence of the existence of graphene over the polymeric substrate.

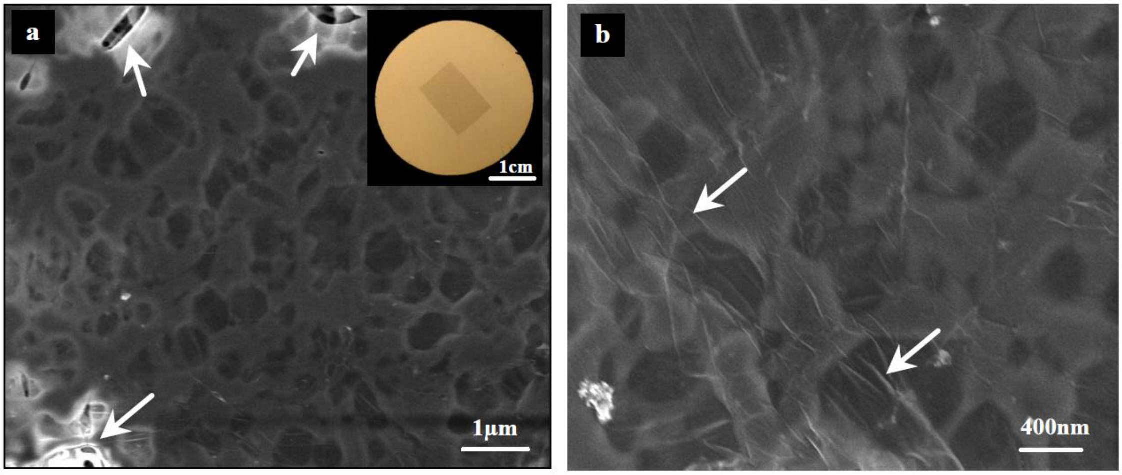

Figure 4-25 FESEM micrograph for the transferred graphene (~ 1x1 cm2) to PP substrate. The white arrows on left image indicate the tears on the graphene revealed during transfer and the arrows on the right image indicates wrinkles within graphene layer [276].

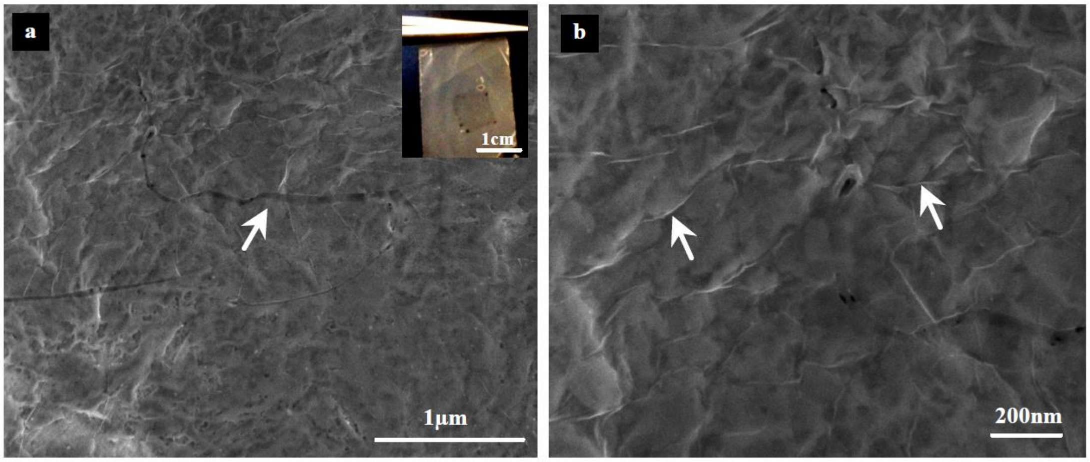

Figure 4-26 FESEM micrograph for the transferred graphene (~ 1x1 cm2) to PVDF 5 substrate. The white arrows indicate wrinkles within graphene layer [276]

Figures 4.27 & 4.28 show FESEM micrographs of poor quality transferred graphene onto PVDF 4 and PVDF 6, respectively. The graphene tore and cracked due to the high surface roughness of both substrates. Discontinuous graphene domains were seen, as shown in Figures 4.27-b and 4.28-b and Figures 4.27-c and 4.28-c. The PVDF 6 substrate which had a higher surface roughness exhibited a more extensive tearing of graphene as compared to the much smoother PVDF 4 substarte. This result supports the argument that the higher surface roughness would result in a poorer quality graphene transfer.

High surface roughness results in poor adherence between graphene and the substrate surface and formation of discontinues graphene domains, as shown in Figures 4.27 and 4.28.

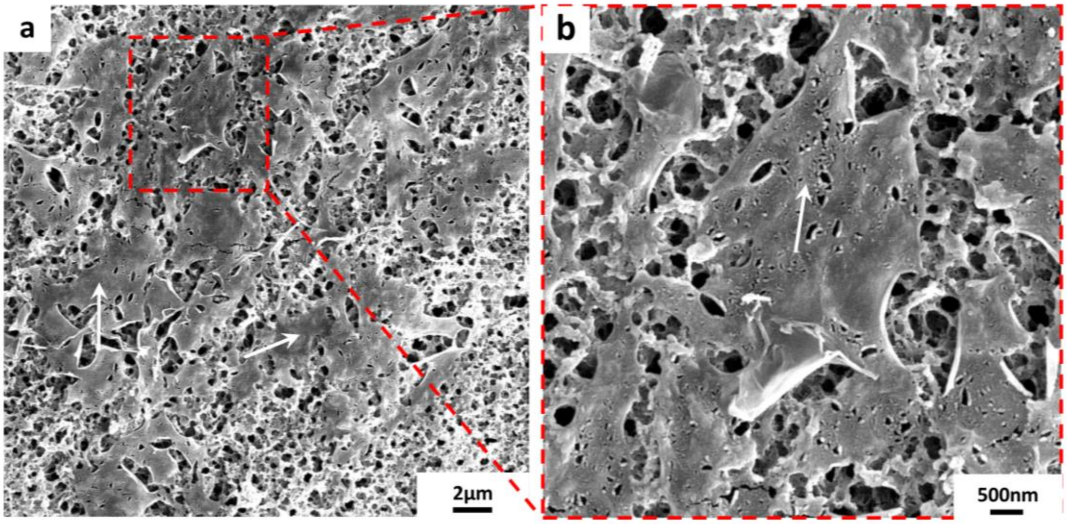

Figure 4-27 FESEM micrographs of the transferred graphene (~ 1x1 cm^2) to PVDF 4 substrate, (a) FESEM of coated graphene/PVDF 4 composite, arrows indicate the discontinuous graphene domains, (b) high magnification FESEM micrograph shows the tears within graphene layer and also shows the underneath PVDF 4 substrate pores.

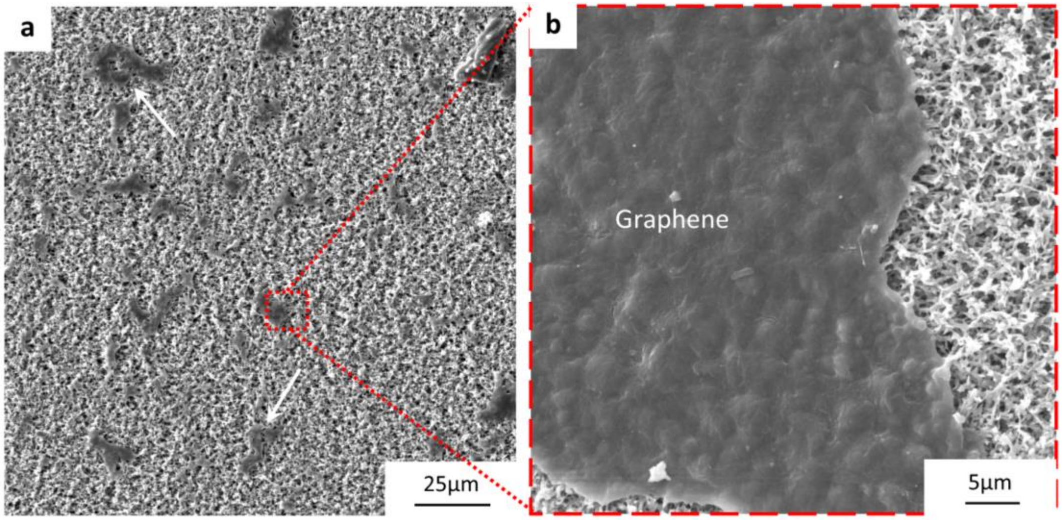

Figure 4-28 FESEM micrographs of the transferred graphene (~ 1x1 cm^2) to PVDF 6 substrate, (a) FESEM of coated graphene/PVDF 6 composite, arrows indicate the discontinuous graphene domains, (b) high magnification FESEM micrograph shows one of graphene domains and the underneath PVDF 6 substrate structure.

4.3.3.2 Ionic Transport Through Graphene/Polymer-Substrate Membranes

Ionic transport of KCl ions through four graphene/polyemr membranes with PP, PVDF 4, PVDF 5 and PVDF 6 as substrates was carried out to check the extent of defects in the transferred graphene monolayer, using a simple diffusion cell in which a 0.5M KCl solution is contained in the cell's left side and de-ionized water in the right side. Due to the concentration difference (caused by osmosis), the KCl ions were transported from the left side toward the right side, passing through the graphene/substrate composite. The rate of ion transport was calculated by monitoring the change of de-ionized water conductivity over time. Based on the fact that graphene is impermeable even for very small species like helium [15, 277], the more ion blockage, the better the quality of graphene. Then, the graphene membrane will be ready to open up the required specific pore size needed through an ion bombardment process, followed by an etching process as proposed by Sean et al. [204].

The diffusion rate of KCl ions was measured by monitoring the change of conductivity with time using an eDAQ conductivity isoPod electrode (eDAQ Pty Ltd) dipped in the de-ionized water side of the cell. A KCl solution with different molarities was prepared, and their conductivities were measured, as seen in Table 4.4. Data in Table 4.4 was plotted to calculate the slope that correlates concentration with conductivity. See Figure 4.29.

Table 4.4 Conductivity of different KCl concentrations

KCl Conc. (M)	Conductivity (mS/cm)
0.05	5.799
0.10	10.220
0.15	14.840
0.20	20.120
0.25	24.970
0.30	29.350
0.35	34.400
0.40	39.350
0.45	43.950
0.50	47.800

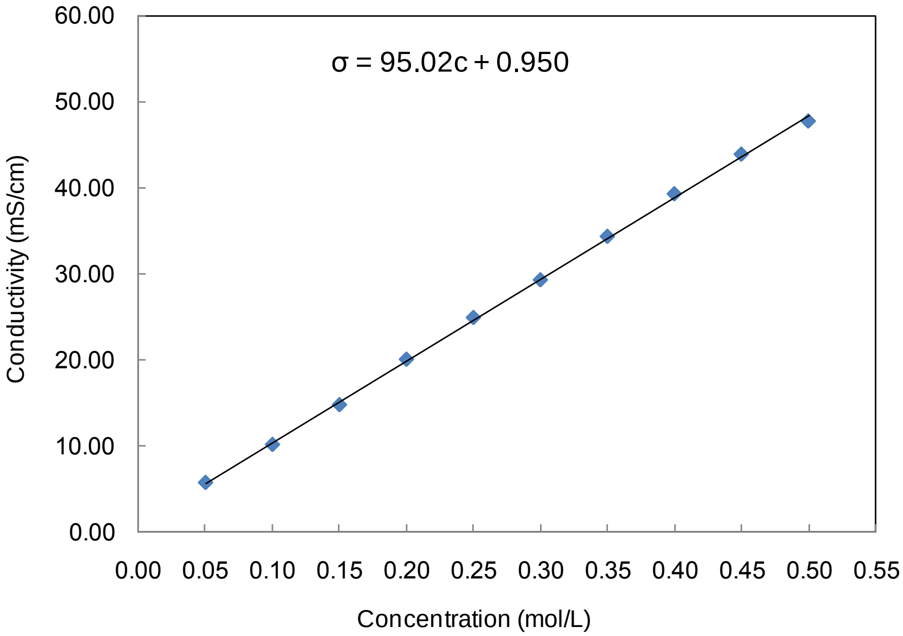

Figure 4-29 KCl conductivity concentration curve; each point in the curve is an average of three measurements.

Figure 4.30 shows the KCl ionic transport thorugh four substrates before and after graphene transfer. PP and PVDF 5 blocked 57% (43% leakage) and 41% (59% leakage) of KCl ions, respectively (Figure 4.30-a and 30-c). On the other hand, PVDF 4 and PVDF 6 blocked only 15% (85% leakage) and 8% (92% leakage) of KCl ions, respectively (Figure 4.30-b and 30-d). These results provides a clear evidence that the quality of transferred graphene over PP and PVDF 5 is far better (possesses far less defects) than in the cases of PVDF 4 and PVDF 6.

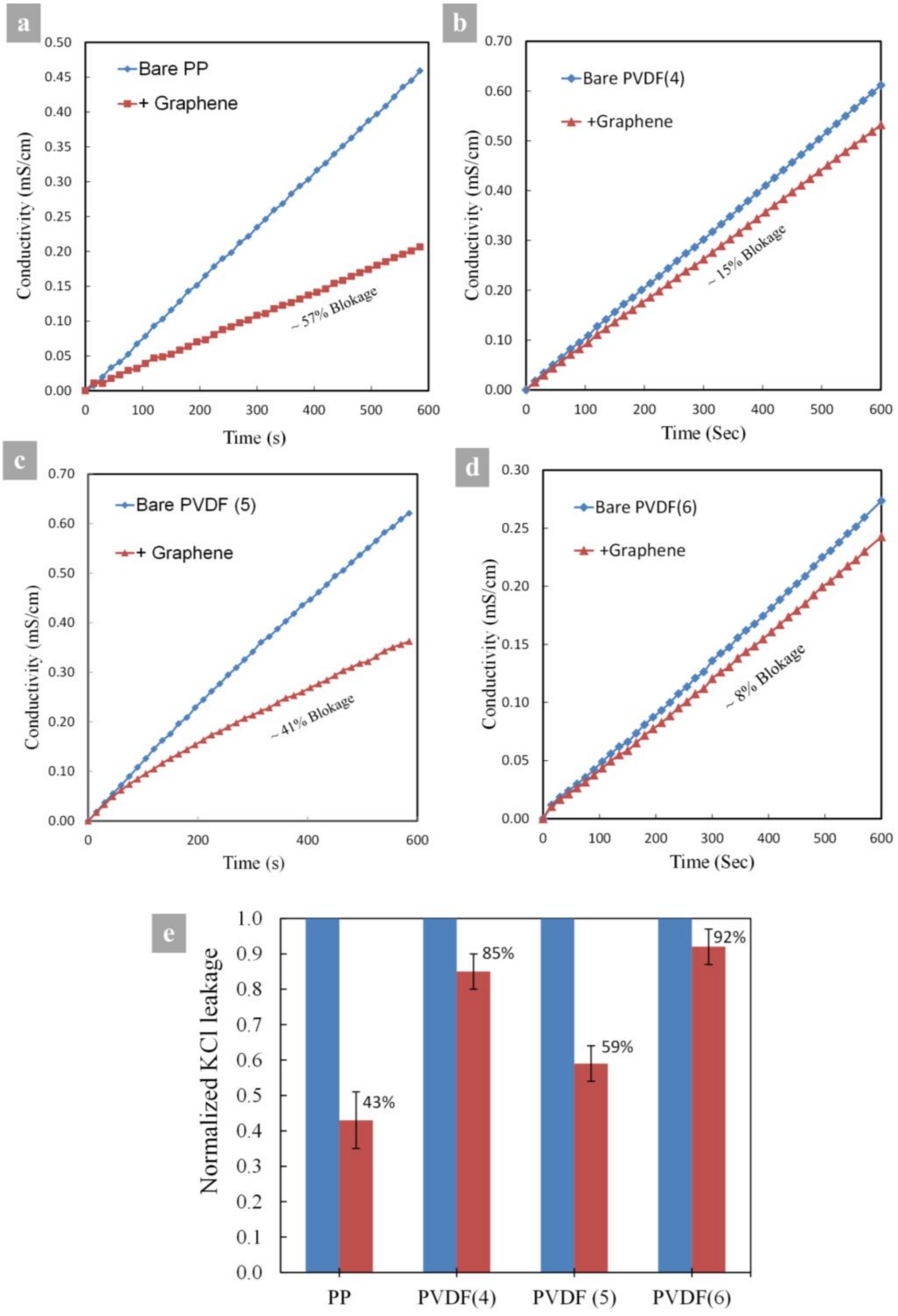

Figure 4-30 Ionic transport measurements of KCl ions passing through substrates before and after graphene transfer, (a) change of conductivity over time for PP substrate, (b) change of conductivity over time for PVDF 4 substrate, (c) change of conductivity over time for PVDF 5 substrate, (d) change of conductivity over time for PVDF 6 substrate, (d) normalized KCl ions leakage for all substrates.

These results also point to the fact that two conditions related to substrate surface characteristics should be controlled in order to achieve a good quality transfer of graphene monolayer on polymeric substrates. First, the substrate surface should be hydrophobic with contact angle > 90° to prevent interfacial penetration of the etchant solution between substrate and graphene/Cu to induce detachment of graphene layer form the substrate during the copper etching step. If this is satisfied, the contact angle (CA) to surface roughness (RMS value) should be higher than 2.7 (CA/RMS > 2.7) otherwise, graphene will transfer but with poor quality, as seen in the cases of PVDF 4 and PVDF 6 (Table 4.3). A high CA/RMS ratio means the substrate has the required hydrophobicity to prevent penetration of the etchant between the Cu/graphene and substrate and also has a low surface roughness which helps in getting better adhesion between the transferred graphene and the substrate [26].

4.3.3.3 Ion Transport Through Defect Sealed Membranes

As mentioned above, large defects (tears, cracks and etc.) found in a graphene layer are usually formed during the transfer process and facilitate ions and other molecular species to leak through the membrane. These defects are plugged and sealed *via* interfacial polymerization of Nylon 6,6 at the defect sites. Figure 4.31-a shows a fluorescent micrograph of a graphene/PVDF composite membrane prior to Nylon 6-6 polymerization. Figure 4.31-b shows a low magnification fluorescent micrograph of a composite graphene/PVDF 5 membrane after IP. The image shows the sites at which Nylon 6,6 is interfacially polymerized as delineated by the orange color originating from the Texas Red fluorescent dye labeling of HDMA. As indicated by arrows, Nylon 6,6 not only sealed the tears and cracks within the graphene layer but, it also sealed large defects produced in the graphene monolayer due to the loss of graphene domains during the transfer process (Figure 4.31-c). The small orange colored spots seen uniformly distributed throughout the image in Figure 4.31-c, result from the fluorescent dye delineating the surface topography of the PVDF 5 bare membrane shown in Figure 4.31-a.

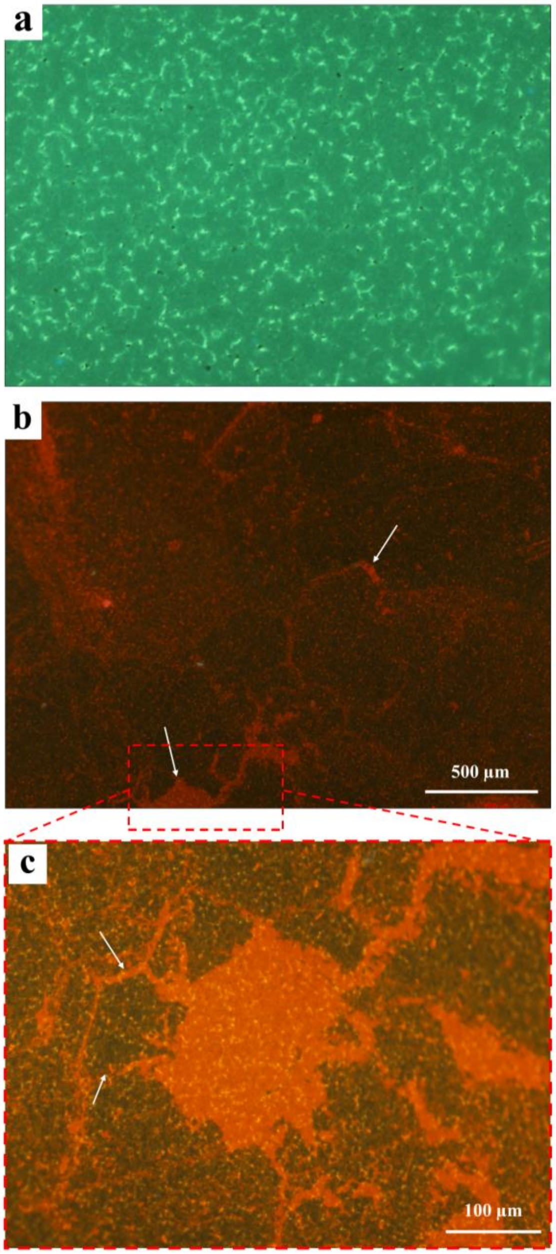

Figure 4-31 Fluorescent micrograph of graphene/PVDF 5 membrane before and after interfacial polymerization of Nylon 6,6. (a) Fluorescent micrograph of bare PVDF 5 membrane. (b) Fluorescent micrograph shows Nylon 6,6 regions at low magnification, white arrows indicate some defects that appear to be sealed by the IP process (c) Magnified fluorescent micrograph shows a graphene domain that was lost during transfer process and was sealed later on with Nylon 6,6 during the IP process (white arrows indicates sealing of even cracks in graphene that may or may not correspond to domain boundaries).

KCl ion transport measurements were repeated after the defect sealing in both graphene/PP and graphene/PVDF 5 membranes. After defect sealing the ion blockage in graphene/PP membranes was improved from 57% to 67% (ion leakage reduced from 43 % to 33%) as shown in Figure 4.32). For the graphene/PVDF 5 membrane, the IP defect sealing was even more effective, and the ion blockage was improved from 40% to 67% (ion leakage reduced from 60% to 33%).

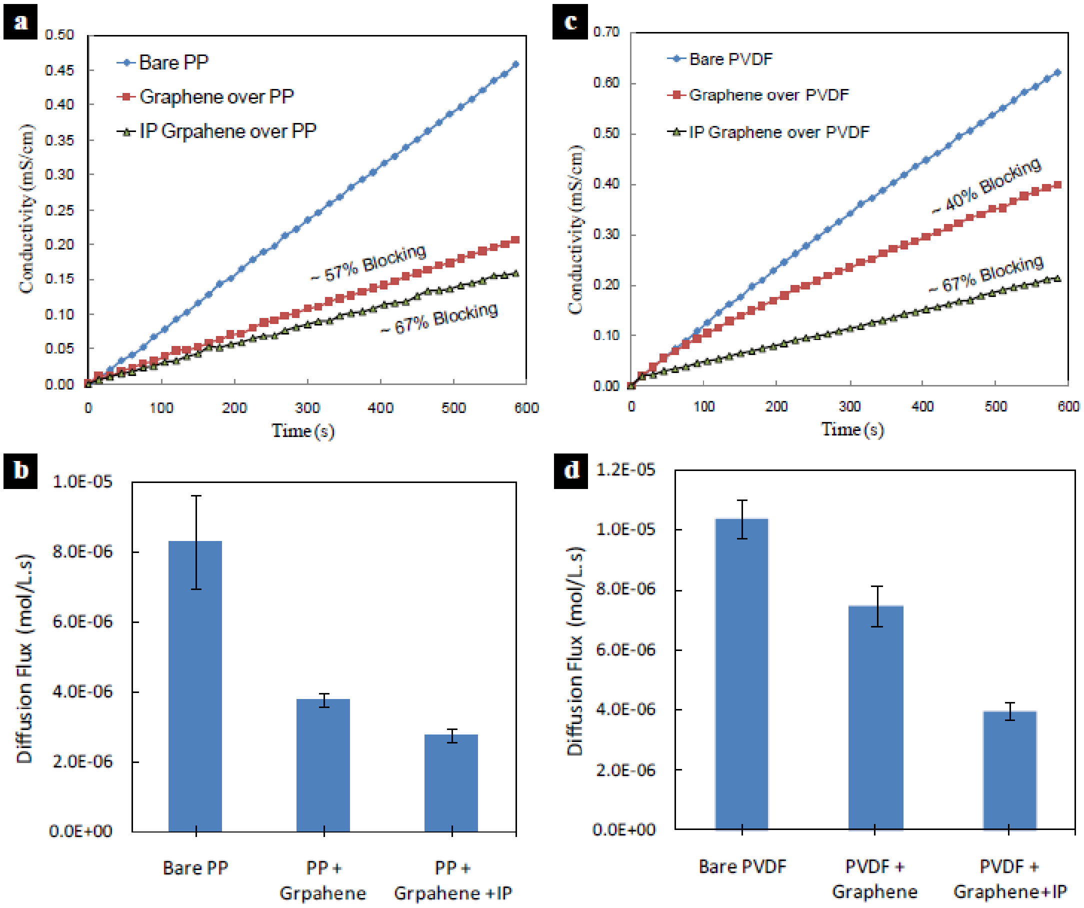

Figure 4-32 0.5M KCl ions conductivity and flux measurements of bare, graphene and IP graphene on both PP and PVDF 5 substrates, (a) Conductivity measurements of bare PP membrane, PP-graphene membrane and defect sealed PP-graphene membrane, (b) KCl ions diffusion flux through PP in all three previous cases. (c) Conductivity measurements of bare PVDF 5 membrane, graphene/ PVDF 5 membrane and defect sealed graphene/ PVDF 5 membrane. (d) KCl ions diffusion flux through PVDF 5 in all three previous cases.

To further enhance the defect plugging, solution B (HDMA) concentration and the IP reaction time were varied. Four different concentrations of solution B (25, 45, 75, and

100 mM) were tested for 5 minutes reaction time on graphene/PP membranes. As displayed in Figure 4.33-a and 4.33-b, the defect sealing *via* Nylon 6,6 became more effective when the HDMA concentration was increased from 25 mM to 75 mM, and the ion blockage increased further from 67 to reach a maximum of 76%. A higher HDMA concentration (100 mM), however, reduced the ion blockage to 52%. Previous studies on Nylon 6,6 polymerization report that there is an optimum concentration ratio between the diamine (HDMA) and adipoyl chloride (APC) at which higher molecular weight (MW) Nylon 6,6 is synthesized. At a higher or lower (HDMA/APC) concentration ratio, poorly-coherent low molecular weight (MW) Nylon 6,6 is produced [278, 279]. Morgan et al. [36] obtained the optimum polymer MW at a diamine to acid chloride ratio of about 6.5. At higher ratios (>6.5), MW was found to decrease due to the greater diffusion of the diamine into the organic phase, and as a result, formed less compact polymer chains. At a lower ratios (<6.5), again the a lower MW polymerization occurred due to the low solubility of the acid chloride in water, as it diffuses only to the film interface, which restricts the depth of Nylon 6,6 polymerization.

With respect to the IP process reaction time; at 75 mM HDMA concentration, our results indicate that the ion blockage deteriorates with increasing the time to 15 minutes and 30 minutes as shown in Figure 4.33-b. This deterioration in the ion blockage characteristics of graphene/PP membrane might be related to the swelling induced in the PP substrate due to longer exposure to hexane. The ion blockage was improved to 84% when the reaction time was reduced to 1 minute; this could be because of less time of exposure to hexane. It is likely that the residual leakage is due to very small defects that cannot be sealed using IP.

Even though such optimization was done, blockage can't surpass 90% due to the intrinsic defects within graphene [19] that can't be sealed by the interfacial polymerization process, which in turn will pass ions through; nevertheless, blockage percentages are expected to be higher than the 8% that is attained with the initial IP process parameters.

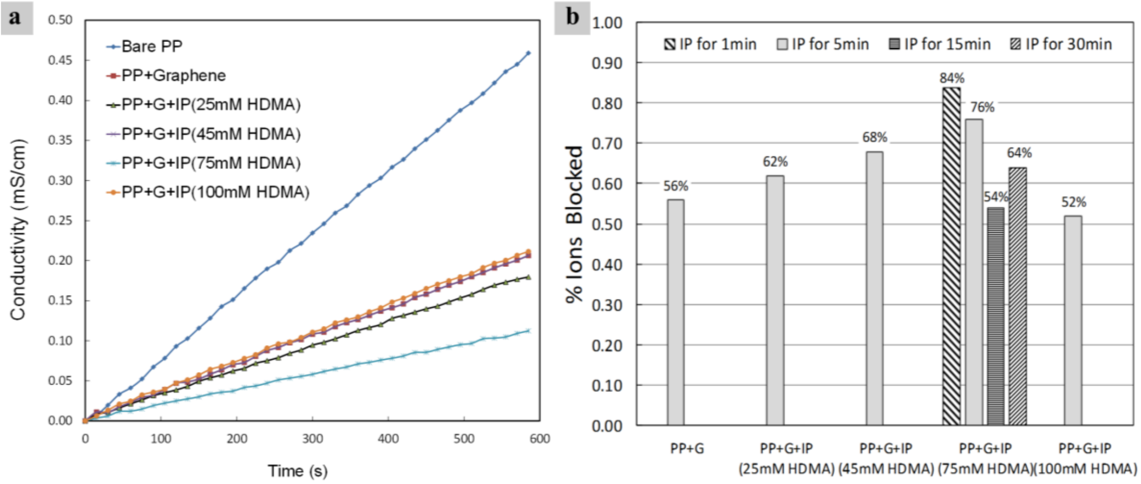

Figure 4-33 IP optimization data, (a) 0.5M KCl ions conductivity measurements while passing through sealed membrane at different HDMA concentrations keeping process duration for 5min. (b) % ion blockage using different HDMA concentrations for 5min IP duration time, and different duration times for 75 mM HDMA concentration case.

4.3.4 Monolayer Graphene Transfer onto Hydrophilic Polymeric Membranes *via* Electrostatic Transfer Method

The hydrophilic substrates (PES, PVDF1, PVDF 2 & PVDF 3) which failed to receive graphene transfer *via* pressing method were tested for transfer with a newly developed transfer method as detailed in Section 3.2.4. Figure 4.34 shows a FESEM of the graphene/PES composite; an approximately 1x1 cm^2 monolayer graphene was transferred using the electrostatic transfer method. A good graphene quality area is captured, as shown in Figure 4.34-a. The arrow within the micrograph indicates a wrinkle, and some copper residues are noticed as well. A higher magnification micrograph is captured that clearly indicates good quality graphene and the underlying PES structure. See Figure 4.34-b.

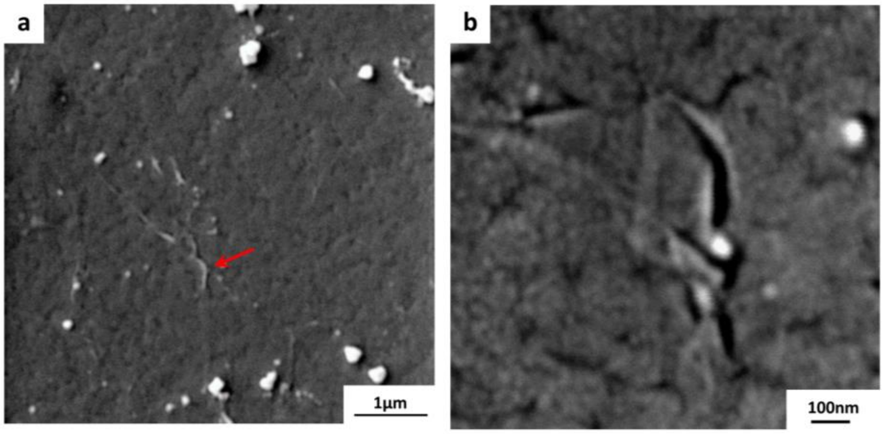

Figure 4-34 FESEM micrographs of the transferred graphene (~ 1x1 cm^2) to PES substrate, the arrow indicates a wrinkle within graphene layer.

Graphene is transferred to a PVDF 1 substrate (having a smooth surface, RMS = 4.6±0.7). Figure 4.35 show the graphene/PVDF 1 composite; FESEM micrographs indicate very good quality and coverage of graphene layer on the polymer substrate. Although some copper residue is found dispersed over the surface, the residual copper does not seem to affect the quality of graphene.

The PVDF 2 substrate which has a rougher surface compared to PVDF 1 and PES was expected to tear and crack the graphene layer, but the quality of transferred graphene was considered acceptable, as shown in Figure 4.36. Figure 4.36-a, b, and c represent the SEM micrograph taken from the samples containing no conductive coating, whereas, Figure 4.36-d represents SEM micrograph taken from a sample with a 10 nm platinum coating. Many wrinkles are notable in the transferred graphene, as indicated by arrows. Tears are also present in the graphene layer, as shown in Figure 4.36-d.

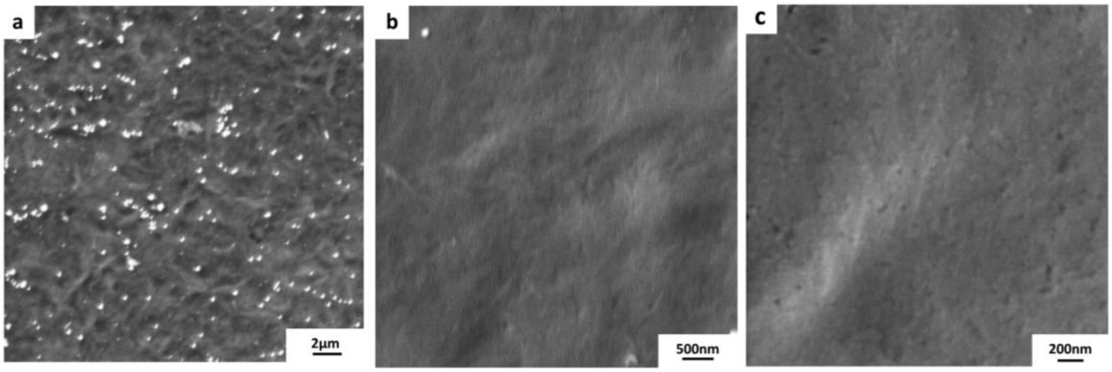

Figure 4-35 FESEM micrographs of the transferred graphene (~ 1x1 cm^2) to PVDF 1 substrate, white spots in the graph (a) could be copper residues.

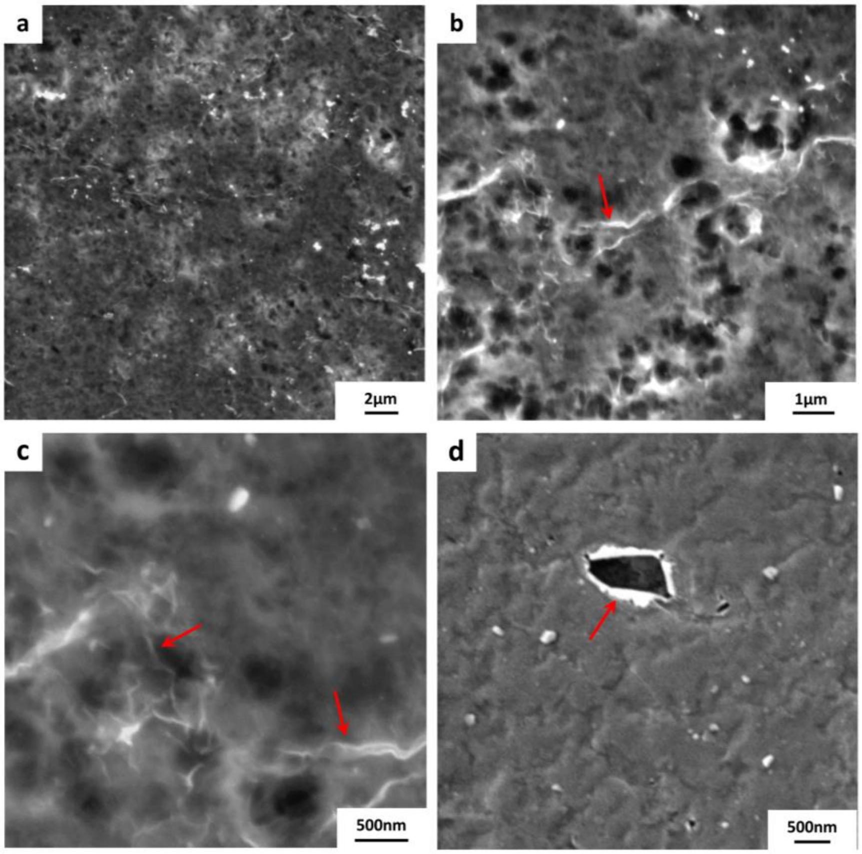

Figure 4-36 FESEM micrographs of the transferred graphene (~ 1x1 cm^2) to PVDF 2 substrate, arrows indicate the wrinkles within graphene layer.

Figure 4.37 show the graphene/PVDF 3 composite. Some cracks and tears are seen within the graphene layer. Magnified FESEM micrographs show wrinkles within the graphene that are again considered as a proof of the existence of graphene on the polymer substrate.

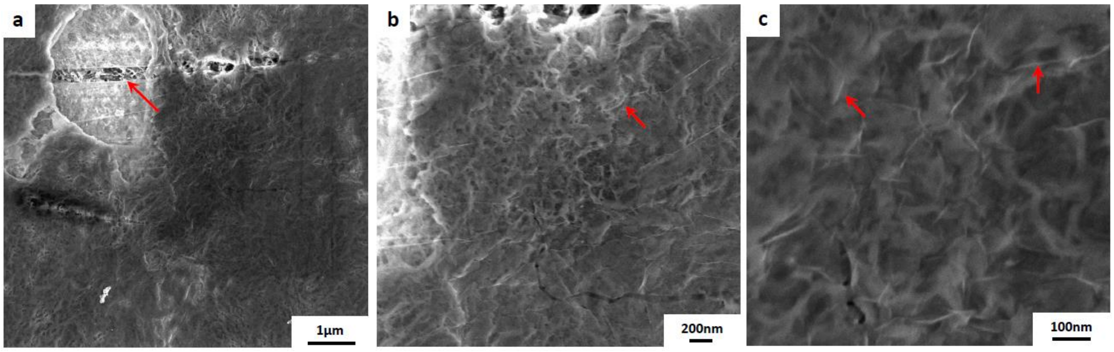

Figure 4-37 FESEM micrographs of the transferred graphene (~ 1x1 cm^2) to PVDF 3 substrate, arrow in (a) indicate the tear within graphene layer and in (b) & (c) indicates the wrinkles within graphene.

4.3.4.1 Ionic transport through graphene/hydrophilic-substrates membranes

KCl ion transport studies were performed for all graphene/hydrophilic substrates to check the quality of the graphene layer. The ionic transport studies were first performed to the hydrophilic substrate covered with graphene, and then, the graphene layer cracks and tears were sealed using the IP of Nylon 6,6 (optimized conditions were applied: 75mM HDMA, 27mM APC and 1 minute duration time).

Figure 4.38 shows results of ion transport. The result show KCl ion blockage of 67%, 70%, 60% and 65% for graphene/PES, graphene/PVDF1, graphene/PVDF2 and graphene/PVDF3 membranes, respectively. The smoothest substrate (PVDF 2) provided the most effective ion blockage, while the roughest substrate (PVDF 2) showed the lowest blockage. All hydrophilic substrates were found to provide better KCl ion blocking than the hydrophobic PP and PVDF 5 substrates. It is worth mentioning that in the case of PP and PVDF 5 substrates transfer of graphene was carried out via press transfer method (Section 3.2.3) whereas the newly developed electrostatic transfer method was adopted. This means that the electrostatic transfer method seems to be much better process for graphene transfer than the press transfer method. This should obviously be expected as the electrostatic transfer method does not involve any mechanical forces that cause cracking and tearing of the graphene layer.

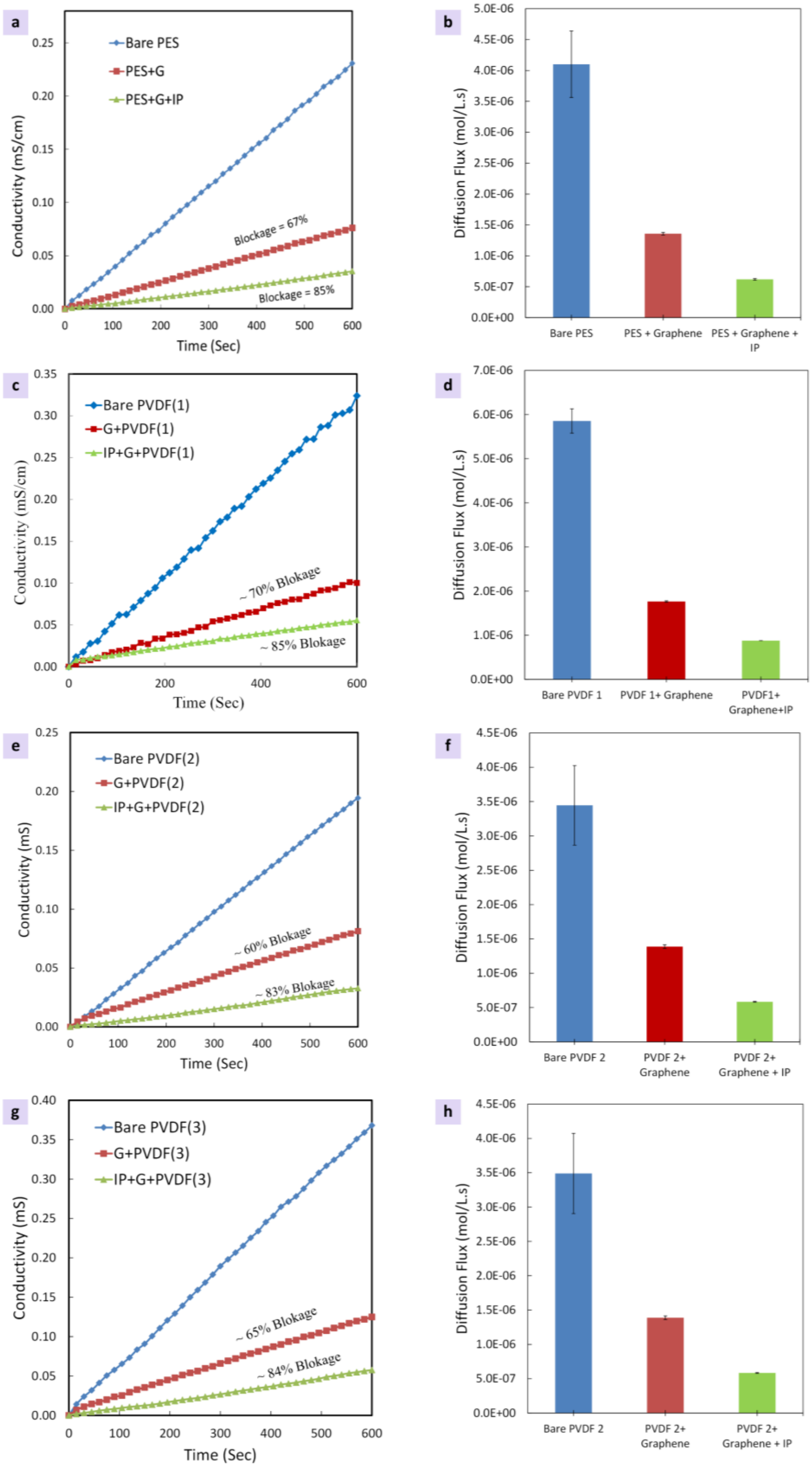

Figure 4-38 The ionic transport measurements for all graphene/hydrophilic substrates (PES, PVDF 1, PVDF 2 & PVDF 3).

The graphene transfer on hydrophilic substrates via electrostatic charge is still prone to produce tears and cracks in the graphene mono as indicated by the ion transport which does not reach to 100%. However after defect sealing by interfacial polymerization of Nylon 6,6 ion blockage of 83% to 85% were obtained. Although the ion blockage was noticeably improved, the membranes still leaked about 15% of KCl ions. It is known that 10% of ion leakage occurs through intrinsic defects within the graphene layer that cannot be sealed with the IP process. These intrinsic defects can be sealed via atomic layer deposition of Hafnium. The remaining few perecent leakage can be stopped by further optimization of the Nylon ,6,6 IP process to produce a totally impervious graphene/polymer membrane as the most sought after first step to produce nano porous graphene membranes for the desired application.

Figure 4.39 summarizes the normalized ion leakage for all graphene/polmer membranes considered in this study. It shows the leakage of different stages for each membrane. As an example, PVDF 1 bare substrate leaks 100% of ions. After monolayer graphene transfer the ion leakage decreased to 30%, which was further reduced to 15% after sealing the defects by Nylon 6,6. PVDF 1 thus exhibited the best ion blockage (lowest ion leakage) while PVDF 6 showed the worst blockage.

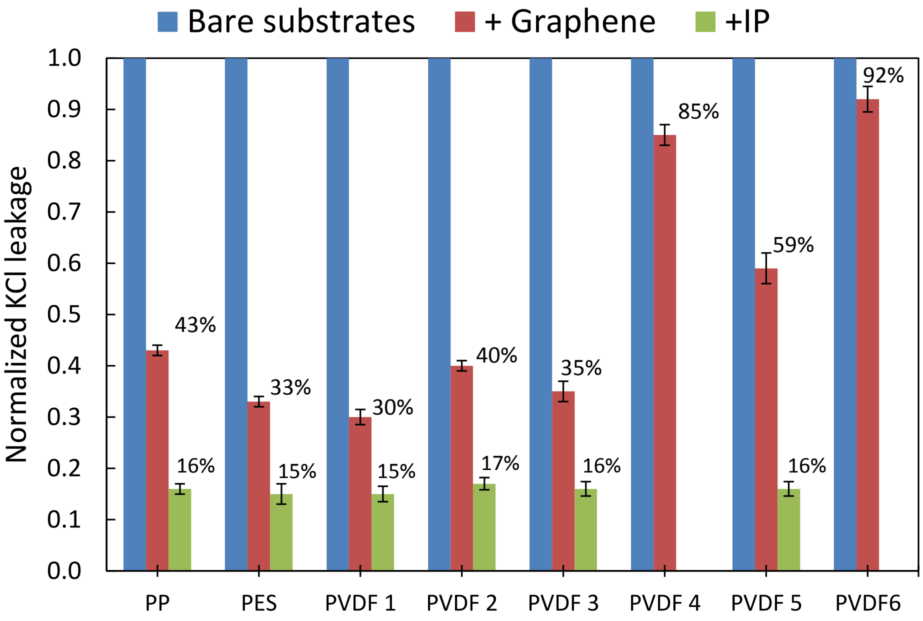

Figure 4-39 Summary of normalized KCl ion leakage percentages for all polymeric substrates.

4.4 Bilayer Graphene Transfer onto PP Membrane

Bi-layer graphene was transferred onto a PP substrate using the pressing transfer method. Figure 4.40 shows the FESEM micrographs of the transferred graphene. As with case of the monolayer, bilayer graphene also shows a good quality graphene transfer with usual cracks and tears.

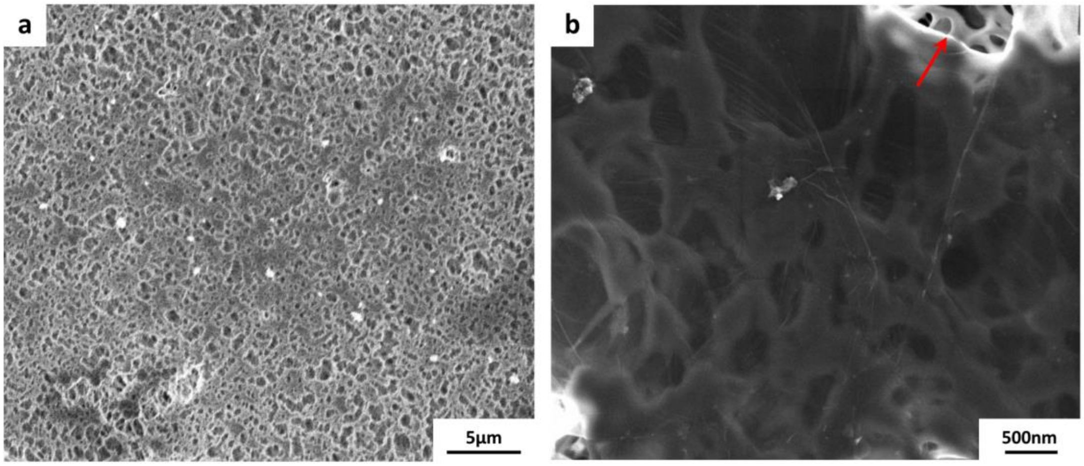

Figure 4-40 FESEM micrographs of the transferred bi-layer graphene (~ 1x1 cm^2) onto PP substrate, arrow in (b) indicates the tear within graphene layer.

Figure 4.41 shows ion blockage of bi-layer graphene/PP membrane. The blockage improved slightly to 60% as against 57% observed for the monolayer graphene/PP membrane. The blockage was further enhanced to 75% after sealing the defects while for the monolayer graphene/PP this was about 84%. This could be attributed to the inability of the two monomers solution to meet at the defect sites through two layers and polymerize to as efficiently seal the defects as occurs in monolayer graphene

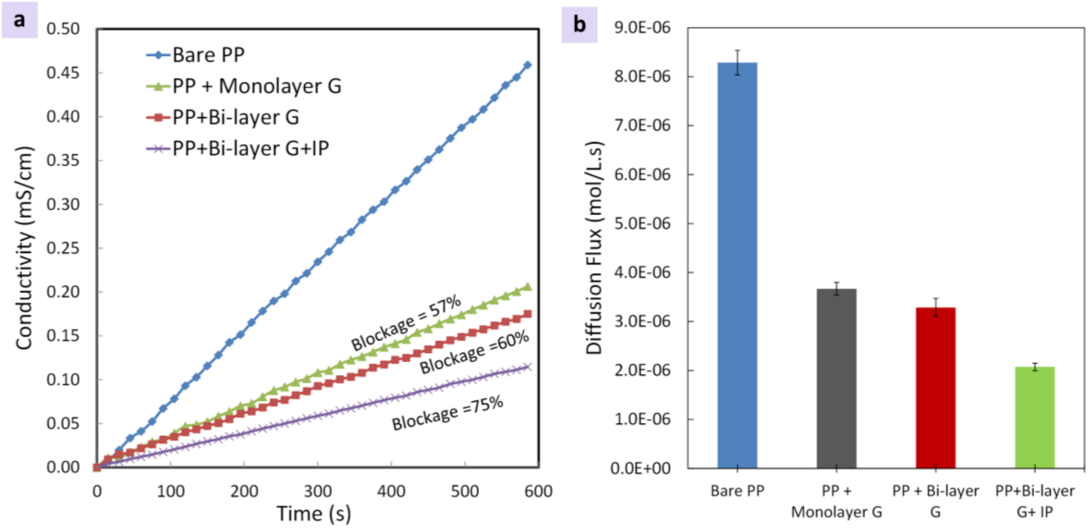

Figure 4-41 KCl ionic transport measurements of bi-layer graphene/PP substrates with and without IP of Nylon 6,6.

4.5 Multilayer Graphene Transfer onto PP Membrane

In addition to monolayer and bilayer graphene, multilayer graphene was also transferred to the PP substrate using the pressing transfer method. Figure 4.42 shows the FESEM micrograph of the multi-layer graphene/PP membranes. The figure reveals a good transfer. The higher density of wrinkles was noted in the case of multilayer graphene, as shown in Figure 4.42-b. This is expected since there are multiple graphene layers stacked over each other which would induce more wrinkling.

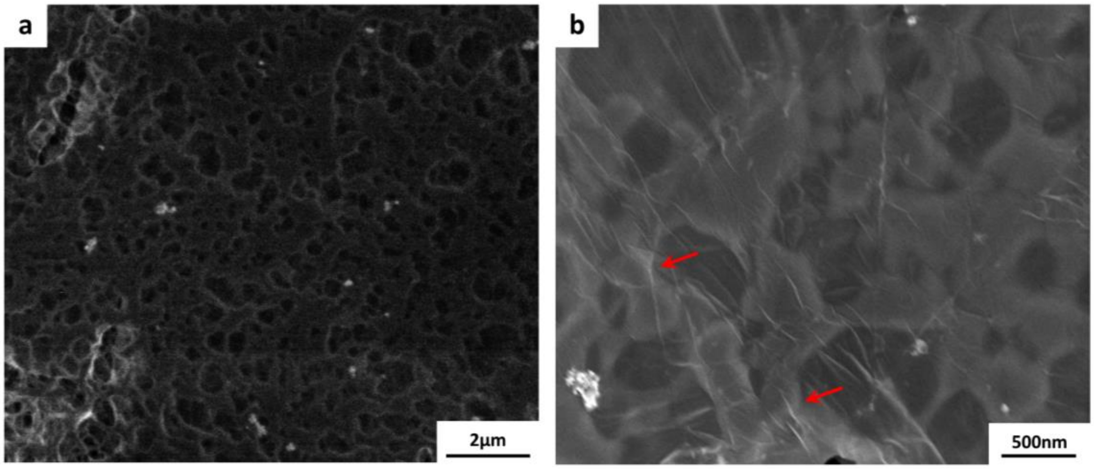

Figure 4-42 FESEM micrographs of the transferred multilayer graphene (~ 1x1 cm^2) onto PP substrate, arrow in (b) indicates the wrinkles within graphene layer.

Surprisingly, multi-layer graphene/PP membrane composite blocked 82% of KCl ions without defect sealing, (Figure 4.43-a) as compared to 57% and 60% for the mono and bilayer graphene/PP membranes respectively. This enhanced ion blockage of multi-layer graphene could be attributed to the sealing of the tears and cracks by layers through a self-sealing phenomenon of overlapping graphene layers.

Interfacial polymerization of Nylon 6,6 was also performed for the multi-layer graphene/PP membrane. As shown in Figure 4.43, a very small improvement was achieved, which can be attributed to the same explanation as provided for the bilayer case discussed above.

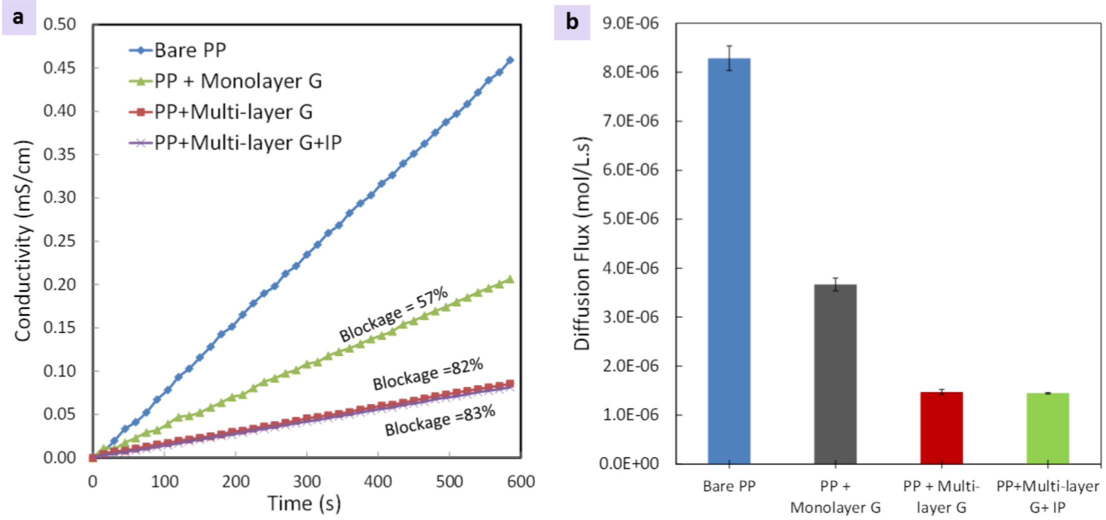

Figure 4-43 KCl ionic transport measurements of multi-layer graphene/PP substrates with and without IP of Nylon 6,6.

4.6 Biofouling Resistance of Graphene Membranes

Figure 4.44 shows the short-term E- coli bacterial adhesion results for PES, PVDF 1 and PP graphene membranes. The test was carried out for bare membranes (without graphene) and then repeated for the membranes after graphene transfer. A total of 10 images were taken from different locations for each membrane sample. The number of cells was manually counted for each image at the magnification of 2000 X and the average value calculated. The average number of cells on the membrane was normalized by the observed membrane area (0.0027 mm^2) and plotted as a bar chart (Figure 4.44-f). The graphene layer reduced the bacterial adhesion on the PES by an approximately 51% (Figure 4.44-a and b). A reduction of ~ 94% bacterial adhesion was observed for the case of PVDF 1 (Figure 4.44-c and d). PP membranes showed almost zero bacterial adhesion before graphene coverage, and when covered with graphene (Figure 4.44-e), ~ 6000 cells/mm^2 of E- coli bacteria adhered to the membrane surface (Figure 4.44-f).

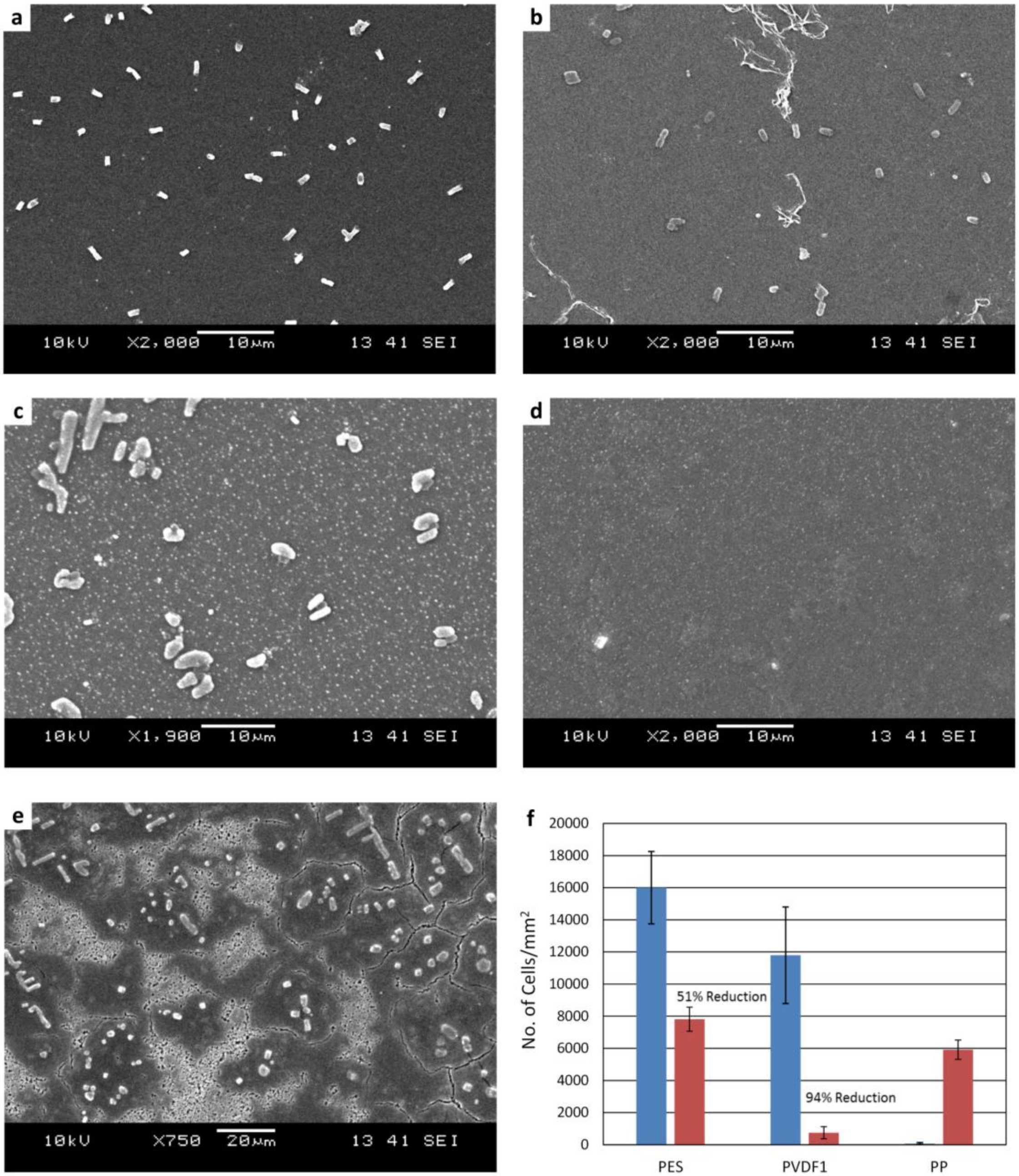

Figure 4-44 SEM micrographs for: PES substrate (a) without graphene layer, (b) with graphene, PVDF 1 substrate (c) without graphene layer, (d) with graphene and PP substrate (e) zones of with and without graphene. (f) No. of cells/mm2 of PES, PVDF1 and PP with graphene compared to bares (without graphene).

4.7 Water Flux and Salt Rejection of Graphene/PP Membrane

Brackish water (2000ppm) was used to measure the transport and rejection of the bare PP and graphene/PP membrane at different pressures. The permeation was carried out using the dead end cell. Figure 4.45 shows that with increasing pressure the water flux increases. Compared to the bare PP, graphene/PP permeate flux was lower at all pressures but at the expense of salt rejection (Figure 4.46). Graphene/PP rejected 60% of salt at 50 psi and 44% at 200 psi confirming the presence of defects within graphene layer.

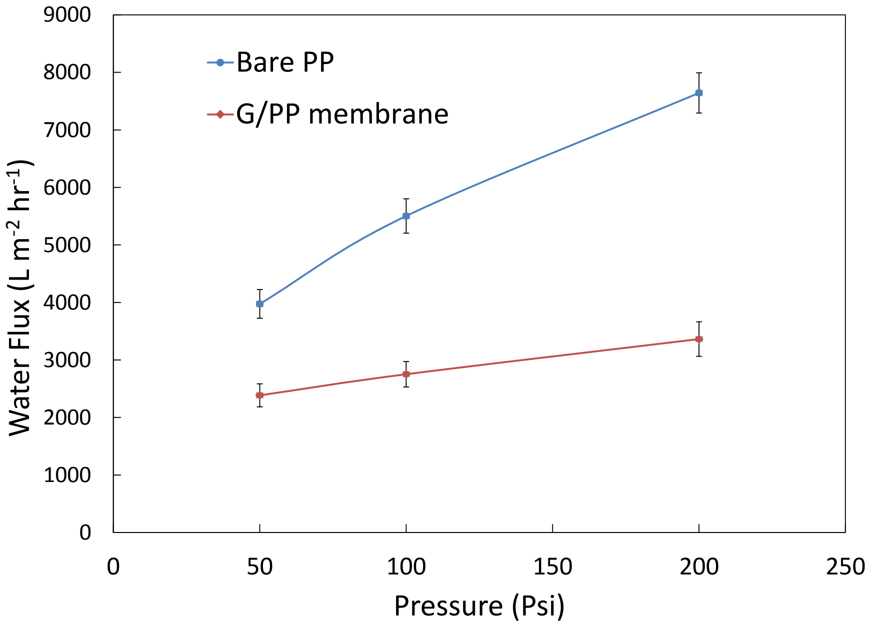

Figure 4-45 Graphene/PP permeation water flux for bare PP compared with graphene/PP membrane at different pressures.

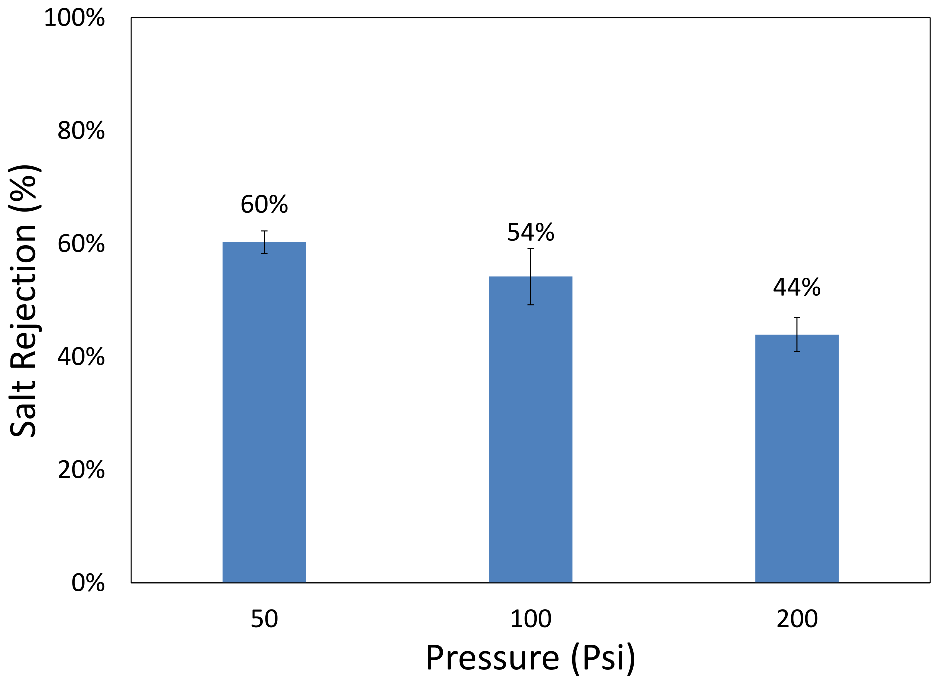

Figure 4-46 Salt rejection of bare PP compared with graphene/PP membrane at different pressures.

CHAPTER 5

CONCLUSION

The present work explored the transfer of graphene onto a polymeric support with an aim to obtain a defect free graphene monolayer/polymer composite for an eventual fabrication of nanoporous water purification membrane. CVD monolayer graphene was transferred to eight different polymeric substrates, having different surface characteristics The following are key findings of this work:

1. To obtain a good quality graphene transfer, the surface should be smooth. The smooth surface allows a conformal adhesion of graphene to the support substrate with minimum tears and cracks.
2. The support substarte should have high hydrophobicity to prevent etchant penetration during copper etching.
3. The graphene failed to transfer over four substrates (PES, PVDF 1, PVDF 2 & PVDF 3) because they were hydrophilic and allowed etchant solution to penetrate into the Cu/graphene and substrate interface and caused detachment of graphene layer from the substrate.
4. To get high-quality graphene, the ratio of the contact angle to the root mean square (RMS) should be higher than 2.7 (CA/RMS > 2.7).
5. Graphene successfully transferred onto other four hydrophobic support substrates (PP, PVDF 4, PVDF 5 and PVDF 6).

6. The press transfer process induced significant defects (tears and cracks) in the graphene layer deposited on the support substrate.
7. To examine the extent of these defects diffusion of potassium chloride (KCl) ions through graphene/polymer composite membrane was measured. The graphene/PP membrane blocked 57% of the KCl ions (i.e. 43% leakage occurred through the defects) whereas the ionic blockage was around 40% (i.e. 60 % leakage occurred through the defects) for the graphene/PVDF membranes.
8. The transfer process-induced defects in the graphene monolayer were sealed with interfacial polymerization of Nylon 6,6 into the defect sites. The sealing of the defects with Nylon increased the ion blockage to form 57% to 67% (reduced leakage from 43% to 33%) for both PP and PVDF membranes. The optimization of the IP process further enhanced the ion blockage to 84% (reduced leakage to 16%) in the graphene/PP membranes.
9. A new transfer method was developed for successfully transfering monolayer graphene onto hydrophilic substrates. The process utlilized an electrostatic charge during the etching process to prevent etchant penetration into the graphene/polymer interface and thus prevent delamination of graphene from the polyemr support substrate.
10. After sealing the defects within the graphene layer, graphene/hydrophilic composite membranes successfully blocked 83% to 85% of KCl ions.
11. Bi-layer and multi-layer graphene was transferred to PP substrate. After defect sealing, the bi-layer graphene blocked 73% of KCl ions whereas multilayer graphene transfer to PP without IP successfully blocked 82% of KCl ions.

12. Static bacteria adhesion tests of E- coli were performed on PP, PES and PVDF 1/ graphene membranes to examine their biofouling resistance. Compared to the bare substrates, the graphene layers reduced e-coli becterial adhesion by 51% and 94% for the PES and PVDF 1 membranes, respectively.
13. The bare PP substrate showed almost complete resistance to bacterial adhesion but showed a surprizing enhancement of bacterial adhesion with the presence of graphene layer.
14. Graphene/PP membrane showed higher water flux and much lower salt rejection compared to the RO commercial membranes, which confirms the existance of both the intrinsic defects and the residual tranfser-induced defects in the graphene mono layer.

CHAPTER 6

FUTURE WORK

- More research is needed to develop more effective methodologies which will allow trasfer of a totally defect free and impervious graphene mono layer/polymer support.
- Once the above is achived research efforts must be directed to produce nanoporous graphene (NPG) with the desirable pore size required for specific application.
- The newly developed electrostatic transfer method could be further explored and optimized for defect free transfer of mono layer graphene onto both hydrophobic and hydrophilic support substrates.
- More work can be directed to explore the transfer of multilayer graphene which may provide an effective self sealing of the interinsic and transfer induced defects.

REFERENCES

[1] M. Al-Ahmad, F. A. Aleem, A. Mutiri, and A. Ubaisy, "Biofuoling in RO membrane systems Part 1: Fundamentals and control," *Desalination,* vol. 132, pp. 173-179, 2000.

[2] E. Cornelissen, D. Harmsen, K. De Korte, C. Ruiken, J.-J. Qin, H. Oo, *et al.*, "Membrane fouling and process performance of forward osmosis membranes on activated sludge," *Journal of Membrane Science,* vol. 319, pp. 158-168, 2008.

[3] M. Goosen, S. Sablani, H. Al-Hinai, S. Al-Obeidani, R. Al-Belushi, and D. Jackson, "Fouling of reverse osmosis and ultrafiltration membranes: a critical review," *Separation Science and Technology,* vol. 39, pp. 2261-2297, 2005.

[4] D. Paul and A. R. M. Abanmy, "Reverse osmosis membrane fouling–the final frontier," *Ultra Pure Water,* vol. 7, pp. 25-36, 1990.

[5] M. Herzberg and M. Elimelech, "Biofouling of reverse osmosis membranes: role of biofilm-enhanced osmotic pressure," *Journal of Membrane Science,* vol. 295, pp. 11-20, 2007.

[6] R. Nair, H. Wu, P. Jayaram, I. Grigorieva, and A. Geim, "Unimpeded permeation of water through helium-leak–tight graphene-based membranes," *Science,* vol. 335, pp. 442-444, 2012.

[7] M. A. Shannon, P. W. Bohn, M. Elimelech, J. G. Georgiadis, B. J. Marinas, and A. M. Mayes, "Science and technology for water purification in the coming decades," *Nature,* vol. 452, pp. 301-310, 2008.

[8] D. Cohen-Tanugi and J. C. Grossman, "Water desalination across nanoporous graphene," *Nano letters,* vol. 12, pp. 3602-3608, 2012.

[9] E. N. Wang and R. Karnik, "Water desalination: Graphene cleans up water," *Nature nanotechnology,* vol. 7, pp. 552-554, 2012.

[10] T. Humplik, J. Lee, S. O'hern, B. Fellman, M. Baig, S. Hassan, *et al.*, "Nanostructured materials for water desalination," *Nanotechnology,* vol. 22, p. 292001, 2011.

[11] M. Hu and B. Mi, "Enabling graphene oxide nanosheets as water separation membranes," *Environmental science & technology,* vol. 47, pp. 3715-3723, 2013.

[12] Ç. Ö. Girit, J. C. Meyer, R. Erni, M. D. Rossell, C. Kisielowski, L. Yang, *et al.*, "Graphene at the edge: stability and dynamics," *science,* vol. 323, pp. 1705-1708, 2009.

[13] S. Chen, Q. Wu, C. Mishra, J. Kang, H. Zhang, K. Cho, *et al.*, "Thermal conductivity of isotopically modified graphene," *Nature materials,* vol. 11, pp. 203-207, 2012.

[14] C. Lee, X. Wei, J. W. Kysar, and J. Hone, "Measurement of the elastic properties and intrinsic strength of monolayer graphene," *science,* vol. 321, pp. 385-388, 2008.

[15] J. S. Bunch, S. S. Verbridge, J. S. Alden, A. M. van der Zande, J. M. Parpia, H. G. Craighead, *et al.*, "Impermeable atomic membranes from graphene sheets," *Nano letters,* vol. 8, pp. 2458-2462, 2008.

[16] J. Despres, E. Daguerre, and K. Lafdi, "Flexibility of graphene layers in carbon nanotubes," *Carbon Nanotubes,* p. 149, 1996.

[17] F. o. Perreault, M. E. Tousley, and M. Elimelech, "Thin-film composite polyamide membranes functionalized with biocidal graphene oxide nanosheets," *Environmental Science & Technology Letters,* vol. 1, pp. 71-76, 2013.

[18] K. Celebi, J. Buchheim, R. M. Wyss, A. Droudian, P. Gasser, I. Shorubalko, *et al.*, "Ultimate permeation across atomically thin porous graphene," *Science,* vol. 344, pp. 289-292, 2014.

[19] S. C. O'Hern, C. A. Stewart, M. S. Boutilier, J.-C. Idrobo, S. Bhaviripudi, S. K. Das, *et al.*, "Selective molecular transport through intrinsic defects in a single layer of CVD graphene," *ACS nano,* vol. 6, pp. 10130-10138, 2012.

[20] S. C. O'Hern, M. S. Boutilier, J.-C. Idrobo, Y. Song, J. Kong, T. Laoui, *et al.*, "Selective ionic transport through tunable subnanometer pores in single-layer graphene membranes," *Nano letters,* vol. 14, pp. 1234-1241, 2014.

[21] S. C. O'Hern, D. Jang, S. Bose, J.-C. Idrobo, Y. Song, T. Laoui, *et al.*, "Nanofiltration across Defect-Sealed Nanoporous Monolayer Graphene," *Nano letters,* 2015.

[22] M. S. Boutilier, C. Sun, S. C. O'Hern, H. Au, N. G. Hadjiconstantinou, and R. Karnik, "Implications of permeation through intrinsic defects in graphene on the design of defect-tolerant membranes for gas separation," *ACS nano,* vol. 8, pp. 841-849, 2014.

[23] S. P. Koenig, L. Wang, J. Pellegrino, and J. S. Bunch, "Selective molecular sieving through porous graphene," *Nature nanotechnology,* vol. 7, pp. 728-732, 2012.

[24] J. Kang, D. Shin, S. Bae, and B. H. Hong, "Graphene transfer: key for applications," *Nanoscale,* vol. 4, pp. 5527-5537, 2012.

[25] U. Stöberl, U. Wurstbauer, W. Wegscheider, D. Weiss, and J. Eroms, "Morphology and flexibility of graphene and few-layer graphene on various substrates," *Applied Physics Letters,* vol. 93, p. 051906, 2008.

[26] L. G. Martins, Y. Song, T. Zeng, M. S. Dresselhaus, J. Kong, and P. T. Araujo, "Direct transfer of graphene onto flexible substrates," *Proceedings of the National Academy of Sciences,* vol. 110, pp. 17762-17767, 2013.

[27] W. Gao and R. Huang, "Effect of surface roughness on adhesion of graphene membranes," *Journal of Physics D: Applied Physics,* vol. 44, p. 452001, 2011.

[28] K. S. Novoselov, A. K. Geim, S. Morozov, D. Jiang, Y. Zhang, S. Dubonos, *et al.*, "Electric field effect in atomically thin carbon films," *science,* vol. 306, pp. 666-669, 2004.

[29] K. Novoselov, D. Jiang, F. Schedin, T. Booth, V. Khotkevich, S. Morozov, *et al.*, "Two-dimensional atomic crystals," *Proceedings of the National Academy of Sciences of the United States of America,* vol. 102, pp. 10451-10453, 2005.

[30] A. K. Geim and K. S. Novoselov, "The rise of graphene," *Nature materials,* vol. 6, pp. 183-191, 2007.

[31] M. J. Allen, V. C. Tung, and R. B. Kaner, "Honeycomb carbon: a review of graphene," *Chemical reviews,* vol. 110, pp. 132-145, 2009.

[32] S. Iijima, "Helical microtubules of graphitic carbon," *nature,* vol. 354, pp. 56-58, 1991.

[33] H. W. Kroto, J. R. Heath, S. C. O'Brien, R. F. Curl, and R. E. Smalley, "C 60: buckminsterfullerene," *Nature,* vol. 318, pp. 162-163, 1985.

[34] C. Soldano, A. Mahmood, and E. Dujardin, "Production, properties and potential of graphene," *Carbon,* vol. 48, pp. 2127-2150, 2010.

[35] H. P. Boehm, R. Setton, and E. Stumpp, "Nomenclature and terminology of graphite intercalation compounds (IUPAC Recommendations 1994)," *Pure and Applied Chemistry,* vol. 66, pp. 1893-1901, 1994.

[36] A. H. Palser, "Interlayer interactions in graphite and carbon nanotubes," *Physical Chemistry Chemical Physics,* vol. 1, pp. 4459-4464, 1999.

[37] T. Enoki, M. Endo, and M. Suzuki, *Graphite intercalation compounds and applications*: Oxford University Press, 2003.

[38] M. S. Dresselhaus and G. Dresselhaus, "Intercalation compounds of graphite," *Advances in Physics,* vol. 51, pp. 1-186, 2002.

[39] P. Delhaes, *Graphite and precursors* vol. 1: CRC Press, 2000.

[40] D. R. Dreyer, R. S. Ruoff, and C. W. Bielawski, "From conception to realization: an historial account of graphene and some perspectives for its future," *Angewandte Chemie International Edition,* vol. 49, pp. 9336-9344, 2010.

[41] H. Fernandez-Moran, "Single crystals of graphite and mica as specimen support for electron microscopy," *J Appl Phys,* vol. 31, p. 1844, 1960.

[42] A. Van Bommel, J. Crombeen, and A. Van Tooren, "LEED and Auger electron observations of the SiC (0001) surface," *Surface Science,* vol. 48, pp. 463-472, 1975.

[43] E. Fitzer, K.-H. Kochling, H. Boehm, and H. Marsh, "Recommended terminology for the description of carbon as a solid (IUPAC Recommendations 1995)," *Pure and Applied Chemistry,* vol. 67, pp. 473-506, 1995.

[44] T. W. Ebbesen and H. Hiura, "Graphene in 3-dimensions: Towards graphite origami," *Advanced Materials,* vol. 7, pp. 582-586, 1995.

[45] E. Dujardin, T. Thio, H. Lezec, and T. W. Ebbesen, "Fabrication of mesoscopic devices from graphite microdisks," *Applied Physics Letters,* vol. 79, pp. 2474-2476, 2001.

[46] A. Krishnan, E. Dujardin, M. Treacy, J. Hugdahl, S. Lynum, and T. Ebbesen, "Graphitic cones and the nucleation of curved carbon surfaces," *Nature,* vol. 388, pp. 451-454, 1997.

[47] X. Lu, H. Huang, N. Nemchuk, and R. S. Ruoff, "Patterning of highly oriented pyrolytic graphite by oxygen plasma etching," *Applied Physics Letters,* vol. 75, pp. 193-195, 1999.

[48] X. Lu, M. Yu, H. Huang, and R. S. Ruoff, "Tailoring graphite with the goal of achieving single sheets," *Nanotechnology,* vol. 10, p. 269, 1999.

[49] Y. Zhang, J. P. Small, W. V. Pontius, and P. Kim, "Fabrication and electric field dependent transport measurements of mesoscopic graphite devices," *arXiv preprint cond-mat/0410314,* 2004.

[50] K. S. Novoselov, A. K. Geim, S. Morozov, D. Jiang, Y. Zhang, S. a. Dubonos, *et al.*, "Electric field effect in atomically thin carbon films," *science,* vol. 306, pp. 666-669, 2004.

[51] D. A. Brownson and C. E. Banks, "The electrochemistry of CVD graphene: progress and prospects," *Physical Chemistry Chemical Physics,* vol. 14, pp. 8264-8281, 2012.

[52] L. Landau, "Zur Theorie der phasenumwandlungen II," *Phys. Z. Sowjetunion,* vol. 11, pp. 26-35, 1937.

[53] C. Berger, Z. Song, T. Li, X. Li, A. Y. Ogbazghi, R. Feng*, et al.*, "Ultrathin epitaxial graphite: 2D electron gas properties and a route toward graphene-based nanoelectronics," *The Journal of Physical Chemistry B,* vol. 108, pp. 19912-19916, 2004.

[54] P. W. Sutter, J.-I. Flege, and E. A. Sutter, "Epitaxial graphene on ruthenium," *Nature materials,* vol. 7, pp. 406-411, 2008.

[55] M. A. Meitl, Z.-T. Zhu, V. Kumar, K. J. Lee, X. Feng, Y. Y. Huang*, et al.*, "Transfer printing by kinetic control of adhesion to an elastomeric stamp," *Nature Materials,* vol. 5, pp. 33-38, 2006.

[56] A. Reina, X. Jia, J. Ho, D. Nezich, H. Son, V. Bulovic*, et al.*, "Large area, few-layer graphene films on arbitrary substrates by chemical vapor deposition," *Nano letters,* vol. 9, pp. 30-35, 2008.

[57] Z. Shou-En, Y. Shengjun, and G. C. A. M. Janssen, "Optical transmittance of multilayer graphene," *EPL (Europhysics Letters),* vol. 108, p. 17007, 2014.

[58] L. Falkovsky, "Optical properties of graphene," in *Journal of Physics: Conference Series*, 2008, p. 012004.

[59] A. R. Ranjbartoreh, B. Wang, X. Shen, and G. Wang, "Advanced mechanical properties of graphene paper," *Journal of Applied Physics,* vol. 109, p. 014306, 2011.

[60] E. H. Hwang, S. Adam, and S. D. Sarma, "Carrier Transport in Two-Dimensional Graphene Layers," *Physical Review Letters,* vol. 98, p. 186806, 05/03/ 2007.

[61] P. Kumar, A. K. Singh, S. Hussain, K. N. Hui, K. San Hui, J. Eom*, et al.*, "Graphene: Synthesis, Properties and Application in Transparent Electronic Devices," *Reviews in Advanced Sciences and Engineering,* vol. 2, pp. 238-258, 2013.

[62] A. A. Balandin, S. Ghosh, W. Bao, I. Calizo, D. Teweldebrhan, F. Miao*, et al.*, "Superior thermal conductivity of single-layer graphene," *Nano letters,* vol. 8, pp. 902-907, 2008.

[63] A. Balandin, S. Ghosh, W. Bao, I. Calizo, D. Teweldebrhan, F. Miao*, et al.*, "Extremely high thermal conductivity of graphene: experimental study," *arXiv preprint arXiv:0802.1367,* 2008.

[64] K. S. Novoselov, V. Fal, L. Colombo, P. Gellert, M. Schwab, and K. Kim, "A roadmap for graphene," *Nature,* vol. 490, pp. 192-200, 2012.

[65] J. C. Meyer, A. K. Geim, M. Katsnelson, K. Novoselov, T. Booth, and S. Roth, "The structure of suspended graphene sheets," *Nature,* vol. 446, pp. 60-63, 2007.

[66] S. Stankovich, D. A. Dikin, G. H. Dommett, K. M. Kohlhaas, E. J. Zimney, E. A. Stach*, et al.*, "Graphene-based composite materials," *Nature,* vol. 442, pp. 282-286, 2006.

[67] S. Watcharotone, D. A. Dikin, S. Stankovich, R. Piner, I. Jung, G. H. Dommett*, et al.*, "Graphene-silica composite thin films as transparent conductors," *Nano Letters,* vol. 7, pp. 1888-1892, 2007.

[68] D. A. Dikin, S. Stankovich, E. J. Zimney, R. D. Piner, G. H. Dommett, G. Evmenenko*, et al.*, "Preparation and characterization of graphene oxide paper," *Nature,* vol. 448, pp. 457-460, 2007.

[69] K. S. Kim, Y. Zhao, H. Jang, S. Y. Lee, J. M. Kim, K. S. Kim*, et al.*, "Large-scale pattern growth of graphene films for stretchable transparent electrodes," *Nature,* vol. 457, pp. 706-710, 2009.

[70] S. Park and R. S. Ruoff, "Chemical methods for the production of graphenes," *Nature nanotechnology,* vol. 4, pp. 217-224, 2009.

[71] X. Li, W. Cai, J. An, S. Kim, J. Nah, D. Yang*, et al.*, "Large-area synthesis of high-quality and uniform graphene films on copper foils," *Science,* vol. 324, pp. 1312-1314, 2009.

[72] D. V. Kosynkin, A. L. Higginbotham, A. Sinitskii, J. R. Lomeda, A. Dimiev, B. K. Price*, et al.*, "Longitudinal unzipping of carbon nanotubes to form graphene nanoribbons," *Nature,* vol. 458, pp. 872-876, 2009.

[73] X. Li, C. W. Magnuson, A. Venugopal, J. An, J. W. Suk, B. Han*, et al.*, "Graphene films with large domain size by a two-step chemical vapor deposition process," *Nano letters,* vol. 10, pp. 4328-4334, 2010.

[74] M. H. Rümmeli, C. G. Rocha, F. Ortmann, I. Ibrahim, H. Sevincli, F. Börrnert*, et al.*, "Graphene: Piecing it together," *Advanced Materials,* vol. 23, pp. 4471-4490, 2011.

[75] M. T. Ghoneim, "Efficient Transfer of Graphene-Physical and Electrical Performance Perspective," King Abdullah University of Science and Technology, 2012.

[76] C. Mattevi, H. Kim, and M. Chhowalla, "A review of chemical vapour deposition of graphene on copper," *Journal of Materials Chemistry,* vol. 21, pp. 3324-3334, 2011.

[77] X. Li, W. Cai, I. H. Jung, J. H. An, D. Yang, A. Velamakanni*, et al.*, "Synthesis, characterization, and properties of large-area graphene films," *ECS Transactions,* vol. 19, pp. 41-52, 2009.

[78] W. Li, C. Tan, M. A. Lowe, H. D. Abruna, and D. C. Ralph, "Electrochemistry of individual monolayer graphene sheets," *ACS nano,* vol. 5, pp. 2264-2270, 2011.

[79] X. Li, Y. Zhu, W. Cai, M. Borysiak, B. Han, D. Chen*, et al.*, "Transfer of large-area graphene films for high-performance transparent conductive electrodes," *Nano letters,* vol. 9, pp. 4359-4363, 2009.

[80] D. A. Brownson and C. E. Banks, "Graphene electrochemistry: an overview of potential applications," *Analyst,* vol. 135, pp. 2768-2778, 2010.

[81] G. G. Wallace, J. Chen, D. Li, S. E. Moulton, and J. M. Razal, "Nanostructured carbon electrodes," *Journal of Materials Chemistry,* vol. 20, pp. 3553-3562, 2010.

[82] J. F. Dayen, A. Mahmood, D. S. Golubev, I. Roch-Jeune, P. Salles, and E. Dujardin, "Side-Gated Transport in Focused-Ion-Beam-Fabricated Multilayered Graphene Nanoribbons," *Small,* vol. 4, pp. 716-720, 2008.

[83] Y. Zhang and S. Tadigadapa, "Thermal characterization of liquids and polymer thin films using a microcalorimeter," *Applied Physics Letters,* vol. 86, p. 034101, 2005.

[84] J.-H. Chen, C. Jang, S. Xiao, M. Ishigami, and M. S. Fuhrer, "Intrinsic and extrinsic performance limits of graphene devices on SiO2," *Nature nanotechnology,* vol. 3, pp. 206-209, 2008.

[85] K. I. Bolotin, K. Sikes, Z. Jiang, M. Klima, G. Fudenberg, J. Hone*, et al.*, "Ultrahigh electron mobility in suspended graphene," *Solid State Communications,* vol. 146, pp. 351-355, 2008.

[86] A. N. Sidorov, M. M. Yazdanpanah, R. Jalilian, P. Ouseph, R. W. Cohn, and G. Sumanasekera, "Electrostatic deposition of graphene," *Nanotechnology,* vol. 18, p. 135301, 2007.

[87] A. Shukla, R. Kumar, J. Mazher, and A. Balan, "Graphene made easy: High quality, large-area samples," *Solid State Communications,* vol. 149, pp. 718-721, 2009.

[88] J. Hass, W. De Heer, and E. Conrad, "The growth and morphology of epitaxial multilayer graphene," *Journal of Physics: Condensed Matter,* vol. 20, p. 323202, 2008.

[89] W. A. De Heer, C. Berger, X. Wu, P. N. First, E. H. Conrad, X. Li, *et al.*, "Epitaxial graphene," *Solid State Communications,* vol. 143, pp. 92-100, 2007.

[90] C. Berger, Z. Song, X. Li, X. Wu, N. Brown, C. Naud, *et al.*, "Electronic confinement and coherence in patterned epitaxial graphene," *Science,* vol. 312, pp. 1191-1196, 2006.

[91] C. Berger, X. Wu, P. N. First, E. H. Conrad, X. Li, M. Sprinkle*, et al.*, "Dirac particles in epitaxial graphene films grown on SiC," in *Advances in Solid State Physics,* ed: Springer, 2008, pp. 145-157.

[92] C. Berger, Z. Song, X. Li, X. Wu, N. Brown, D. Maud*, et al.*, "Phys. Status Solidi A: Appl," *Mater. Sci,* vol. 204, p. 1746, 2007.

[93] T. Aizawa, R. Souda, S. Otani, Y. Ishizawa, and C. Oshima, "Bond softening in monolayer graphite formed on transition-metal carbide surfaces," *Physical Review B,* vol. 42, p. 11469, 1990.

[94] M. Terai, N. Hasegawa, M. Okusawa, S. Otani, and C. Oshima, "Electronic states of monolayer micrographite on TiC (111)-faceted and TiC (410) surfaces," *Applied surface science,* vol. 130, pp. 876-882, 1998.

[95] B. Itchkawitz, P. Lyman, G. Ownby, and D. Zehner, "Monolayer graphite on TaC (111): electronic band structure," *Surface science,* vol. 318, pp. 395-402, 1994.

[96] A. Nagashima, H. Itoh, T. Ichinokawa, C. Oshima, and S. Otani, "Change in the electronic states of graphite overlayers depending on thickness," *Physical Review B,* vol. 50, p. 4756, 1994.

[97] M. H. Rummeli, C. G. Rocha, F. Ortmann, I. Ibrahim, H. Sevincli, F. Borrnert, *et al.*, "Graphene: Piecing it together," *Adv Mater,* vol. 23, pp. 4471-90, Oct 18 2011.

[98] X.-m. Chen, G.-h. Wu, Y.-q. Jiang, Y.-r. Wang, and X. Chen, "Graphene and graphene-based nanomaterials: the promising materials for bright future of electroanalytical chemistry," *Analyst,* vol. 136, pp. 4631-4640, 2011.

[99] X. Li, W. Cai, L. Colombo, and R. S. Ruoff, "Evolution of graphene growth on Ni and Cu by carbon isotope labeling," *Nano letters,* vol. 9, pp. 4268-4272, 2009.

[100] R. A. Barton, J. Parpia, and H. G. Craighead, "Fabrication and performance of graphene nanoelectromechanical systems," *Journal of Vacuum Science & Technology B,* vol. 29, p. 050801, 2011.

[101] F. Himpsel, K. Christmann, P. Heimann, D. Eastman, and P. J. Feibelman, "Adsorbate band dispersions for C on Ru (0001)," *Surface Science Letters,* vol. 115, pp. L159-L164, 1982.

[102] N. Kholin, E. Rut'kov, and A. Y. Tontegode, "The nature of the adsorption bond between graphite islands and iridium surface," *Surface science,* vol. 139, pp. 155-172, 1984.

[103] J. Coraux, A. T. N'Diaye, C. Busse, and T. Michely, "Structural coherency of graphene on Ir (111)," *Nano letters,* vol. 8, pp. 565-570, 2008.

[104] K. S. Novoselov, Z. Jiang, Y. Zhang, S. Morozov, H. Stormer, U. Zeitler, *et al.*, "Room-temperature quantum Hall effect in graphene," *Science,* vol. 315, pp. 1379-1379, 2007.

[105] M. Eizenberg and J. Blakely, "Carbon monolayer phase condensation on Ni (111)," *Surface Science,* vol. 82, pp. 228-236, 1979.

[106] A. Obraztsov, E. Obraztsova, A. Tyurnina, and A. Zolotukhin, "Chemical vapor deposition of thin graphite films of nanometer thickness," *Carbon,* vol. 45, pp. 2017-2021, 2007.

[107] Q. Yu, J. Lian, S. Siriponglert, H. Li, Y. P. Chen, and S.-S. Pei, "Graphene segregated on Ni surfaces and transferred to insulators," *Applied Physics Letters,* vol. 93, p. 113103, 2008.

[108] S.-Y. Kwon, C. V. Ciobanu, V. Petrova, V. B. Shenoy, J. Bareno, V. Gambin, *et al.*, "Growth of semiconducting graphene on palladium," *Nano letters,* vol. 9, pp. 3985-3990, 2009.

[109] J. Hamilton and J. Blakely, "Carbon segregation to single crystal surfaces of Pt, Pd and Co," *Surface Science,* vol. 91, pp. 199-217, 1980.

[110] T. Land, T. Michely, R. Behm, J. Hemminger, and G. Comsa, "STM investigation of single layer graphite structures produced on Pt (111) by hydrocarbon decomposition," *Surface Science,* vol. 264, pp. 261-270, 1992.

[111] N. Gall, S. Mikhailov, E. Rut'kov, and A. Y. Tontegode, "Carbon interaction with the rhenium surface," *Surface science,* vol. 191, pp. 185-202, 1987.

[112] H. Zi-Pu, D. Ogletree, M. Van Hove, and G. Somorjai, "LEED theory for incommensurate overlayers: Application to graphite on Pt (111)," *Surface Science,* vol. 180, pp. 433-459, 1987.

[113] W. J. Arnoult and R. B. McLellan, "The solubility of carbon in rhodium ruthenium, iridium and rhenium," *Scripta Metallurgica,* vol. 6, pp. 1013-1018, 1972.

[114] J. McCleverty, "Chemistry of the first-row transition metals," *Oxford Chemistry Primers,* vol. 71, pp. ALL-ALL, 1999.

[115] A. Reina, X. T. Jia, J. Ho, D. Nezich, H. B. Son, V. Bulovic, *et al.*, "Large area, few-layer graphene films on arbitrary substrates by chemical vapor deposition," *Nano Letters,* vol. 9, pp. 30–35, 2009.

[116] M. J. Allen, V. C. Tung, and R. B. Kaner, "Honeycomb carbon: a review of graphene," *Chemical reviews,* vol. 110, pp. 132-145.

[117] C. Mattevi, H. Kima, and M. Chhowall, "A review of chemical vapour deposition of graphene on copper," *J. Mater. Chem.*, vol. 21, pp. 3324–3334, 2011.

[118] W. Regan, N. Alem, B. Alemán, B. Geng, Ç. Girit, L. Maserati, *et al.,* "A direct transfer of layer-area graphene," *APPLIED PHYSICS LETTERS* vol. 96, p. 113102, 2010.

[119] X. Li, W. Cai, J. An, S. Kim, J. Nah, D. Yang, *et al.*, "Large-area synthesis of high-quality and uniform graphene films on copper foils," *Science,* vol. 324, pp. 1312-1314, 2009.

[120] S. Bae, H. Kim, Y. Lee, X. Xu, J.-S. Park, Y. Zheng, *et al.*, *Nat. Nanotechnol.,* vol. 5, p. 574, 2010.

[121] C. S. R.-V. M. P. Levendorf, S. Garg and J. Park, *Nano Lett.,* vol. 9, p. 4479, 2009.

[122] A. Ismach, C. Druzgalski, S. Penwell, A. Schwartzberg, M. Zheng, A. Javey, *et al.*, *Nano Lett,* vol. 10, p. 1542, 2010.

[123] Y.-H. Lee and J.-H. Lee, *Appl. Phys. Lett.*, vol. 96, p. 083101, 2010.

[124] Y. Lee, S. Bae, H. Jang, S. Jang, S.-E. Zhu, S. H. Sim, *et al.*, *Nano Lett.*, vol. 10, p. 490, 2010.

[125] A. Srivastava, C. Galande, L. Ci, L. Song, C. Rai, D. Jariwala, *et al.*, *Chem. Mater.*, vol. 22, p. 3457, 2010.

[126] H. Cao, Q. Yu, L. A. Jauregui, J. Tian, W. Wu, Z. Liu, *et al.*, *Appl. Phys. Lett.* , vol. 96, p. 122106, 2010.

[127] V. P. Verma, S. Das, I. Lahiri, and W. Choi, *Appl. Phys. Lett.*, vol. 96, p. 203108, 2010.

[128] M. H. Rummel, C. G. Rocha, F. Ortmann, I. Ibrahim, H. Sevincli, F. Borrnert, *et al.*, *Adv. Mater.*, vol. 23, p. 4471, 2011.

[129] X. Li, W. Cai, L. Colombo, and R. S. Ruoff, *Nano Lett.*, vol. 9, p. 4268, 2009.

[130] W. Cai, Y. Zhu, X. Li, R. D. Piner, and R. S. Ruoff, *Appl. Phys. Lett.*, vol. 95, p. 123115, 2009.

[131] M. P. Levendorf, C. S. Ruiz-Vargas, S. Garg, and J. Park, *Nano Lett.*, vol. 9, p. 4479, 2009.

[132] A. Guermoune, T. Chari, F. Popescu, S. S. Sabri, J. Guillemette, H. S. Skulason, *et al.*, *Carbon,* vol. 49, p. 4204, 2011.

[133] D. A. C. Brownson and C. E. Banks, "The electrochemistry of CVD graphene: progress and prospects," *Phys. Chem. Chem. Phys.,* vol. 14, pp. 8264 - 8281, 2012.

[134] X. Li, C. W. Magnuson, A. Venugopal, R. M. Tromp, J. B. Hannon, E. M. Vogel, *et al.*, *J. Am. Chem. Soc.*, vol. 133, p. 2816, 2011.

[135] K. Kim, Z. Lee, W. Regan, C. Kisielowski, M. F. Crommie, and A. Zettl, *ACS Nano,* vol. 5, p. 2142, 2011.

[136] C. S. Ruiz-Vargas, H. L. Zhuang, P. Y. Huang, A. M. van-der-Zande, S. Garg, P. L. McEuen, *et al.*, *Nano Lett.,* vol. 11, p. 2259, 2011.

[137] H. C. L. A. Jauregui, W. Wu, Q. Yu and Y. P. Chen, *Solid State Commun.*, vol. 151, p. 1100, 2011.

[138] Y. Zhang, L. Gomez, F. N. Ishikawa, A. Madaria, K. Ryu, C. Wang, *et al.*, *J. Phys. Chem. Lett.*, vol. 1, p. 3101, 2010.

[139] A. N. Obraztsov, E. A. Obraztsova, A. V. Tyurnina, and A. A. Zolotukhin, *Carbon,* vol. 45, p. 2017, 2007.

[140] M. Z. Butt, *J. Mater. Sci. Lett.,* vol. 2, p. 1, 1983.

[141] Y. N. Z. Trehan and Z. Anorg, *Allg. Chem.*, vol. 318, p. 107, 1962.

[142] K. L. Chavez and D. W. J. Hess, *J. Electrochem. Soc.,* vol. 148, p. G640, 2001.

[143] S. Park and R. S. Ruoff, "Chemical methods for the production of graphenes," *Nat Nanotechnol,* vol. 4, pp. 217–224, 2009.

[144] B. BC., "On the atomic weight of graphite," *Philos Trans Roy Soc London,* vol. 149, pp. 249-259, 1859.

[145] L. Babiano, "Graphitic acid," *Ann Chim Appl,* vol. 4, pp. 231-245, 1915.

[146] C. Soldano, A. Mahmood, and E. Dujardin, "Production, properties and potential of graphene," *Carbon* vol. 48, pp. 2127-2150, 2010.

[147] W. S. Hummers and R. E. Offeman, "Preparation of graphitic oxide," *J Am Chem Soc*, vol. 80, p. 1339, 1958.

[148] S. Duquesne, M. Le Bras, S. Bourbigot, R. Delobel, H. Vezin, V. Camino, *et al.*, "Expandable graphite: a fire retardant additive for polyurethane coatings," *Fire Mater*, vol. 27, pp. 103-117, 2003.

[149] F. Kang, T. Y. Zhang, and Y. Leng, "Electrochemical behavior of graphite in electrolyte of sulfuric and acetic acid," *Carbon*, vol. 35, pp. 1167–1173, 1997.

[150] H. P. Boehm, A. Clauss, U. Hofmann, and G. O. Fischer, "Dunnste Kohlenstoff-Folien " *Zeitschrift Fur Naturforschung Part B –Chemie Biochemie Biophysik Biologie Und Verwandten Gebiete*, vol. B17, p. 150, 1962.

[151] H. C. Schniepp, J.-L. Li, M. J. McAllister, H. Sai, M. Herrera-Alonso, D. H. Adamson, *et al.*, "Functionalized single graphene sheets derived from splitting graphite oxide," *J Phys Chem B*, vol. 110, pp. 8535-8539, 2006.

[152] M. J. McAllister, J. L. Li, D. H. Adamson, H. C. Schniepp, A. A. Abdala, J. Liu, *et al.*, "Single sheet functionalized graphene by oxidation and thermal expansion of graphite," *Chem Mater*, vol. 19, pp. 4396-4404, 2007.

[153] M. Endo, *Graphite intercalation compounds and applications*: Oxford University Press, 2003.

[154] X. L. Li, X. R. Wang, L. Zhang, S. W. Lee, and H. J. Dai, *Science,* vol. 319, p. 1229., 2008.

[155] L. M. Viculis, J. J. Mack, and R. B. Kaner, *Science* vol. 299, p. 1361, 2003.

[156] L. M. Viculis, J. J. Mack, O. M. Mayer, H. T. Hahn, and R. B. Kaner, *J. Mater. Chem.* , vol. 15, p. 974, 2005.

[157] S. Stankovich, D. A. Dikin, G. H. B. Dommett, K. M. Kohlhaas, E. J. Zimney, E. A. Stach, *et al.*, *Nature* vol. 442, p. 282, 2006.

[158] S. Stankovich, D. A. Dikin, R. D. Piner, K. A. Kohlhaas, A. Kleinhammes, Y. Jia, *et al.*, *Carbon* vol. 45, p. 1558, 2007.

[159] H.-K. Jeong, Y. P. Lee, R. J. W. E. Lahaye, M.-H. Park, K. H. An, I. J. Kim, *et al.*, *J. Am. Chem. Soc.* , vol. 130, p. 1362, 2008.

[160] M. Lotya, P. J. King, U. Khan, S. De, and J. N. Coleman, *ACS Nano,* vol. 4, p. 3155, 2010.

[161] M. Lotya, Y. Hernandez, P. J. King, R. J. Smith, V. Nicolos, L. S. Karlsson, *et al.*, *J. Am. Chem. Soc.,* vol. 131, p. 3611, 2009.

[162] W. Regan, N. Alem, B. Alemán, B. Geng, Ç. Girit, L. Maserati, *et al.*, "A direct transfer of layer-area graphene," *Applied Physics Letters*, vol. 96, p. 113102, 2010.

[163] S. Bae, H. Kim, Y. Lee, X. Xu, J.-S. Park, Y. Zheng, *et al.*, "Roll-to-roll production of 30-inch graphene films for transparent electrodes," *Nature nanotechnology,* vol. 5, pp. 574-578, 2010.

[164] B. Alemán, W. Regan, S. Aloni, V. Altoe, N. Alem, C. l. Girit, *et al.*, "Transfer-free batch fabrication of large-area suspended graphene membranes," *ACS nano,* vol. 4, pp. 4762-4768, 2010.

[165] Y. Lee, S. Bae, H. Jang, S. Jang, S.-E. Zhu, S. H. Sim, *et al.*, "Wafer-scale synthesis and transfer of graphene films," *Nano letters,* vol. 10, pp. 490-493, 2010.

[166] E. Saubestre, "Copper etching in ferric chloride," *Industrial & Engineering Chemistry,* vol. 51, pp. 288-290, 1959.

[167] Y.-H. Lee and J.-H. Lee, "Scalable growth of free-standing graphene wafers with copper (Cu) catalyst on SiO2/Si substrate: Thermal conductivity of the wafers," *Applied Physics Letters,* vol. 96, p. 083101, 2010.

[168] A. Srivastava, C. Galande, L. Ci, L. Song, C. Rai, D. Jariwala, *et al.*, "Novel liquid precursor-based facile synthesis of large-area continuous, single, and few-layer graphene films," *Chemistry of Materials,* vol. 22, pp. 3457-3461, 2010.

[169] S. Habu and Y. Yoshihiro, "Studies of copper etching in ferric chloride solutions," *Industrial & Engineering Chemistry Process Design and Development,* vol. 21, pp. 511-514, 1982.

[170] A. Ismach, C. Druzgalski, S. Penwell, A. Schwartzberg, M. Zheng, A. Javey, *et al.*, "Direct chemical vapor deposition of graphene on dielectric surfaces," *Nano letters,* vol. 10, pp. 1542-1548, 2010.

[171] L.-H. Liu and M. Yan, "Simple method for the covalent immobilization of graphene," *Nano letters,* vol. 9, pp. 3375-3378, 2009.

[172] H. A. Becerril, J. Mao, Z. Liu, R. M. Stoltenberg, Z. Bao, and Y. Chen, "Evaluation of solution-processed reduced graphene oxide films as transparent conductors," *ACS nano,* vol. 2, pp. 463-470, 2008.

[173] J. C. Meyer, C. O. Girit, M. Crommie, and A. Zettl, "Imaging and dynamics of light atoms and molecules on graphene," *Nature,* vol. 454, pp. 319-322, 2008.

[174] P. Blake, E. Hill, A. C. Neto, K. Novoselov, D. Jiang, R. Yang, *et al.*, "Making graphene visible," *Applied Physics Letters,* vol. 91, p. 063124, 2007.

[175] L. Gao, W. Ren, F. Li, and H.-M. Cheng, "Total color difference for rapid and accurate identification of graphene," *ACS nano,* vol. 2, pp. 1625-1633, 2008.

[176] S. Akcöltekin, M. El Kharrazi, B. Köhler, A. Lorke, and M. Schleberger, "Graphene on insulating crystalline substrates," *Nanotechnology,* vol. 20, p. 155601, 2009.

[177] Y. Zhang, J. P. Small, M. E. Amori, and P. Kim, "Electric field modulation of galvanomagnetic properties of mesoscopic graphite," *Physical review letters,* vol. 94, p. 176803, 2005.

[178] J. C. Meyer, C. Kisielowski, R. Erni, M. D. Rossell, M. Crommie, and A. Zettl, "Direct imaging of lattice atoms and topological defects in graphene membranes," *Nano letters,* vol. 8, pp. 3582-3586, 2008.

[179] A. Hashimoto, K. Suenaga, A. Gloter, K. Urita, and S. Iijima, "Direct evidence for atomic defects in graphene layers," *Nature,* vol. 430, pp. 870-873, 2004.

[180] Y. Hernandez, V. Nicolosi, M. Lotya, F. M. Blighe, Z. Sun, S. De, *et al.*, "High-yield production of graphene by liquid-phase exfoliation of graphite," *Nature nanotechnology,* vol. 3, pp. 563-568, 2008.

[181] S. Horiuchi, T. Gotou, M. Fujiwara, R. Sotoaka, M. Hirata, K. Kimoto, *et al.*, "Carbon nanofilm with a new structure and property," *Japanese journal of applied physics,* vol. 42, p. L1073, 2003.

[182] A. Damascelli, Z. Hussain, and Z.-X. Shen, "Angle-resolved photoemission studies of the cuprate superconductors," *Reviews of modern physics,* vol. 75, p. 473, 2003.

[183] S. Zhou, G.-H. Gweon, J. Graf, A. Fedorov, C. Spataru, R. Diehl, *et al.*, "First direct observation of Dirac fermions in graphite," *Nature physics,* vol. 2, pp. 595-599, 2006.

[184] T. Ohta, A. Bostwick, T. Seyller, K. Horn, and E. Rotenberg, "Controlling the electronic structure of bilayer graphene," *Science,* vol. 313, pp. 951-954, 2006.

[185] A. Ferrari, J. Meyer, V. Scardaci, C. Casiraghi, M. Lazzeri, F. Mauri, *et al.*, "Raman spectrum of graphene and graphene layers," *Physical review letters,* vol. 97, p. 187401, 2006.

[186] A. C. Ferrari, "Raman spectroscopy of graphene and graphite: disorder, electron–phonon coupling, doping and nonadiabatic effects," *Solid state communications,* vol. 143, pp. 47-57, 2007.

[187] L. Malard, M. Pimenta, G. Dresselhaus, and M. Dresselhaus, "Raman spectroscopy in graphene," *Physics Reports,* vol. 473, pp. 51-87, 2009.

[188] C. Thomsen and S. Reich, "Double resonant Raman scattering in graphite," *Physical Review Letters,* vol. 85, p. 5214, 2000.

[189] C. Faugeras, A. Nerrière, M. Potemski, A. Mahmood, E. Dujardin, C. Berger, *et al.*, "Few-layer graphene on SiC, pyrolitic graphite, and graphene: A Raman scattering study," *Applied Physics Letters,* vol. 92, p. 011914, 2008.

[190] I. Calizo, A. Balandin, W. Bao, F. Miao, and C. Lau, "Temperature dependence of the Raman spectra of graphene and graphene multilayers," *Nano letters,* vol. 7, pp. 2645-2649, 2007.

[191] C. Casiraghi, A. Hartschuh, E. Lidorikis, H. Qian, H. Harutyunyan, T. Gokus, *et al.*, "Rayleigh imaging of graphene and graphene layers," *Nano letters,* vol. 7, pp. 2711-2717, 2007.

[192] I. P. Batra, N. Garcia, H. Rohrer, H. Salemink, E. Stoll, and S. Ciraci, "A study of graphite surface with stm and electronic structure calculations," *Surface Science,* vol. 181, pp. 126-138, 1987.

[193] J. P. Rabe and S. Buchholz, "Commensurability and mobility in two-dimensional molecular patterns on graphite," *Science,* vol. 253, pp. 424-427, 1991.

[194] J. Soler, A. Baro, N. García, and H. Rohrer, "Interatomic forces in scanning tunneling microscopy: giant corrugations of the graphite surface," in *Scanning Tunneling Microscopy*, ed: Springer, 1993, pp. 172-175.

[195] E. Stolyarova, K. T. Rim, S. Ryu, J. Maultzsch, P. Kim, L. E. Brus*, et al.*, "High-resolution scanning tunneling microscopy imaging of mesoscopic graphene sheets on an insulating surface," *Proceedings of the National Academy of Sciences,* vol. 104, pp. 9209-9212, 2007.

[196] L. A. Ponomarenko, F. Schedin, M. I. Katsnelson, R. Yang, E. W. Hill, K. S. Novoselov*, et al.*, "Chaotic Dirac Billiard in Graphene Quantum Dots," *Science,* vol. 320, pp. 356-358, April 18, 2008 2008.

[197] G. Lalwani, A. M. Henslee, B. Farshid, L. Lin, F. K. Kasper, Y.-X. Qin*, et al.*, "Two-Dimensional Nanostructure- Reinforced Biodegradable Polymeric Nanocomposites for Bone Tissue Engineering," *Biomacromolecules,* vol. 14, pp. 900-909, 02/27 2013.

[198] R. Tkacz, R. Oldenbourg, S. B. Mehta, M. Miansari, A. Verma, and M. Majumder, "pH dependent isotropic to nematic phase transitions in graphene oxide dispersions reveal droplet liquid crystalline phases," *Chemical Communications,* vol. 50, pp. 6668-6671, 2014.

[199] J. Hedberg. (2013, Graphene-Based Solar Cells Could Yield 60% Efficiency.

[200] S. Hu, M. Lozada-Hidalgo, F. C. Wang, A. Mishchenko, F. Schedin, R. R. Nair, *et al.*, "Proton transport through one-atom-thick crystals," *Nature*, vol. 516, pp. 227-230, 12/11/print 2014.

[201] Z. Peng, J. Lin, R. Ye, E. L. G. Samuel, and J. M. Tour, "Flexible and Stackable Laser-Induced Graphene Supercapacitors," *ACS Applied Materials & Interfaces*, vol. 7, pp. 3414-3419, 2015/02/11 2015.

[202] S. Zhu and T. Li, "Hydrogenation-Assisted Graphene Origami and Its Application in Programmable Molecular Mass Uptake, Storage, and Release," *ACS Nano*, vol. 8, pp. 2864-2872, 2014/03/25 2014.

[203] M. Andronico, "5 Ways Graphene Will Change Gadgets Forever," in *Laptop*, ed. Laptop: Laptop, 2014.

[204] S. C. O'Hern, M. S. H. Boutilier, J.-C. Idrobo, Y. Song, J. Kong, T. Laoui, *et al.*, "Selective Ionic Transport through Tunable Subnanometer Pores in Single-Layer Graphene Membranes," *Nano Letters*, vol. 14, pp. 1234-1241, 2014/03/12 2014.

[205] D.-e. Jiang, V. R. Cooper, and S. Dai, "Porous graphene as the ultimate membrane for gas separation," *Nano letters*, vol. 9, pp. 4019-4024, 2009.

[206] M. E. Suk and N. Aluru, "Water transport through ultrathin graphene," *The Journal of Physical Chemistry Letters*, vol. 1, pp. 1590-1594, 2010.

[207] S. Garaj, W. Hubbard, A. Reina, J. Kong, D. Branton, and J. Golovchenko, "Graphene as a subnanometre trans-electrode membrane," *Nature*, vol. 467, pp. 190-193, 2010.

[208] C. A. Merchant, K. Healy, M. Wanunu, V. Ray, N. Peterman, J. Bartel, *et al.*, "DNA translocation through graphene nanopores," *Nano letters*, vol. 10, pp. 2915-2921, 2010.

[209] G. F. Schneider, S. W. Kowalczyk, V. E. Calado, G. Pandraud, H. W. Zandbergen, L. M. Vandersypen, *et al.*, "DNA translocation through graphene nanopores," *Nano letters*, vol. 10, pp. 3163-3167, 2010.

[210] Z.-M. Huang, Y. Z. Zhang, M. Kotaki, and S. Ramakrishna, "A review on polymer nanofibers by electrospinning and their applications in nanocomposites," *Composites Science and Technology*, vol. 63, pp. 2223-2253, 11// 2003.

[211] L. Yao, T. W. Haas, A. Guiseppi-Elie, G. L. Bowlin, D. G. Simpson, and G. E. Wnek, "Electrospinning and stabilization of fully hydrolyzed poly (vinyl alcohol) fibers," *Chemistry of Materials*, vol. 15, pp. 1860-1864, 2003.

[212] A. Greiner and J. H. Wendorff, "Electrospinning: a fascinating method for the preparation of ultrathin fibers," *Angew Chem Int Ed Engl,* vol. 46, pp. 5670-703, 2007.

[213] Y. Shin, M. Hohman, M. Brenner, and G. Rutledge, "Electrospinning: A whipping fluid jet generates submicron polymer fibers," *Applied Physics Letters,* vol. 78, pp. 1149-1151, 2001.

[214] G. C. Rutledge and S. V. Fridrikh, "Formation of fibers by electrospinning," *Advanced Drug Delivery Reviews,* vol. 59, pp. 1384-1391, 2007.

[215] H. Wu and W. Pan, "Preparation of zinc oxide nanofibers by electrospinning," *Journal of the American Ceramic Society,* vol. 89, pp. 699-701, 2006.

[216] W. Wang, H. Huang, Z. Li, H. Zhang, Y. Wang, W. Zheng*, et al.*, "Zinc oxide nanofiber gas sensors via electrospinning," *Journal of the American Ceramic Society,* vol. 91, pp. 3817-3819, 2008.

[217] H. Wu, R. Zhang, X. Liu, D. Lin, and W. Pan, "Electrospinning of Fe, Co, and Ni nanofibers: synthesis, assembly, and magnetic properties," *Chemistry of materials,* vol. 19, pp. 3506-3511, 2007.

[218] D. Li and Y. Xia, "Direct fabrication of composite and ceramic hollow nanofibers by electrospinning," *Nano Letters,* vol. 4, pp. 933-938, 2004.

[219] R. Ramaseshan, S. Sundarrajan, R. Jose, and S. Ramakrishna, "Nanostructured ceramics by electrospinning," *Journal of Applied Physics,* vol. 102, p. 111101, 2007.

[220] W. Sigmund, J. Yuh, H. Park, V. Maneeratana, G. Pyrgiotakis, A. Daga*, et al.*, "Processing and structure relationships in electrospinning of ceramic fiber systems," *Journal of the American Ceramic Society,* vol. 89, pp. 395-407, 2006.

[221] D. Li, Y. Wang, and Y. Xia, "Electrospinning of polymeric and ceramic nanofibers as uniaxially aligned arrays," *Nano letters,* vol. 3, pp. 1167-1171, 2003.

[222] D. Li, J. T. McCann, Y. Xia, and M. Marquez, "Electrospinning: a simple and versatile technique for producing ceramic nanofibers and nanotubes," *Journal of the American Ceramic Society,* vol. 89, pp. 1861-1869, 2006.

[223] P. Dayal, J. Liu, S. Kumar, and T. Kyu, "Experimental and theoretical investigations of porous structure formation in electrospun fibers," *Macromolecules,* vol. 40, pp. 7689-7694, 2007.

[224] S. Agarwal, A. Greiner, and J. H. Wendorff, "Functional materials by electrospinning of polymers," *Progress in Polymer Science,* vol. 38, pp. 963-991, 2013.

[225] X. Yuan, Y. Zhang, C. Dong, and J. Sheng, "Morphology of ultrafine polysulfone fibers prepared by electrospinning," *Polymer International,* vol. 53, pp. 1704-1710, 2004.

[226] S. Ramakrishna, K. Fujihara, W.-E. Teo, T.-C. Lim, and Z. Ma, *An introduction to electrospinning and nanofibers* vol. 90: World Scientific, 2005.

[227] A. Greiner and J. H. Wendorff, "Electrospinning: a fascinating method for the preparation of ultrathin fibers," *Angewandte Chemie International Edition,* vol. 46, pp. 5670-5703, 2007.

[228] C. Thompson, G. Chase, A. Yarin, and D. Reneker, "Effects of parameters on nanofiber diameter determined from electrospinning model," *Polymer,* vol. 48, pp. 6913-6922, 2007.

[229] A. Ferrari, J. Meyer, V. Scardaci, C. Casiraghi, M. Lazzeri, F. Mauri*, et al.*, "The Raman fingerprint of graphene," *arXiv preprint cond-mat/0606284,* 2006.

[230] Z. Ni, Y. Wang, T. Yu, and Z. Shen, "Raman spectroscopy and imaging of graphene," *Nano Research,* vol. 1, pp. 273-291, 2008.

[231] R. Jalili, S. A. Hosseini, and M. Morshed, "The effects of operating parameters on the morphology of electrospun polyacrilonitrile nanofibres," *Iranian Polymer Journal,* vol. 14, p. 1074, 2005.

[232] K. Jun, O. Reid, Y. Yanou, C. David, M. Robert, W. C. Geoffrey*, et al.*, "A scanning tip electrospinning source for deposition of oriented nanofibres," *Nanotechnology,* vol. 14, p. 1124, 2003.

[233] S. Dhakate, B. Singla, M. Uppal, and R. Mathur, "Effect of processing parameters on morphology and thermal properties of electrospun polycarbonate nanofibers," *Advanced Materials Letters,* vol. 1, pp. 200-204, 2010.

[234] K.-H. Chang and H.-L. Lin, "Electrospin of polysulfone in N,N'-dimethyl acetamide solutions," *Journal of Polymer Research,* vol. 16, pp. 611-622, 2009/11/01 2009.

[235] M. M. Demir, I. Yilgor, E. Yilgor, and B. Erman, "Electrospinning of polyurethane fibers," *Polymer,* vol. 43, pp. 3303-3309, 5// 2002.

[236] H. Fong, I. Chun, and D. Reneker, "Beaded nanofibers formed during electrospinning," *Polymer,* vol. 40, pp. 4585-4592, 1999.

[237] L. Larrondo and R. St John Manley, "Electrostatic fiber spinning from polymer melts. I. Experimental observations on fiber formation and properties," *Journal of Polymer Science: Polymer Physics Edition,* vol. 19, pp. 909-920, 1981.

[238] P. Heikkilä and A. Harlin, "Parameter study of electrospinning of polyamide-6," *European Polymer Journal,* vol. 44, pp. 3067-3079, 2008.

[239] M. Chowdhury and G. Stylios, "Effect of experimental parameters on the morphology of electrospun Nylon 6 fibres," *International Journal of Basic & Applied Sciences,* vol. 10, pp. 116-131, 2010.

[240] V. Beachley and X. Wen, "Effect of electrospinning parameters on the nanofiber diameter and length," *Materials Science and Engineering: C,* vol. 29, pp. 663-668, 2009.

[241] V. Beachley and X. Wen, "Polymer nanofibrous structures: Fabrication, biofunctionalization, and cell interactions," *Progress in polymer science,* vol. 35, pp. 868-892, 2010.

[242] P. K. Baumgarten, "Electrostatic spinning of acrylic microfibers," *Journal of colloid and interface science,* vol. 36, pp. 71-79, 1971.

[243] S. Megelski, J. S. Stephens, D. B. Chase, and J. F. Rabolt, "Micro-and nanostructured surface morphology on electrospun polymer fibers," *Macromolecules,* vol. 35, pp. 8456-8466, 2002.

[244] J. Sutasinpromprae, S. Jitjaicham, M. Nithitanakul, C. Meechaisue, and P. Supaphol, "Preparation and characterization of ultrafine electrospun polyacrylonitrile fibers and their subsequent pyrolysis to carbon fibers," *Polymer International,* vol. 55, pp. 825-833, 2006.

[245] Q. Li, Z. Jia, Y. Yang, L. Wang, and G. Zhicheng, "Preparation and Properties of Poly (vinyl alcohol) Nanofibers by Electrospinning," in *International Conference on Solid Dielectrics*, Winchester, UK, 2007, pp. 215-218.

[246] C. Mit-uppatham, M. Nithitanakul, and P. Supaphol, "Effects of Solution Concentration, Emitting Electrode Polarity, Solvent Type, and Salt Addition on Electrospun Polyamide-6 Fibers: A Preliminary Report," in *Macromolecular Symposia*, 2004, pp. 293-300.

[247] P. Supaphol, C. Mit-Uppatham, and M. Nithitanakul, "Ultrafine electrospun polyamide-6 fibers: Effect of emitting electrode polarity on morphology and average fiber diameter," *Journal of Polymer Science Part B: Polymer Physics*, vol. 43, pp. 3699-3712, 2005.

[248] K. Morota, H. Matsumoto, T. Mizukoshi, Y. Konosu, M. Minagawa, A. Tanioka, *et al.*, "Poly (ethylene oxide) thin films produced by electrospray

deposition: morphology control and additive effects of alcohols on nanostructure," *Journal of colloid and interface science,* vol. 279, pp. 484-492, 2004.

[249] V. Pornsopone, P. Supaphol, R. Rangkupan, and S. Tantayanon, "Electrospinning of methacrylate-based copolymers: Effects of solution concentration and applied electrical potential on morphological appearance of as-spun fibers," *Polymer Engineering & Science,* vol. 45, pp. 1073-1080, 2005.

[250] C. Zhang, X. Yuan, L. Wu, Y. Han, and J. Sheng, "Study on morphology of electrospun poly (vinyl alcohol) mats," *European Polymer Journal,* vol. 41, pp. 423-432, 2005.

[251] L. Li and Y.-L. Hsieh, "Ultra-fine polyelectrolyte fibers from electrospinning of poly (acrylic acid)," *Polymer,* vol. 46, pp. 5133-5139, 2005.

[252] X. Zong, K. Kim, D. Fang, S. Ran, B. S. Hsiao, and B. Chu, "Structure and process relationship of electrospun bioabsorbable nanofiber membranes," *Polymer,* vol. 43, pp. 4403-4412, 2002.

[253] C. J. Buchko, L. C. Chen, Y. Shen, and D. C. Martin, "Processing and microstructural characterization of porous biocompatible protein polymer thin films," *Polymer,* vol. 40, pp. 7397-7407, 12// 1999.

[254] S. Zhao, X. Wu, L. Wang, and Y. Huang, "Electrospinning of ethyl–cyanoethyl cellulose/tetrahydrofuran solutions," *Journal of Applied Polymer Science,* vol. 91, pp. 242-246, 2004.

[255] J. Deitzel, J. Kleinmeyer, D. e. a. Harris, and N. Beck Tan, "The effect of processing variables on the morphology of electrospun nanofibers and textiles," *Polymer,* vol. 42, pp. 261-272, 2001.

[256] J. S. Lee, K. H. Choi, H. D. Ghim, S. S. Kim, D. H. Chun, H. Y. Kim*, et al.*, "Role of molecular weight of atactic poly (vinyl alcohol)(PVA) in the structure and properties of PVA nanofabric prepared by electrospinning," *Journal of Applied Polymer Science,* vol. 93, pp. 1638-1646, 2004.

[257] C. Wang, C.-H. Hsu, and J.-H. Lin, "Scaling laws in electrospinning of polystyrene solutions," *Macromolecules,* vol. 39, pp. 7662-7672, 2006.

[258] C.-M. Hsu and S. Shivkumar, "Nano-sized beads and porous fiber constructs of poly (ε-caprolactone) produced by electrospinning," *Journal of Materials Science,* vol. 39, pp. 3003-3013, 2004.

[259] B. Ding, H.-Y. Kim, S.-C. Lee, D.-R. Lee, and K.-J. Choi, "Preparation and characterization of nanoscaled poly (vinyl alcohol) fibers via electrospinning," *Fibers and Polymers,* vol. 3, pp. 73-79, 2002.

[260] Y. Li, Z. Huang, and Y. Lǚ, "Electrospinning of nylon-6, 66, 1010 terpolymer," *European polymer journal,* vol. 42, pp. 1696-1704, 2006.

[261] S. Y. Gu and J. Ren, "Process Optimization and Empirical Modeling for Electrospun Poly (D, L-lactide) Fibers using Response Surface Methodology," *Macromolecular Materials and Engineering,* vol. 290, pp. 1097-1105, 2005.

[262] C. Wang, W. Zhang, Z. Huang, E. Yan, and Y. Su, "Effect of concentration, voltage, take-over distance and diameter of pinhead on precursory poly (phenylene vinylene) electrospinning," *Pigment & resin technology,* vol. 35, pp. 278-283, 2006.

[263] V. Sencadas, D. Correia, A. Areias, G. Botelho, A. Fonseca, I. Neves, *et al.*, "Determination of the parameters affecting electrospun chitosan fiber size distribution and morphology," *Carbohydrate Polymers,* vol. 87, pp. 1295-1301, 2012.

[264] W. Cui, X. Li, S. Zhou, and J. Weng, "Investigation on process parameters of electrospinning system through orthogonal experimental design," *Journal of applied polymer science,* vol. 103, pp. 3105-3112, 2007.

[265] R. Krishnappa, K. Desai, and C. Sung, "Morphological study of electrospun polycarbonates as a function of the solvent and processing voltage," *Journal of materials science,* vol. 38, pp. 2357-2365, 2003.

[266] T. Subbiah, G. Bhat, R. Tock, S. Parameswaran, and S. Ramkumar, "Electrospinning of nanofibers," *Journal of Applied Polymer Science,* vol. 96, pp. 557-569, 2005.

[267] M. Khayet and T. Matsuura, *Membrane distillation: principles and applications*: Elsevier, 2011.

[268] H. Homayoni, S. A. H. Ravandi, and M. Valizadeh, "Electrospinning of chitosan nanofibers: Processing optimization," *Carbohydrate Polymers,* vol. 77, pp. 656-661, 2009.

[269] A. H. Touny, J. G. Lawrence, A. D. Jones, and S. B. Bhaduri, "Effect of electrospinning parameters on the characterization of PLA/HNT nanocomposite fibers," *Journal of Materials Research,* vol. 25, pp. 857-865, 2010.

[270] Y. Feng, F. Meng, R. Xiao, H. Zhao, and J. Guo, "Electrospinning of polycarbonate urethane biomaterials," *Frontiers of Chemical Science and Engineering,* vol. 5, pp. 11-18, 2011.

[271] J. Kameoka and H. Craighead, "Fabrication of oriented polymeric nanofibers on planar surfaces by electrospinning," *Applied Physics Letters,* vol. 83, pp. 371-373, 2003.

[272] A. H. Hekmati, A. Rashidi, R. Ghazisaeidi, and J.-Y. Drean, "Effect of needle length, electrospinning distance, and solution concentration on morphological properties of polyamide-6 electrospun nanowebs," *Textile Research Journal,* vol. 83, pp. 1452-1466, 2013.

[273] J. S. Bunch and M. L. Dunn, "Adhesion mechanics of graphene membranes," *Solid State Communications,* vol. 152, pp. 1359-1364, 8// 2012.

[274] Z. Yoshimitsu, A. Nakajima, T. Watanabe, and K. Hashimoto, "Effects of surface structure on the hydrophobicity and sliding behavior of water droplets," *Langmuir,* vol. 18, pp. 5818-5822, 2002.

[275] D. Quéré, "Wetting and roughness," *Annu. Rev. Mater. Res.,* vol. 38, pp. 71-99, 2008.

[276] J. W. Suk, A. Kitt, C. W. Magnuson, Y. Hao, S. Ahmed, J. An*, et al.*, "Transfer of CVD-grown monolayer graphene onto arbitrary substrates," *ACS nano,* vol. 5, pp. 6916-6924, 2011.

[277] R. R. Nair, H. A. Wu, P. N. Jayaram, I. V. Grigorieva, and A. K. Geim, "Unimpeded Permeation of Water Through Helium-Leak–Tight Graphene-Based Membranes," *Science,* vol. 335, pp. 442-444, January 27, 2012 2012.

[278] P. W. Morgan and S. L. Kwolek, "Interfacial polycondensation. II. Fundamentals of polymer formation at liquid interfaces," *Journal of Polymer Science,* vol. 40, pp. 299-327, 1959.

[279] R. G. Griskey and C. A. Patel, "Laminar and turbulent flow continuous interfacial polycondensations of nylon 66," *Journal of Applied Polymer Science,* vol. 38, pp. 351-357, 1989.

Vitae

Name : Feras Mohammad Abdalla Kafiah.

Nationality : Jordanian.

Date of Birth : 26-05-1981.

Email : fkafiah399@gmail.com.

Address : Dhahran- 31261, Saudi Arabia.

Academic Background : PhD in Mechanical Engineering.